RAPID SOLIDIFICATION OF OXIDES: ZrO_2-CONTAINING CERAMICS AND HIGH T_c SUPERCONDUCTORS

by

JOANNA MARIE McKITTRICK

B.S., Mechanical Engineering
University of Colorado, Boulder, Colorado

M.S., Materials Science and Engineering
Northwesterm University, Evanston, Illinois

Submitted to the Department of Materials Science and Engineering
in partial fulfillment of the requirements for the

DEGREE OF DOCTOR OF PHILOSOPHY

at the

MASSACHUSETS INSTITUTE OF TECHNOLOGY

May 1988

Signature of Author_____
Department of Materials Science and Engineering
April 29, 1988

Certified by_____
Gretchen Kalonji
Thesis Supervisor

Accepted by_____
John B. Vander Sande
Chairman, Departmental Committee on Graduate Students

RAPID SOLIDIFICATION OF OXIDES: ZrO_2-CONTAINING CERAMICS AND HIGH T_c OXIDE SUPERCONDUCTORS

by

Joanna McKittrick

Submitted to the Department of Materials Science and Engineering on
May 1988 in partial fulfillment of the requirements
for the degree of Doctor of Philosophy in Ceramics

ABSTRACT

Two classes of oxide systems, ZrO_2 containing ceramics and $MBa_2Cu_3O_{7-x}$ (M=Y, Eu, Gd) superconductors, were melted and rapidly solidified by a variety of techniques. A crucibleless melting technique was used for all of the compositions. A twin roller solidification device generated materials with the highest quench rates, on the order of 10^7 K/sec.

Al_2O_3-ZrO_2 eutectic and off-eutectic compositions, the Al_2O_3-Y_2O_3-ZrO_2 eutectic composition and two ternary eutectics in the Al_2O_3-MgO-ZrO_2 system were examined. Amorphous and metastable crystalline materials were generated for all compositions. The microstructures generated for different compositions and cooling rates can be predicted by solidification theory. Annealing was performed under a range of thermal conditions, and compositional and microstructural changes were examined as the systems approached equilibrium. For the Al_2O_3-ZrO_2 and Al_2O_3-Y_2O_3-ZrO_2 eutectic compositions, devitrification occurred between 930-945°C with the nucleation of a ZrO_2 phase. In the Al_2O_3-MgO-ZrO_2 ternary eutectics, annealing the as-quenched, crystalline materials resulted in significant diffusion of Al_2O_3 and MgO, yielding complex phase assemblages.

The $MBa_2Cu_3O_{7-x}$ compositions were melted with an H_2-O_2 torch with an O_2-rich flame. Significant reduction of the oxide was avoided by maintaining an overpressure of O_2 above the melt. Two metastable phases were found, amorphous materials and a previously unreported cubic phase, at the highest quench rates. The cubic phase does not have the 1:2:3 stoichiometry but is copper rich. The as-quenched materials are not superconducting, but must be annealed above 920°C in O_2. The phase development was identified through annealing experiments. The amorphous materials crystallize in a temperature range of 730-750°C. The peritectic decomposition temperatures of the Eu and Gd-1:2:3 compositions are 50°C higher than the Y-1:2:3. At low quench rates, the solidification path is complex as multiphase materials were generated. The annealed materials had excellent superconducting properties; a narrow transition width and a high T_c. Magnetic relaxation data indicate that the rapidly solidified materials have a narrower distribution of pinning sites than single crystals or materials produced through conventional powder processing techniques.

Thesis Supervisor: Gretchen Kalonji
Title: Associate Professor of Materials Science

TABLE OF CONTENTS

LIST OF FIGURES

LIST OF TABLES

ACKNOWLEDGEMENTS

This work was supported by the United States Department of Energy Grant # DE-FG02-84ER451 and by the National Aeronautics and Space Administration through a block grant to the Materials Processing Center. I would like to express my utmost gratitude to the Hughes Aircraft Company for granting me a Howard Hughes Doctoral Fellowship for five years.

I sincerely thank my advisor, Professor Gretchen Kalonji, who has been a continual source of guidance and humor during my graduate career. I am most grateful to my thesis committee members, Professors Linn Hobbs and Yet-Ming Chiang, and to Dr. Robert O'Handley for their suggestions and indefatigable cooperation.

This work couldn't have been done without the help of all the folks who helped with or trained me on various analytical instruments: Mike Frongillo on the TEM, Tony Garrett-Reed on the STEM, Hans Jennsen on the IR, and Serge Bensoussian on the x-ray diffraction units. H. Choi ran the VUV unit and provided me with the data. Jagadeesh Moodera cheerfully assisted me at the National Magnet Lab in obtaining and analyzing data. Simone Peterson helped me with the SEM work. Professor Kingery allowed me to use his DTA equipment. All of them receive my sincere thanks.

The laser splat materials were provided to me from John Haggerty and Jean-Marc Lehrmann, the solar splats from Alex Revcolevschi at the University of Paris and additional rapidly solidified materials from Robert Ingel at the NRL. I sincerely appreciate their contributions.

Several colleagues deserve a special acknowledgement for both their friendship and technical contributions: Mike McHenry was a constant inspiration for the work on the superconductors and Shinichi Sasayama and Teiichi Ando assisted immeasurably with the rapid solidification processing techniques. I am sincerely grateful for the friendship of Mark DeGuire and Pierre Deymier who were instrumental in making graduate life a more enjoyable and rewarding experience and to my office mates, Han-Ill Yoo, Peter Moon, and Thao Nguyen who maintained a congenial atmosphere during my first few years as a graduate student.

Special thanks are due to the wonderful assortment of UROP and other undergraduate students who passed through the lab, notably Olof Hellman, Eduardo Gómez, Steve Geislinger, Peter Standley and Catherine Heremans. And to Pat Kearney, Fred Wilson and John Centerino who bent over backwards at times to help me with a myriad of problems, for which I'll be eternally grateful. Dennis Clougherty has ceaselessly availed himself to me in the preparation of this document and deserves a heartfelt thanks.

Finally, I thank my family for their unflagging love and encouragement over the years. This work could not have been produced without their support.

PART I

INTRODUCTION

Rapid solidification is a processing technique used to generate materials with unusual microstructures and properties which may not be obtainable through other methods. To date, most of the work has been on metallic systems and more recently in ceramic systems. Duwez (1967) and collaborators discovered in 1960 that splatting a liquid metal against a cold substrate resulted in the formation of a metallic glass. Subsequently, Sarjeant and Roy applied this technique to oxides in 1967. Quench rates reported for rapid solidification of oxides range from 10^3-10^9 K/sec [Brockway and Wills (1984)].

Faster solidification rates suppress diffusion in both the liquid and solid and hence curb the formation of the equilibrium phases and microstructures found in more slowly cooled materials. There are several beneficial outcomes for materials produced through rapid solidification. First, increasing the solidification rate results in a smaller grain size. Second, the grains are chemically homogeneous and have limited or no grain boundary segregation of impurities. Third, faster quench rates can extend the terminal solid solubility of the primary phase. And, fourth, metastable phases can be quenched in from the melt which include supersaturated or amorphous materials.

Besides being a scientific curiosity, there are many technological reasons to study rapid solidification of oxides. Laboratory studies have shown that rapid solidification of oxides has produced glasses with ionic conductivities much higher than the polycrystalline materials of the same composition, other glasses with good long wavelength IR transmission, and crystalline and amorphous materials with desirable semiconductive or magnetic properties [Revcolevschi and Livage (1981)]. These materials have the potential to be exploited commercially, and the technology is available to produce rapidly solidified glass or ceramic powders, to produce continuous fibers or strips, and to consolidate the rapidly solidified powders while retaining the metastable phases.

This work has examined the benefits of rapid solidification processing on two classes of oxide systems. Part II comprises the research done on ZrO_2 binary and ternary systems. Part III contains the research done on high temperature oxide superconductors in the systems $MO_{1.5}$-BaO-CuO (M=Y, Eu, Gd). For both parts, a variety of melting and solidification techniques were employed and the microstructural features and phase stability of the resultant materials were evaluated

ZrO_2 systems are of interest because of their high potential for use in structural as well as in electronic applications. ZrO_2 is rarely used in its pristine state; it must be alloyed with other oxides in order to attain any of its desirable properties. This work has focused on ZrO_2 systems with Al_2O_3, Al_2O_3-Y_2O_3, and MgO-Al_2O_3, systems which are currently used in industrial applications.

The oxide superconductors offer a tremendous potential for future use in a diversity of fields. The superconductors can be utilized as electronic or magnetic materials. The list of possible applications includes electronic devices, power transmision lines, magnetic pick-ups and magnetic shielding, to name only a few. Exploitation of these materials relies on generating materials with optimal superconducting properties and understanding the structure/property relationships. Rapid solidification processing is capable of producing fine grained materials and pore-free materials, which is advantageous in terms of both superconducting and structural properties.

PART II

ZrO_2 CONTAINING CERAMICS

1. INTRODUCTION AND LITERATURE REVIEW

1.1. Overview

Zirconia is a remarkable and versatile material which has wide applicability in a number of fields. Interest in both the scientific and engineering communities has lead to intense research efforts during the past decade. ZrO_2 is an electronic as well as a structural ceramic, and due to its high refractive index, is used in ceramic glazes as an opacifier and in jewelrey. Doped cubic ZrO_2 is an ionic conductor and is used as O_2 sensors in catalytic converters in automobiles, for high temperature fuel cells, electrochemical oxygen pumps, resistance heating elements and susceptors for induction heating. It is also used as a thermal barrier material due to its low thermal conductivity, and as tool bits and extrustion dies because of its high fracture toughness. It is still under investigation as a replacement material for some components in internal combustion engines. Zirconia has been the subject of three international symposia over the past six years and yet questions remain about some of the fundamental materials properties.

Rapid solidification is currently used as a processing technique for different materials applications in ZrO_2 systems. Rapidly solidified compositions of Al_2O_3-ZrO_2 are used as abrasive materials. Rapid solidification in this case causes the retention of a high temperature, metastable ZrO_2 phase which transforms to the stable phase under applied stress and with a volume expansion. This volume expansion cracks the Al_2O_3 matrix surrounding the ZrO_2 to expose freshly cracked, abrasive surfaces. Precursor powders for plasma spraying are rapidly solidified from compositions of Y_2O_3-ZrO_2, which generates powders with a high degree of chemical mixing and aids in avoiding segregation during the plasma spraying operation.

In this study, the microstructures and phase stability of rapidly solidified Al_2O_3-ZrO_2 materials, three binary compositions and the eutectics in two ternary systems, the Al_2O_3–Y_2O_3-ZrO_2 and the Al_2O_3-MgO-ZrO_2 system, were examined. One goal of this research was to obtain rapidly solidified materials containing different concentrations of ZrO_2. ZrO_2 has a melting point above 2600°C and is thus hard to melt in its pure state. This work focused on compositions containing ZrO_2 in the range of 20-70 mol%. Another goal was to understand the microstructural development of the crystalline materials produced in terms of solidification theory. This is important for future microstructural control of the materials. Another goal was to study the devitrification of the amorphous materials produced. This in itself is a processing technique in which uniform, fine-grained microstructures can be obtained. And the final goal was to to gain further understanding of how the different polymorphs of ZrO_2 are obtained and stabilized with different alloying oxides through the rapid solidification process.

1.3 Phase Diagrams and Phase Equilibria

1.3.1 Al_2O_3-ZrO_2

Figure 1.0 shows two phase diagrams of the Al_2O_3-ZrO_2 binary system as determined by Cevales (1968)[Levin and McMurdie (1975)] and Alper (1967)[Levin and McMurdie (1975)]. The Cevales diagram, shown in Figure 1.1(a), indicates a eutectic temperature of 1710°C and a eutectic composition of 40.0 ^{m}/o (42.6 ^{w}/o) ZrO_2, and shows no solid solubility of one oxide in the other. A high temperature phase, ε-Al_2O_3, is found for compositions of ZrO_2 up to 2.8 ^{m}/o (3.3^{w}/o). In the Alper diagram, the eutectic temperature is 1880°C and the eutectic composition is 37.5 ^{m}/o (42 ^{w}/o) ZrO_2. This diagram shows limited solid solubility of each oxide in the other. Up to ~1.2 ^{m}/o (1.4 ^{w}/o) ZrO_2 can be dissolved in the Al_2O_3 phase and up to ~8.5 ^{m}/o (7.1 ^{w}/o) Al_2O_3 can be dissolved in the ZrO_2 phase at the eutectic temperature. The only other significant difference is that the liquidus on the ZrO_2 side of the diagram is convex into the liquid for the Cevales diagram and concave for the Alper diagram.

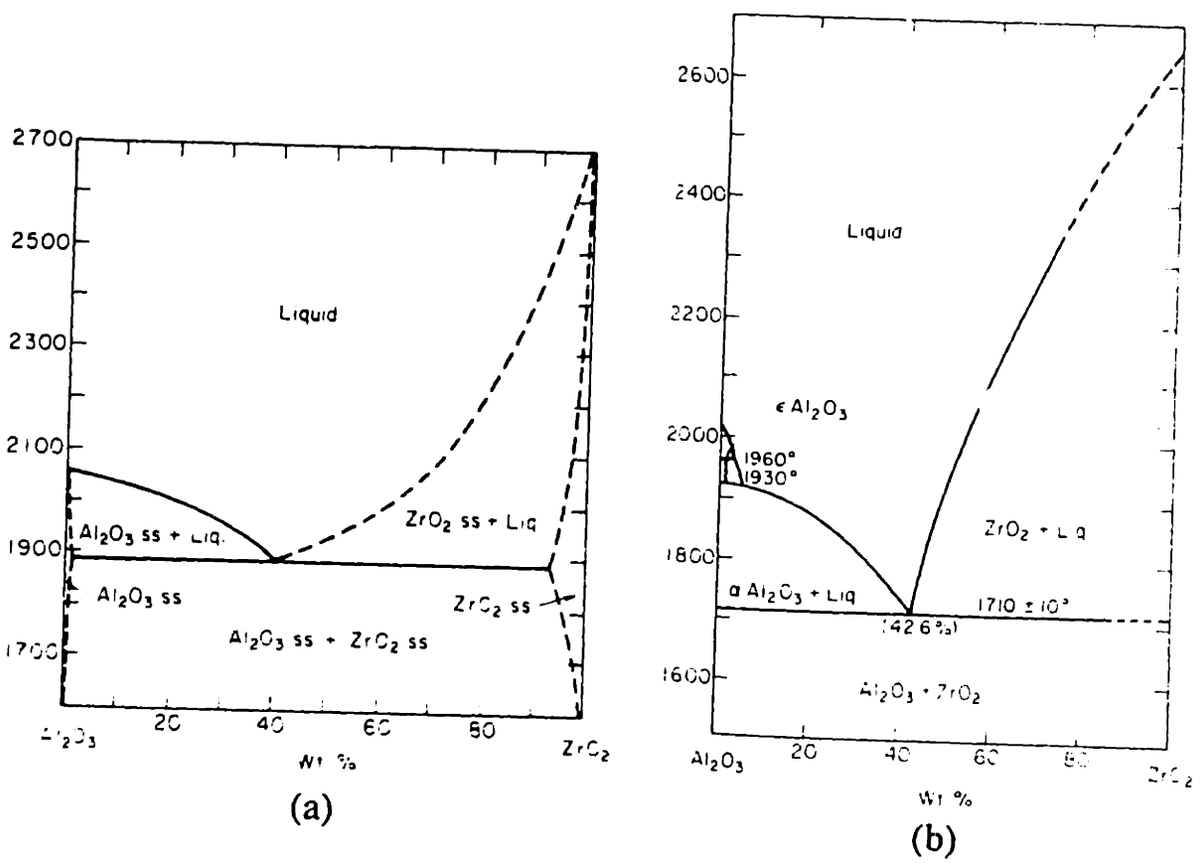

Figure 1.0
Phase diagrams reported for the Al_2O_3-ZrO_2 system. (a) Cevales (1968) [Levin and McMurdie (1975)] and (b) Alper (1967) [Levin and McMurdie (1975)]

1.3.2 Al_2O_3-Y_2O_3-ZrO_2 and Y_2O_3-ZrO_2

Figure 1.1 shows the subsolidus ternary phase diagram for the Al_2O_3-Y_2O_3-ZrO_2 system, as determined by Tuohig and Tien (1980). As indicated by the diagram, additions of small amounts of Y_2O_3 to the Al_2O_3-ZrO_2 eutectic result in the formation of t-ZrO_2. Increasing the Y_2O_3 content results in the formation of c-ZrO_2. A ternary eutectic composition identified by Echigoya et.al.(1986) is found to be 59 ^{m}/o Al_2O_3-4.2 ^{m}/o Y_2O_3-36.8 ^{m}/o ZrO_2 (52.3 ^{w}/o Al_2O_3-8.2 ^{w}/o Y_2O_3-39.4 ^{w}/o ZrO_2), which is indicated on the phase diagram. As shown, the eutectic falls in the α-Al_2O_3-c-ZrO_2 equilibrium phase field. Figure 1.2 shows the ZrO_2-Y_2O_3 binary phase diagram, as determined by Scott (1975). According to this diagram, only c-ZrO_2 is stable for Y_2O_3 contents greater than ~9 ^{m}/o. For lower compositions t- and/or m-ZrO_2 form. At intermediate Y_2O_3 contents t'-ZrO_2 is found.

1.3.3 Al_2O_3-MgO-ZrO_2, MgO-ZrO_2, and Al_2O_3-MgO

Figure 1.3 shows the ternary Al_2O_3-MgO-ZrO_2 phase diagram as determined by Bierezhnoi and Kordyuk (1964). Two ternary eutectics and one binary pseudo-eutectic were identified and shown on the diagram. Figure 1.4 shows two binary phase diagrams, for ZrO_2-MgO in (a) [Grain (1967)] and for Al_2O_3-MgO shown in (b) [Alper et al. (1962) and Roy et al. (1953)]. The MgO-ZrO_2 phase diagram shows that the cubic phase field extends up to ~21 mol% MgO at high temperatures. Under ambient conditions, the cubic phase decomposes into m-ZrO_2 and MgO. The MgO-Al_2O_3 phase diagram consists of two binary eutectics, MgO-$MgAl_2O_4$ and $MgAl_2O_4$-Al_2O_3. The spinel phase, $MgAl_2O_4$, displays a high degree of non-stoichiometry at elevated temperatures and ranges from 40-85 mol% Al_2O_3. There is some question in regard to the slope of the phase boundary between spinel and MgO+spinel for the MgO-rich spinels. Unpublished data by Chiang (1988) indicate that the degree of non-stoichiometry is more limited than what is shown in the phase diagram.

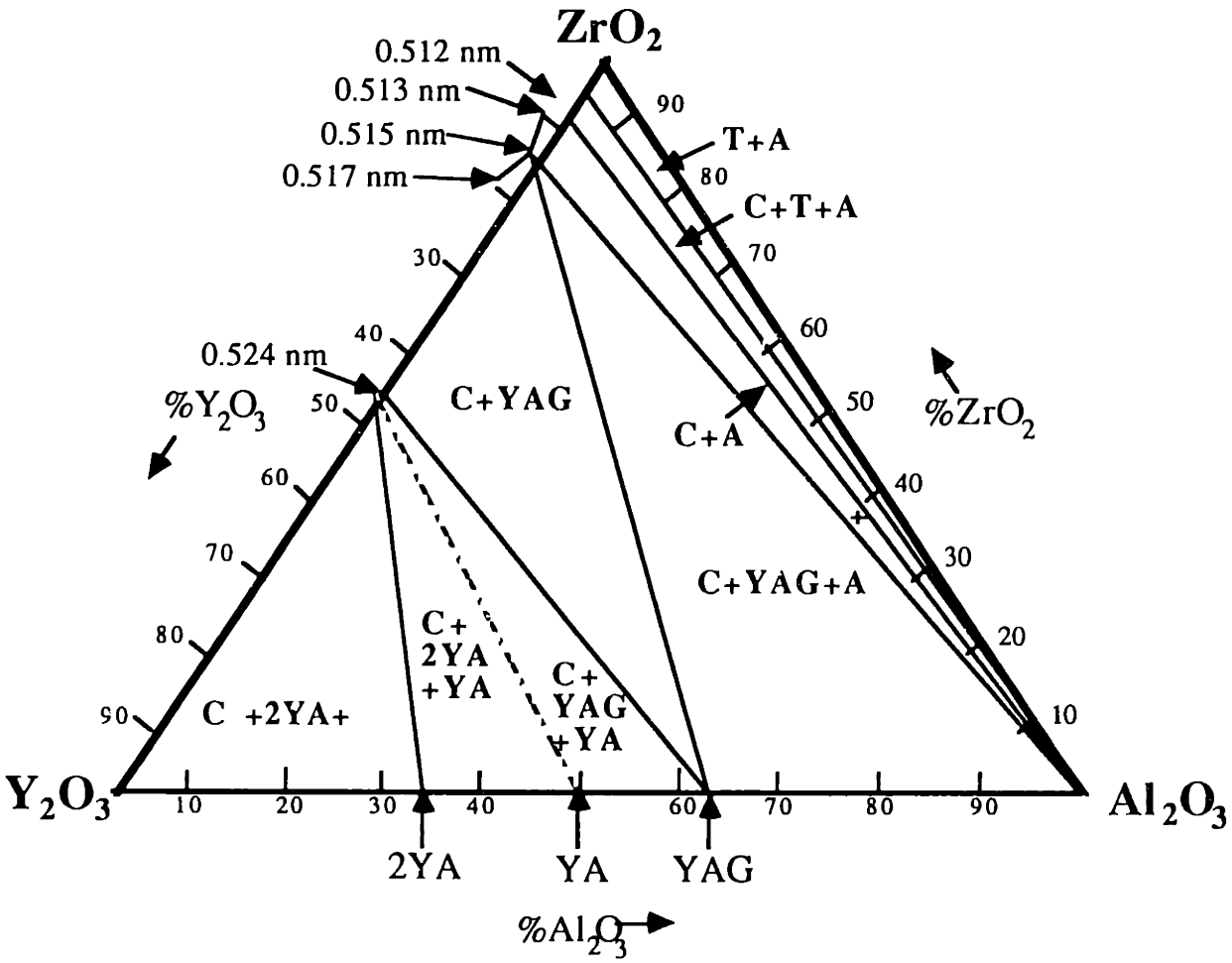

Compositions examined:
(mol%)

Al_2O_3	Y_2O_3	ZrO_2
52.3	4.2	36.9

Figure 1.1

Subsolidus phase diagram of the Al_2O_3-Y_2O_3-ZrO_2 system from Tuohig and Tien (1980). Eutectic composition was identified by Echigoya et al. (1986).

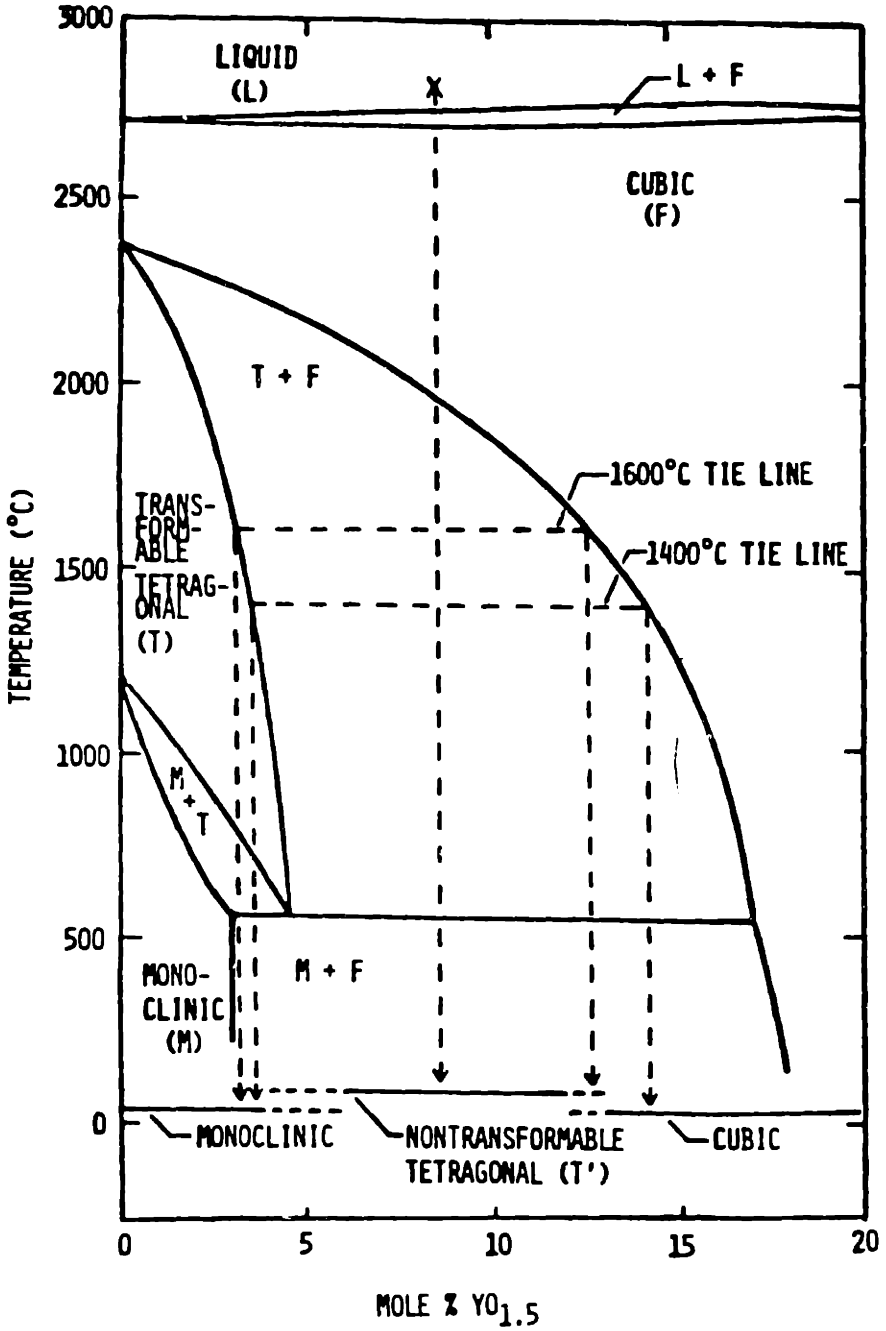

Figure 1.2.
Low Y_2O_3 region of the ZrO_2-$YO_{1.5}$ binary phase diagram. From Scott (1975).

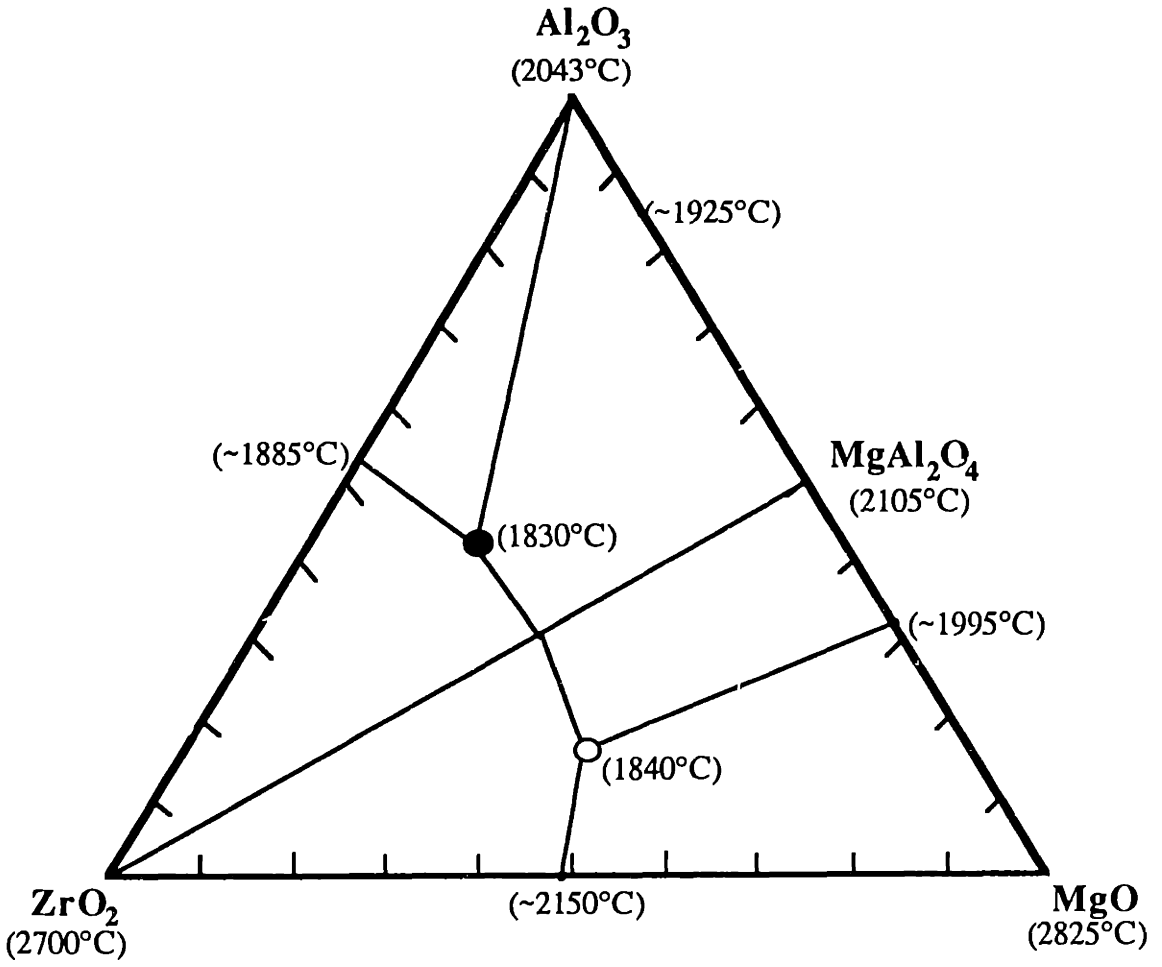

Compositions examined:
(mol%)

	Al_2O_3	MgO	ZrO_2
○	16.6	42.1	41.3
●	42.1	17.4	40.5

Figure 1.3

Phase diagram of MgO-Al_2O_3-ZrO_2. Two eutectics are indicated, a MgO-rich and an Al_2O_3 -rich. From Bierezhnoi and Kordyuk (1964).

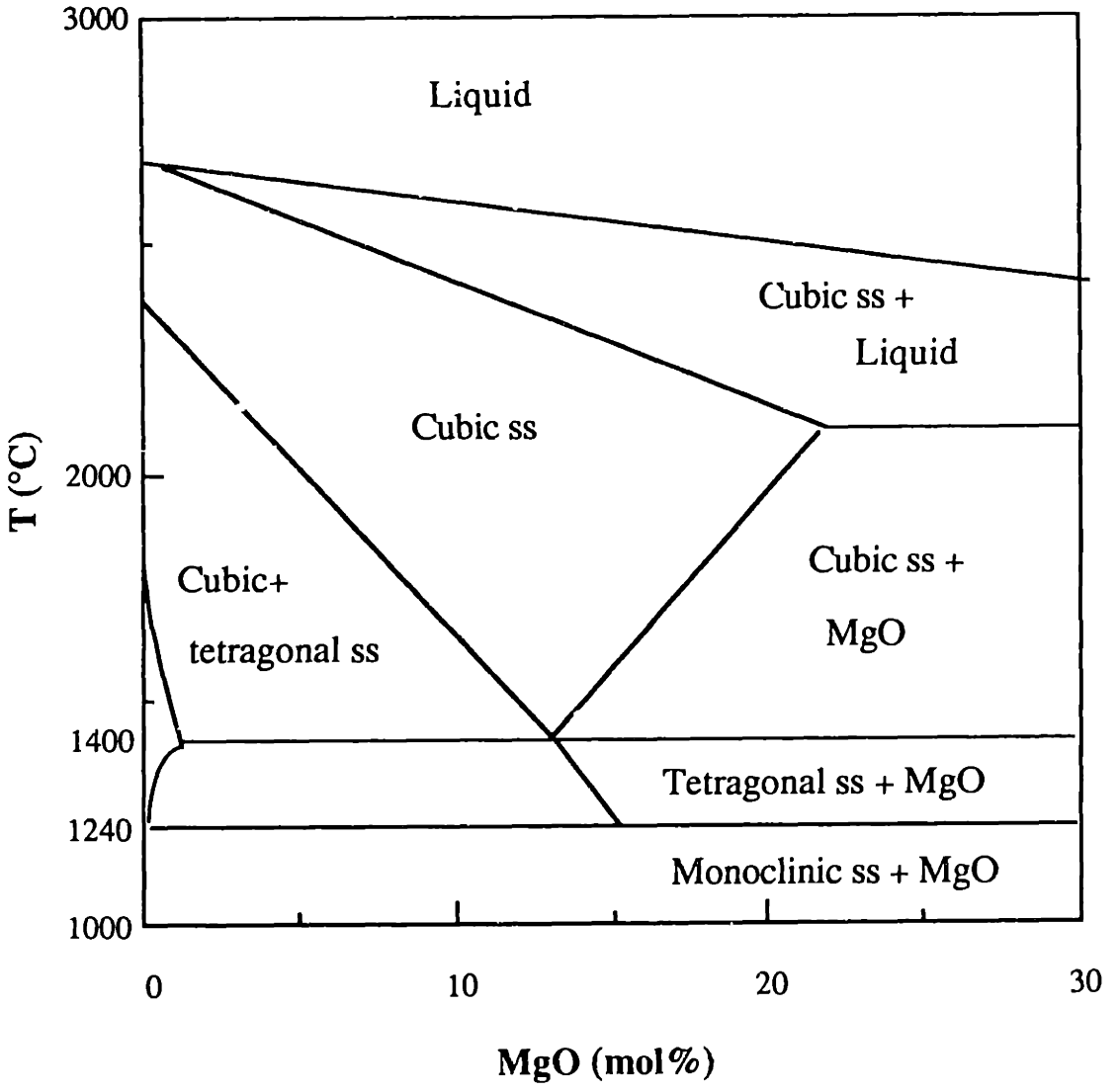

Figure 1.4(a)
MgO-ZrO_2 phase diagram from Subbarao (1981).

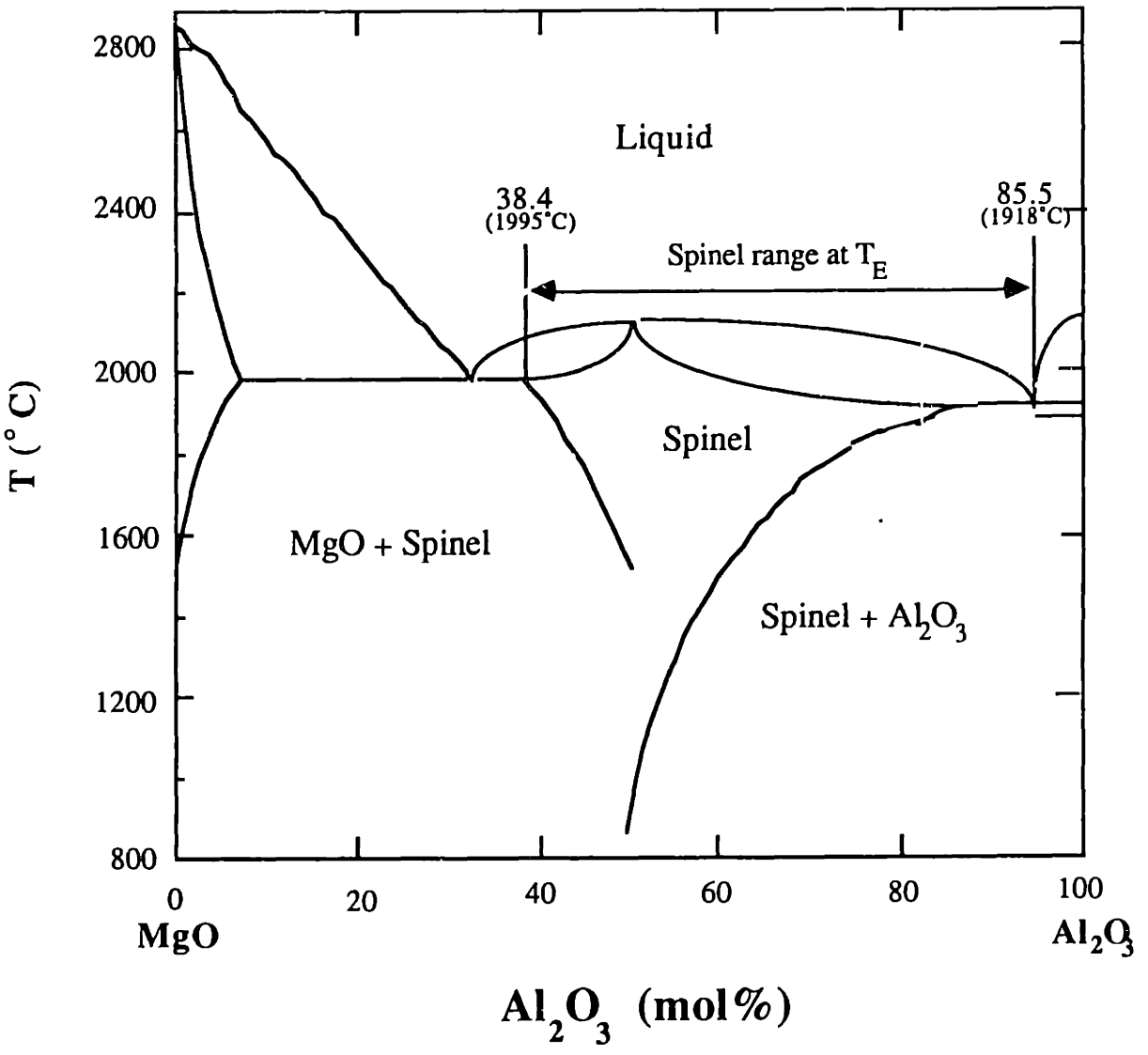

Figure 1.4(b)

MgO-Al_2O_3 phase diagram. Taken from Alper et al. (1962) and Roy et al. (1953).

1.4 Rapid Solidification Techniques

There are two general techniques for rapidly solidifying melts; substrate quenching and atomization, which yield different materials with different thermal histories. In either case, a suitable melting method must be employed along with an adequate quenching device to attain high cooling rates. Melting and solidification of ceramics is a more cumbersome task then for metals. Ceramics typically have high melting points which leads to practical problems with the determination of an adequate heating source, the container material if a crucible is to be used and in heat containment. The heating methods for high temperature materials are usually induction, laser, plasma or flame heating. There are only a few materials which can contain high temperature melts, notably W, Mo and graphite. The refractory metals suffer from applicability due to their cost and extreme difficulity in machining. Graphite is easier to form but will reduce the material and may form carbides or otherwise contaminate the melt. Insulation can be a critical problem in both providing enough of a barrier to the heat transfer to keep the material at a high temperature and to protect the surrounding environment from the extreme temperatures.

Substrate quenching is the solidification of the melt against one or two surfaces which are at a lower temperature than the melt, usually at room temperature or in some cases, close to liquid nitrogen temperature. The principle behind substrate quenching is to spread the thinnest amount of liquid onto a substrate with a high thermal conductivity in order to achieve the greatest heat extraction rate. Techniques such as twin roller quenching [Chen and Miller (1970)], melt spinning [Suzuki et al. (1977)], anvil and hammer quenching [Revcolevschi et al. (1975)] and flame or plasma spraying [Frank and Liebertz (1968)] have been sucessfully used in quenching ceramics. Twin roller quenching consists of squeezing the liquid through two rollers in contact rotating at a high rate of speed. Melt spinning is the application of a spinning wheel to the surface of melt so that the material is solidified on the roller and 'spun' into a collection chamber. In flame or plasma spraying, the material is melted in a gas torch or plasma gun and sprayed onto a cold substrate. For a comprehensive review of the techniques successfully used on oxide compositions, see Revcolevschi and Livage (1981). For these above stated methods, the heat is extracted primarily through the substrate and little, if any, undercooling is achieved in the liquid, and the temperature gradient into the melt is positive.

Ruhl (1967) has estimated that cooling during splat quenching is controlled by the interfacial resistance between the melt and the substrate for Biot numbers (Bi)$<$0.015, and

is controlled by the thermal conductivity of the solidified material for Bi>30. The Biot number and is defined as hd/k, where h is the heat transfer coefficient between the splat and the substrate, d is the thickness of the splat and k is the thermal conductivity of the solidified material. If there is complete thermal contact between the splat and the substrate ($h=\infty$), there is not a discontinuity in the temperature gradient at the interface and the cooling is ideal. For ideal cooling, Birnie and Kingery (1985) have estimated the cooling rate to be:

$$\frac{dT}{dt} = \frac{k\Delta T}{\rho c_p d^2} \qquad (1.0)$$

where ΔT is the temperature difference between the substrate and the melt, ρ is the density of the solidified product, and c_p is the specific heat of the solidified material. In Newtonian cooling, the thermal resistance between the sample and the substrate limits the cooling rate, and is expressed by [Geiger and Poirier (1973)]:

$$\frac{dT}{dt} = \frac{h\Delta T}{\rho c_p d} \qquad (1.1)$$

Estimates for h during splat quenching of metals range between 10^4-10^5 $Wm^{-2}K^{-1}$ [Clyne and Garcia (1981)]. Although the exact values for cooling rates for each mechanism can not be known *a priori*, an estimate can be made for oxides. Using typical values of k=1 W m^{-1} K^{-1}, c_p=800 J kg^{-1} K^{-1}, ρ=3000 kg m^{-3}, ΔT=1500 K, d=10^{-5} m and h=10^3 W m^{-2} K^{-1}, the cooling rate for ideal cooling is ~10^7 K/sec, and for Newtonian cooling it is ~10^5 K/sec. These are only approximations as k, c_p, and ρ are functions of temperature and composition. If high cooling rates are achieved in oxides, it appears that ideal cooling must be rate limiting, although a combination of the two mechanisms is most likely present. [See Sec. 3.2.6 for estimates of cooling rates.]

If significant undercooling is present in the melt, the heat can be removed both from the solid and the liquid and higher cooling rates can be obtained, as for the case of atomization of the melt. Atomization is the process of breaking up a molten stream of liquid into small spheres by the use of gas or water jets. Significant undercooling can be

achieved and the latent heat can flow into both the solid and liquid due to the negative temperature gradient. The growth rate is determined by the heat transfer coefficient for radiant and convective cooling and by the amount of recalescence. This is again be limited for the case of oxides as they tend to be insulators when solid.

A variety of techniques have been used to rapidly solidify Al_2O_3-ZrO_2 compositions with varying results. Krauth and Meyer (1963) were the first to produce amorphous materials by plasma spraying the eutectic composition onto a cool substrate. They also found the metastable high temperature polymorphs, γ-Al_2O_3 and t-ZrO_2, along with some m-ZrO_2. They examined a range of compositions across the phase diagram. Claussen et.al.(1983) used flame pressure atomization and high pressure water atomization to produce amorphous and crystalline materials. They found amorphous materials for the highest quench rates, ϵ-Al_2O_3 and t-ZrO_2 for intermediate rates, and α-Al_2O_3 and m-ZrO_2 for lowest rates. Peterson (1987) used gas atomization and obtained small spheres of amorphous materials along with larger spheres of crystalline material, α-Al_2O_3 and t-ZrO_2. Ando et al. (1986) used centrifugal atomization; a technique in which a pellet of the material is placed on the center of a rotating disk and melted with a torch applied to the top of the pellet. The spinning causes the molten pool to break up into into small spheres which solidify in the air before impacting the collection chamber. Bender et al. (1986) report a method where the sample is suspended, melted and allowed to drop onto a rotating cylinder which is partially submurged in water. Table 1.0 summarizes the results from rapid solidification of Al_2O_3-ZrO_2 compositions found in the literature.

Several studies have been done on rapid solidification of compositions in the MgO-Al_2O_3 system. Sarjeant and Roy (1967) found a spinel structure for MgO-Al_2O_3 compositions of 20-100 mol% Al_2O_3 in their splat cooled materials. A high degree of cation disorder was found in these splats seen in the IR spectra. The pure Al_2O_3 diffraction patterns showed the presence of α-Al_2O_3 as well as the high temperature, metastable spinel-structure γ-Al_2O_3 phase. Jantzen et al. (1980) found amorphous materials along with a metastable, monoclinic intermediate spinel phase in systems containing from 50-77.8 mol% Al_2O_3 in splat quenched materials. This monoclinic phase had been reported for Al_2O_3 concentrations > 71.4 mol% under equilibrium conditions [Saalfeld and Jagodzinski (1957)].

Technique	*Material Produced*	*Phases Present*	*Quench Rate (K/sec)*	*Research Group*
Plasma Spraying	Flakes	amorphous and γ-Al_2O_3 and t-&m-ZrO_2	10^5	Krauth & Meyer (1963)
Flame Pressure Atomization	Transparent, translucent, and opaque white spheres	amorphous and α+ε–Al_2O_3 and t+m-ZrO_2	10^3-10^5	Claussen et al. (1983)
Gas Atomization	Transparent, black and white spheres	amorphous and α-Al_2O_3 and t-ZrO_2	10^3-10^5	Peterson (1987)
Centrifugal Atomization	White spheres		(*)	Ando (1986)
Roller Quenching in water	White spheres and flakes	α-Al_2O_3 and t+m-ZrO_2	(*)	Bender et al. (1986)

Table 1.0. Summary of the results on rapid solidification of Al_2O_3-ZrO_2 compositions found in the literature. (*) Not reported.

Work done on rapidly solidifying pure ZrO_2 has resulted in the formation of crystalline products only [Topol et al. (1973)] but several studies on rapidly solidifying pure Al_2O_3 have yielded crystalline and amorphous materials. In plasma sprayed Al_2O_3, δ, γ, and θ phases have been found [Wilms and Herman (1976)], and laser splatting has yielded the α, γ and δ phases for successively higher quench rates, respectively [Sarjeant and Roy ()]. Y_2O_3 additions to Al_2O_3 yield δ-Al_2O_3 and $Y_3Al_5O_{12}$ with amorphous materials for splat quenching of 1.4 and 4.6 mol% Y_2O_3 [Krepski (1975)].

There has not been any work done on rapid solidification of ternary compositions containing Al_2O_3-ZrO_2.

1.5 Zirconia and Alumina Polymorphs and Stabilization

1.5.1 Zirconia Polymorphs

Pure zirconium oxide (ZrO_2) has three known polymorphs under ambient conditions. Upon heating from room temperature, the crystal structures and transformation temperatures are:

$$\text{monoclinic} \xrightarrow{1170^\circ C} \text{tetragonal} \xrightarrow{2370^\circ C} \text{cubic} \xrightarrow{2680^\circ C} \text{liquid}$$

The cubic phase has a fluorite structure with space group Fm3m, as shown in Figure 1.5. The tetragonal form is also a distorted fluorite structure in which the oxygens in the center of the cell are slightly displaced from the ideal fluorite position, as shown in Figure 1.6. Figure 1.7 shows the monoclinic crystal structure. In this structure the zirconium atoms are coordinated with only 7 oxygen, instead of 8, as in the other two structures. Table 1.1 summarizes the crystallography of the ZrO_2 phases.

The most studied transformation is the reversible tetragonal - -> monoclinic, as it gives rise to improved fracture toughness in the pure material and in other materials in which the ZrO_2 is dispersed as a second phase. The t—>m transformation is martinsitic; it is athermal, diffusionless and shear displacive. This transformation is unusual in that there is an increase in volume upon transformation to the lower temperature phase, like the freezing of water. The volume expansion is in the range of 3-5%. The transformation can be stress induced; if the tetragonal modification can be retained below the start of the martinsitic transformation temperature, M_S, the application of stress can trigger the endothermic transformation. The properties of this transformation can be exploited to increase the fracture toughness through the stress induced transformation or microcrack nucleation. Retention of the tetragonal phase is a function of particle size and shape, elastic and thermal properties of the particle and its surrounding matrix, and of chemical composition, as discussed in the following sections.

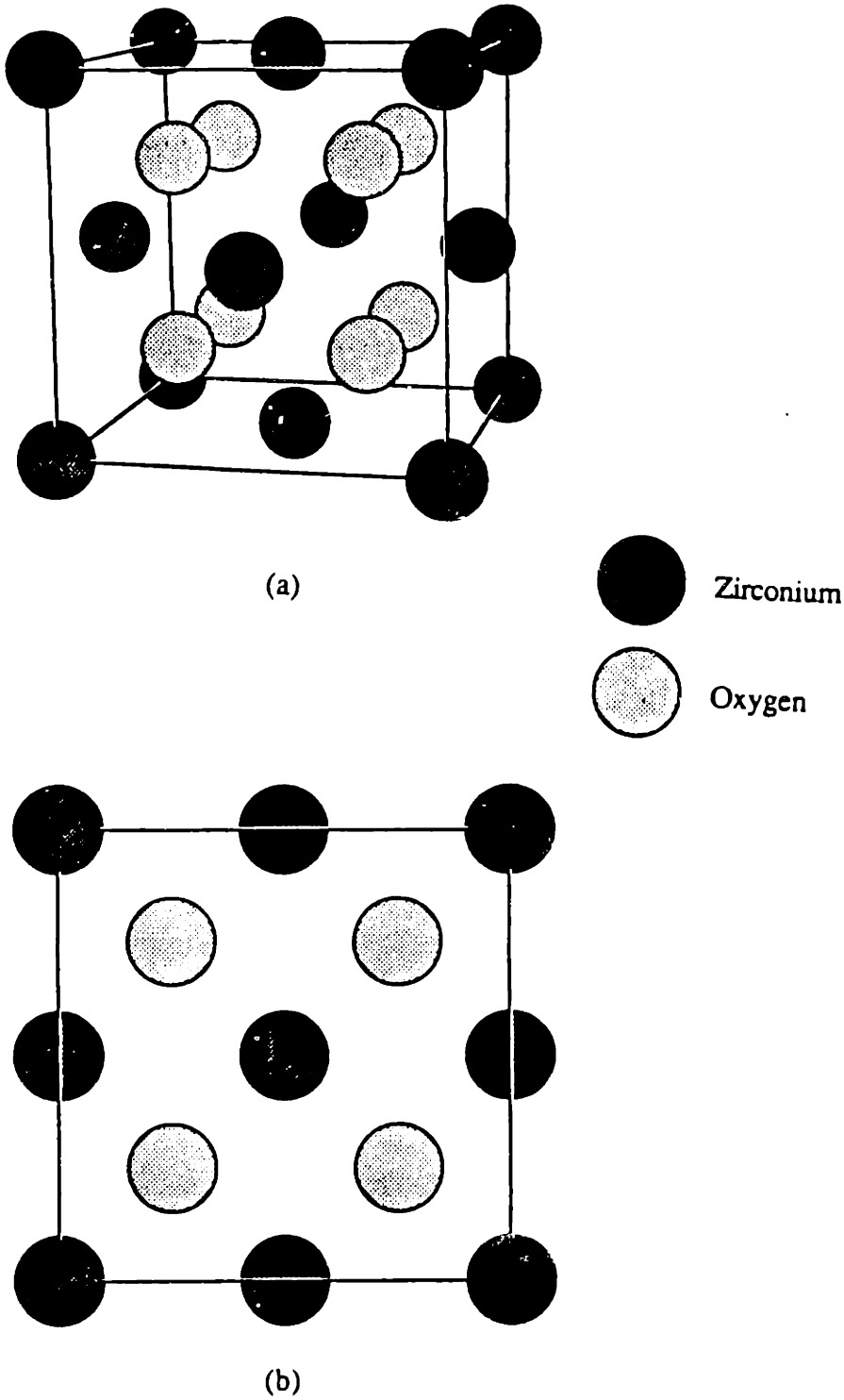

Figure 1.5
Cubic ZrO_2 (a) unit cell and (b) projection on the (100) plane.

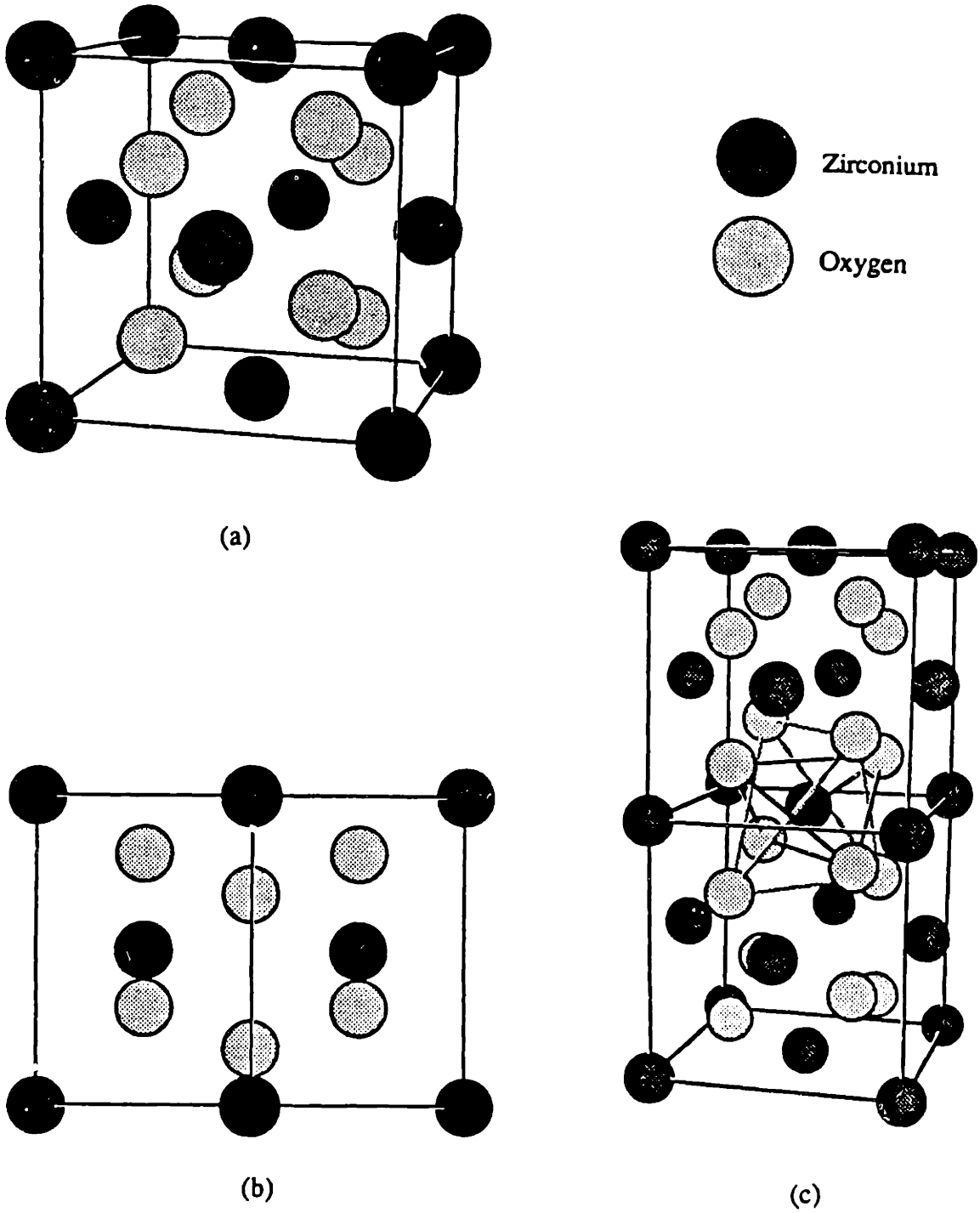

Figure 1.6
Tetragonal ZrO_2 (a) unit cell, (b) projection on the (110) plane and (c) two unit cells showing the 8-fold coordination of oxygen.

(a)

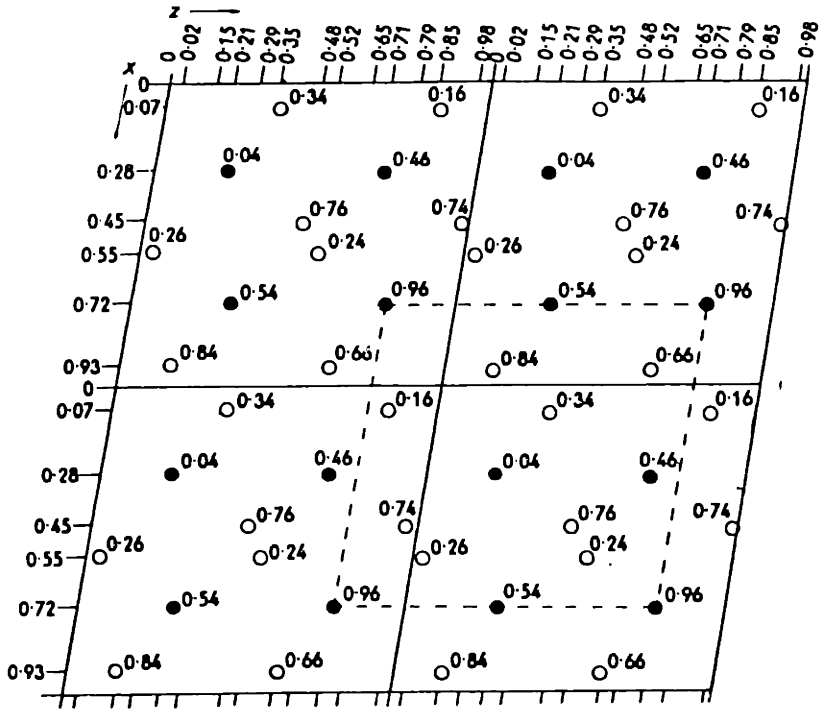

(b)

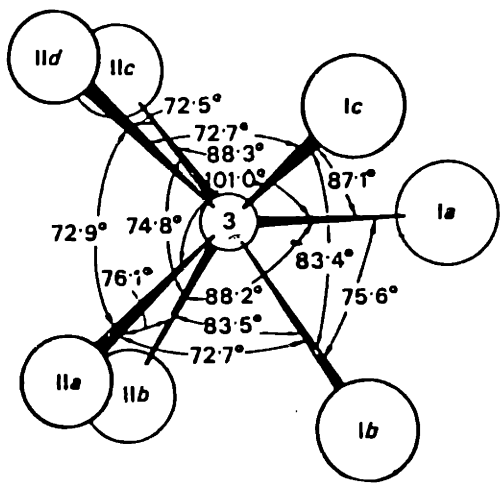

Figure 1.7
Monoclinic ZrO_2 (a) projection on the (010) plane [Wolten (1964)] and (b) angles and interatomic distances in the ZrO_7 polyhedron [Smith and Newkirk (1965)].

Phase	*Lattice Parameters (Å)*				*Space Group*	*Density* (gm/cm^3)
	a	b	c	β		
Monoclinic	5.1881	5.2142	5.3835	81.22°	$P2_1/c$	5.56
Tetragonal	5.1485	5.2692			$P4_2/nmc$	6.10*
Cubic	5.124				Fm3m	6.09*

Table 1.1. Crystallographic information on the zirconia polymorphs.
* indicates a calculated density.

1.5.2 Mechanical Stabilization of Tetragonal Zirconia

In examining particles of ZrO_2 produced through precipitation of zirconyl nitrate, Garvie (1965) noticed that the tetragonal form was stable at room temperature for free standing particle sizes < 30 nm, and hypothesized that the surface energy of the monoclinic form must be greater than for the tetragonal form for this to occur. Other workers have suggested that the tetragonal form is stabilized in air due to surface adsorbed species [Mitsuhashi et al. (1974)].

Numerous other works have shown that t-ZrO_2 particles can be retained in high elastic modulus, low thermal expansion materials (eg., Al_2O_3, $MgAl_2O_4$) [Claussen and Jahn (1978), Evans and Heuer (1980)]. Thermal expansion mismatch between the matrix and the ZrO_2 particles causes compressive stresses to form around the ZrO_2 particle during cooling from processing temperatures. These compressive stresses prohibit the increase in volume necessary for the transformation to arise, and the tetragonal particles are retained in the matrix. The transformation temperature is a function of the size of the tetragonal particle and the material which surrounds it. In polycrystalline ZrO_2, the transformation occurs between 950°C to 850°C and is lower if the tetragonal particle is embedded in a higher elastic modulus material [Claussen and Ruhle].

Mechanical stabilization arises from surface energy and strain energy constraints imposed on the t-ZrO_2 particle, and can be expressed by:

$$\Delta G_{t\text{-}m} = \Delta G^{C}_{t\text{-}m} + \Delta G^{SE}_{t\text{-}m} + \Delta G^{S}_{t\text{-}m} \qquad (1.2)$$

where $\Delta G^{C}_{t\text{-}m}$ = the change in chemical free energy for the transformation, $\Delta G^{SE}_{t\text{-}m}$ = the change in strain energy due to the volume change and from thermal mismatch between the ZrO_2 particle and the surrounding matrix and $\Delta G^{S}_{t\text{-}m}$ = the change in surface free energy for the transformation = $\gamma_m A_m - \gamma_t A_t$, where γ_x is the surface energy of the particle and A_x is the surface area.

The transformation will not occur if the strain energy and surface energy terms overwhelm the chemical driving force for the transformation. For small particles, the surface energy term will be the dominant one. For spherical particles embedded in a matrix of a different material, the stress term can be expressed by [Selsing (1961)]:

$$\sigma_{ij} = \frac{\Delta\alpha\, \Delta T}{\frac{1+\nu_m}{2E_m} + \frac{1-2\nu_m}{E_p}} \qquad (1.3)$$

where $\Delta\alpha = \alpha_m - \alpha_p$, the difference between the thermal expansion coefficients between the matrix (m) and the particle (p), and $\Delta T = T_r - T$, ν is Poisson's ratio, and E is the elastic modulus. The strain energy term is $1/2\ \sigma_{ij}\, d\varepsilon_{ij}$. For ZrO_2 particles embedded in an Al_2O_3 matrix, the stress field in the matrix around the particle is negative and the stress field in the particle is positive. Due to the higher elastic modulus of Al_2O_3, this causes the retention of t-ZrO_2. Table 1.2 lists some of the thermal and elastic properties of Al_2O_3 and ZrO_2.

	Al_2O_3		ZrO_2	
	20°C	1000°C	20°C	1000°C
E (GPa)	399	386	233	160
α ($x10^{-6}$ K^{-1})	5.4(11[a],10[c])	9.6	8.8(6-9)	10.5
ν	0.27	0.35	0.2	

Table 1.3 Some elastic properties of Al_2O_3 and ZrO_2.

1.5.3 Chemical Stabilization of Tetragonal and Cubic Zirconia

Additions of aliovalent cations to the ZrO_2 system creates vacancies on the oxygen sublattice:

$$Y_2O_3 \xrightarrow{2ZrO_2} 2Y'_{Zr} + 3O_O + V_O^{\cdot\cdot}$$

$$MgO \xrightarrow{ZrO_2} Mg''_{Zr} + O_O + V_O^{\cdot\cdot}$$

The creation of these vacancies is thought to stabilize the cubic (at higher concentrations) or tetragonal (at lower concentrations) polymorphs. Ho (1982) has proposed that zirconium ions in all of the polymorphs prefer a 7-fold coordination of oxygen, and that the lattice arranges itself to achieve that symmetry. Through the creation of vacancies, the coordination number of the zirconium atom is decreased for the tetragonal and cubic lattices, thereby reducing the normal fluorite structure of 8-fold to a 7-fold coordination.

Another polymorph is found for Y_2O_3 contents between 2.8-6.4 mol% and is identified as the t'-ZrO_2 phase, a tetragonal phase which does not transform to monoclinic under an applied stress. This phase indexes to the well-known tetragonal structure by x-ray diffraction and is only distinguished from it in the electron microscope in showing APD-type boundaries.

1.5.4 Alumina Polymorphs

There are 12 reported polymorphs of Al_2O_3 in the JCPDS card files. Table 1.3 lists their structures and other physical data.

Poly-morph	*Lattice Type*	*Lattice Parameters (Å)*	*Density (gm/cm3)*	*Stability Range*
α	Trigonal	a=4.758, c=12.991	3.987	Ambient conditions
β	Hexagonal	a=5.64, c=22.65	4.01	(*)
χ	Hexagonal	a=5.64, c=8.64	(*)	Heating gibbsite to 470°C
χ	Cubic	a=7.95	(*)	α-Al(OH)$_3$ heated 1 hr, 800°C
δ	Tetragonal	a=7.943, c=23.90	3.653	γ–AlO(OH)—>γ—>δ at 750°C
ε	Hexagonal	a=7.849, c=16.183	(*)	High temperature, >1930°C
γ	Cubic	a=7.90	3.67	Slow trans. to α at 1000°C
η	Spinel	a=7.94	(*)	β-Al(OH)$_3$ heated 640 hrs at 400°C
ι	(*)	(*)	(*)	Quenching from melt, 1% SiO_2
κ	(*)	(*)	(*)	α-Al(OH)$_3$ heated 1 hr, 1000°C
θ	Monoclinic	a=5.70, b=2.90 c=11.80, β=104.5°	3.585	β-Al(OH)3 heated 1 hr, 1100°C, dry air

Table 1.3 Summary of some crystallographic and physical data for the 12 polymorphs of Al_2O_3 found in the JCPDS cards. (*) indicates no available data.

As seen in the above table, Al_2O_3 can exist in a variety of forms. The evolution of these structures is dependent on thermal conditioning and the processing route. Many of these polymorphs are formed for small grain sizes and are dependent on the processing route. For example, sol-gel processing of Al_2O_3 results in the successive appearance of $\gamma \rightarrow \delta \rightarrow \theta \rightarrow \alpha$ polymorphs [Pierre (1985)].

1.6 Solidification Theory and Microstructural Development

Although rapid solidification is a non-equilibrium process on the whole, it can be assumed that free energies of the individual phases are known at a given point by the composition and temperature. Expressions governing growth from the melt must include mass and heat transfer balances across the moving interface. Baker and Cahn (1976) have described a mathematical treatment for the solidification process which assumes that:

(1) The temperature remains continuous across the interface, regardless of how fast the heat is extracted.

(2) Heat is conserved across the interface.

$$K_s(\nabla \underline{T} \cdot \underline{n})_s - K_L (\nabla \underline{T} \cdot \underline{n})_L = L_m V$$

where K_s and K_L are the heat transfer coefficients for the solid and liquid, respectively, $\nabla \underline{T}$ is the temperature difference between the solid and liquid, $\underline{n}$ in the normal vector to the interface, L_m is the latent heat of fusion and V is the velocity of the interface.

(3) Mass is conserved for each component

$$D_s (\nabla \underline{C} \cdot \underline{n})_s - D_L (\nabla \underline{C} \cdot \underline{n})_L = (C_s - C_L) V$$

where D_s and D_L are the diffusion coefficients for the solid and liquid, respectively and $\nabla \underline{C}$ is the composition gradient across the interface.

(4) Thermodynamic response functions which define the instantaneous conditions at the interface must be identified. One of the functions defines the interfacial temperature dependence on the velocity, and the other defines the liquid and solid compositional dependence on the velocity. The kinetic undercooling $f(v,C_L^*)$, has the property that $f(0,C_L^*) = 0$, and the velocity dependent partition coefficient $k_e g(v,C_L^*)$, has the property that $k_e g(0,C_L^*) = k_e$.

With these assumptions in mind, predictions about the microstructural development of a rapidly solidified material can be formulated.

1.6.1 Eutectic Growth

Eutectic growth is the cooperative growth of two phases occurring simultaneously, and results in a rod or lamellar type microstructure. For oxides, not only does a minimization of lattice mismatch between the two phases control the type of microstructure, but the charge balance across the interface is important. These two criteria result in oxide systems which possess highly oriented, esthetically pleasing microstructures. In addition, the solidification rate and amount of undercooling achieved in each phase will influence whether the growth is fibrous or lamellar.

The undercooling at the interface is equal to the sum of the undercooling due to capillarity effects and from constitutional supercooling. This can be written as [Kurz (1986)]:

$$T_E - T_I = \Delta T = \frac{A_1}{D_L(T_I)}\lambda V + \frac{A_2}{\lambda} \qquad (1.4)$$

where:

$$A_1 = \frac{m\Delta C}{8} \qquad (1.5)$$

$$A_2 = \frac{2\gamma_{\alpha\beta}}{\Delta S} \qquad (1.6)$$

where T_E is the eutectic temperature, T_I is the interface temperature, V is the velocity of the interface, λ is the interlamellar spacing, m is the slope of the liquidus, ΔC is the compositional difference between the two solid phases, $\gamma_{\alpha\beta}$ is the surface energy between the two phases, ΔS is the average entropy of fusion of the solid phases, D_L is the liquid interdiffusion coefficient. This equation predicts a maximum interfacial growth velocity for a crystalline material, which is determined by taking the derivative of Eq. 1.4 with respect to λ:

$$V_{max} = \frac{D_L T_I (\Delta T)^2}{4 A_1 A_2} \quad , \qquad (1.7)$$

and

$$\lambda^2 V = \frac{D_L T_I A_2}{A_1} = K. \qquad (1.8)$$

Eq (1.7) predicts that a maximum velocity can be obtained for a given interfacial undercooling. The constant K in Eq (1.8) for the Al_2O_3-ZrO_2 eutectic composition has been determined to be 1×10^{-17} m^3/sec by Cocks et al. (1974) through unidirectional solidification studies. If the interface moves at a faster rate, amorphous materials are formed. Eq (1.8) can also be applied to ternary eutectics. Echigoya et al. (1986) have published the solidification microstructure of the Al_2O_3-Y_2O_3-ZrO_2 eutectic grown at a rate of 2.8×10^{-6} m/sec. Measurements of the interlamellar spacing average ~1 μm gives the constant equal to 2.8×10^{-18} m/sec in Eq 1.8. Then, for a given undercooling, the maximum interfacial velocity for solidification of crystalline materials is greater in the Al_2O_3-ZrO_2 eutectic than for the Al_2O_3-Y_2O_3-ZrO_2 eutectic. This suggests that under the same experimental conditions, it should be easier to form amorphous Al_2O_3-Y_2O_3-ZrO_2 eutectics than Al_2O_3-ZrO_2 eutectics.

Coupled growth (cellular or eutectic) can occur at compositions other than the eutectic at very high and very low growth rates. The cooperative growth at high growth rates is a consequence of minimizing the interfacial area between the liquid and solid, and at low growth rates due to the steep thermal gradient from the solid to the liquid. In both cases, perturbations are inhibited and the typical dendrite plus eutectic microstructure expected in the off eutectic compositions is not observed.

1.6.2 Dendritic Growth

Dendritic growth occurs when perturbations on the liquid-solid interface are able to form and grow into the liquid, in a growth velocity regime between the limits:

$$v < \frac{G^* D_L}{\Delta T} = \frac{G^* D_L k_E}{m (1-k_E) C_o} \tag{1.9}$$

$$v > \frac{D_L \Delta T}{k_E T_M \Gamma} = \frac{m D_L (1-k_E) C_o}{k_E^2 T_M \Gamma} \tag{1.10}$$

where

$$G^* = \frac{k_L G_L + k_S G_S}{(k_L + k_S)} \tag{1.11}$$

where ΔT is the temperature difference between the liquid and solid, D_L is the diffusion coefficient in the liquid, k_E is the partition coefficient, m is the slope of the liquidus, C_o is the composition of interest, T_M is the melting temperature, Γ is the curvature, G_x is the thermal gradient in x, the liquid or solid and k_x is the thermal conductivity.

Boettinger (1982) has developed a set of microstructural possibility maps for binary eutectic phase diagrams from applying the thermodynamics and kinetics of solidification, as discussed in the above sections. Figure 1.8 shows three types of eutectic phase diagrams

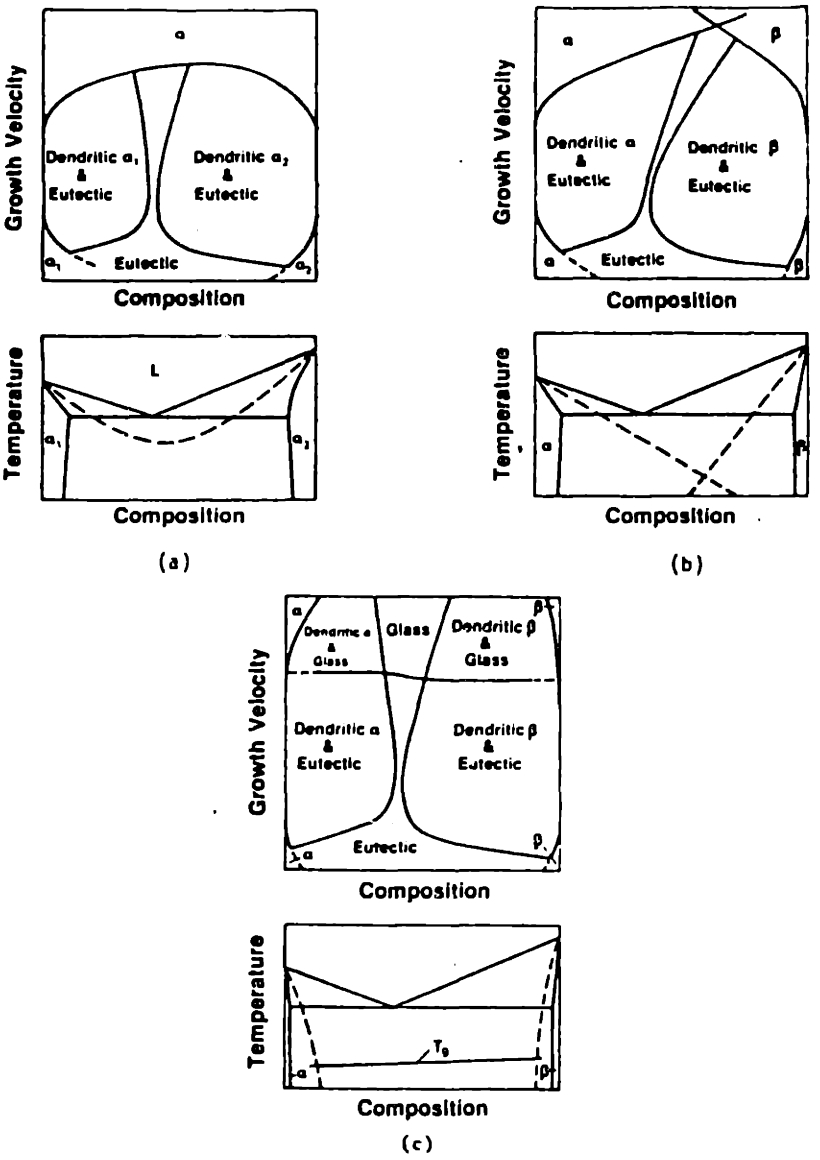

Figure 1.8
Growth velocity vs. composition plots of the microstructures expected for growth into a positive gradient for simple eutectic systems with (a) continuous T_o curves, (b) intersecting T_o curves and (c) non-intersecting T_o curves. From Boettinger (1982).

and their microstructural possibility maps. These possibility maps plot the expected microstructures as a function of growth velocity and composition. In Figure 1.8(a), the phase diagram shows the two phases to have continuous T_o curves across the compositional range. The T_o temperature is the point where the liquid and solid have the same Gibb's free energy, where massive solidification can take place, i.e., solidification without a change in composition. Continuous T_o curves imply that the two end phases have significant degrees of mutual solubility with respect to each other. Figure 1.8(b) shows a phase diagram where faceted growth occurs for at least one phase and the T_o curves intersect, implying some mutual solubility of the end members. Figure 1.8(c) shows a phase diagram for plunging T_o curves, where there is limited mutual solubility of the end members. This is the phase diagram most similar to the Al_2O_3-ZrO_2 phase diagram (see Figure 1.0).

According to this possibility map, there is a variety of microstructural features which can be expected for different growth velocities. For the eutectic composition, rod or lamellar eutectic growth is expected for low to moderate growth velocities and glass for higher velocities. For off-eutectic compositions, dendrites of the primary phase surrounded by eutectic material are expected for all velocities. If the growth rate is sufficiently high, the eutectic may form a glass. Only for extremely high growth rates are completely amorphous materials generated.

1.7 Devitrification of Glass

Nucleation of crystalline phases within highly metastable, rapidly solidified glasses can yield crystalline products which are supersaturated with one component. Consider the Gibbs free energy curves for a binary system, shown in Figure 1.9 (a) for a temperature above the melting point. The liquid has the lowest free energy curve and is flanked above by the crystalline free energy curves. If the liquid is rapidly quenched into a glass, it is metastable with a higher free energy than the crystalline phases, as shown in Figure 1.9(b). Heating the glass will result in the initial nucleation of a crystalline phase in a compositional range from C_1 to C_2, determined from the intersection on the crystalline free energy curve of the tangent from the starting composition C_o. The highest driving force for nucleation is for the equilibrium composition C_E but due to kinetic limitations a composition C_2 can form which is supersaturated with respect to C_E.

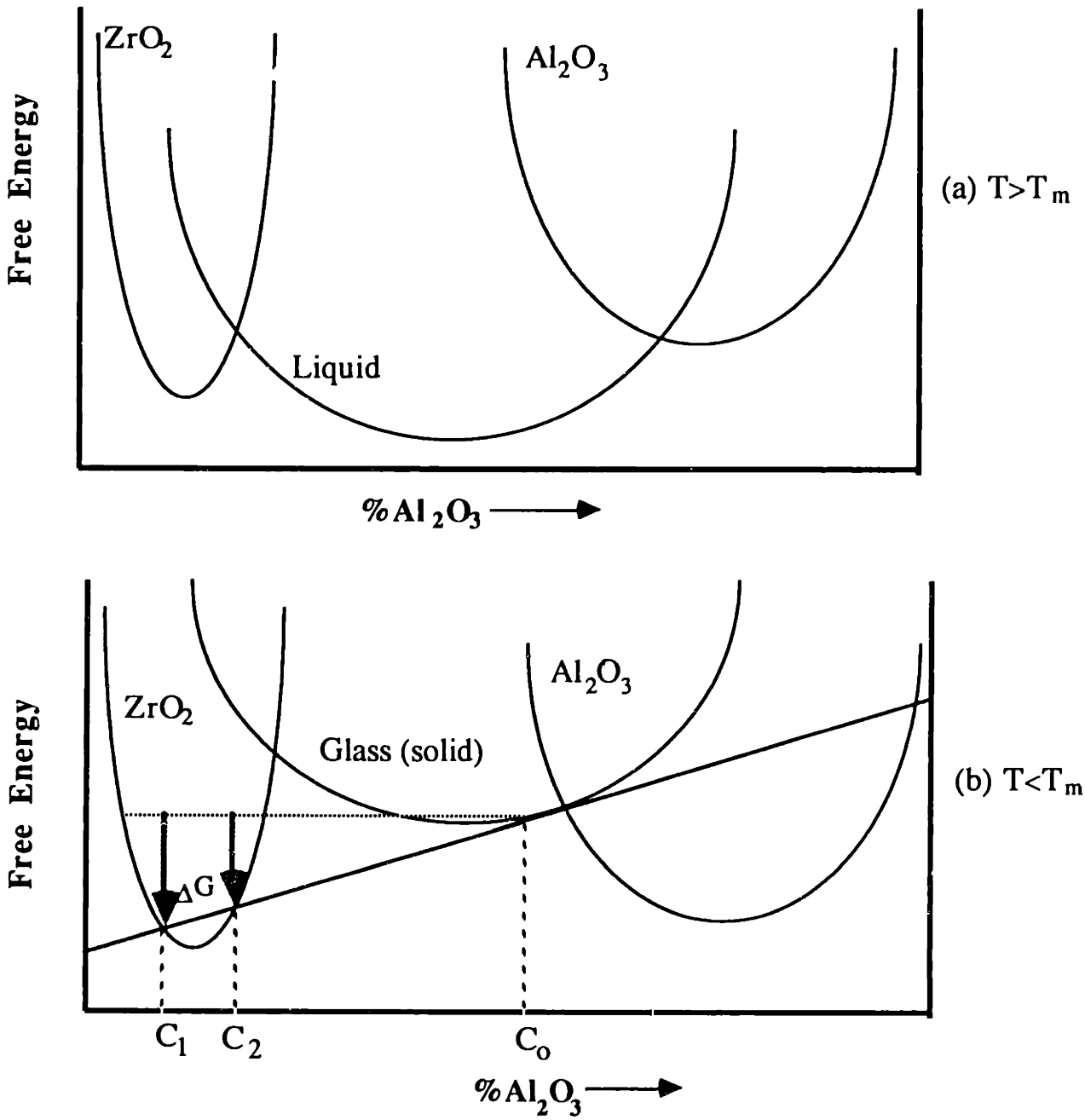

Figure 1.9

Free energy curves for (a) $T>T_m$ and (b) $T<T_m$.

1.8 Spectroscopy

Spectroscopic studies performed across the electromagnetic spectrum yields useful information about the structure and properties of glasses. Table 1.4 shows the typical regimes of interest and their corresponding energies and wavelengths.

	Microwave	*Far-Infared*	*Infared (IR)*	*Visible*	*Ultraviolet (UV)*
λ (cm)	0.1-30	0.001-0.01	0.00025-0.003	$3\text{-}7\text{x}10^{-5}$	$1\text{-}3\text{x}10^{-5}$
ν (Hz)	$10^{9}\text{-}3\text{x}10^{11}$	$3\text{x}10^{12}\text{-}3\text{x}10^{13}$	$10^{13}\text{-}1.2\text{x}10^{14}$	$4\text{x}10^{14}\text{-}10^{15}$	$10^{15}\text{-}3\text{x}10^{15}$
E (eV)	$4\text{-}1200\text{x}10^{-6}$	0.012-0.12	0.04-0.50	1.7-4.1	4.1-12.4
ν (cm^{-1})	0.03-10	100-1,000	300-4,000	14,000-33,000	33,000-100,000

Table 1.4. Regions in the electromagnetic spectrum with their corresponding wavelengths, frequencies and energies.

IR spectroscopic data are structure sensitive, while UV yields information about electronic transitions. Garnering information about the vibrational spectra of the molecules in oxides is typically done in the IR while far-infared is more informative for amorphous semiconductors. Glasses formed via rapid solidification have the potential to possess unusual optical properties by extending the transmission range in the IR and UV spectra. The incorporation of heavier atomic weight elements, which tend not to be glass formers under reasonable quenching rates, alters the fundamental vibrational frequencies and hence the IR adsorption frequency. In the UV region, however, the presence of short range disorder in the glasses will tend to broaden the adsorption edge. The different atomic configurations in a glass result in different electronic states.

The fraction of transmitted intensity is expressed by [modified Lambert's Law]:

$$\frac{I}{I_o} = (1\text{-}R)^2 e^{-\alpha t} \qquad (1.12)$$

where I_o is the incident intensity, I is the transmitted intensity, R $[=(n-1)^2/(n+1)^2]$ is the reflectance coefficient, α is the adsorption coefficient and t is the thickness. The adsorption coefficient $\alpha=2\pi K''/n\lambda$ where K'' is the relative dielectric loss factor, n is the index of refraction and λ is the wavelength. If scattering is present due to second phase particles, the measured adsorption coefficient incorporates a scattering coefficient which is proportional to the volume fraction of the second phase and inversly proportional to the diameter of the particle. For minor amounts of a second phase, the scattering coefficient only becomes important when the particle diameter is close to the wavelength of the incident radiation.

1.8.1 IR Spectroscopy

It is well known that glasses with high molecular weight elements exhibit IR transparency for longer wavelengths. The adsorption edge in the IR region is determined by the frequency of vibration of the cation-anion bonds. This frequency is only estimated for glasses because of the disordered network, and is expressed by:

$$\nu = \frac{1}{2\pi}\sqrt{\frac{k}{\mu}} \qquad (1.13)$$

where ν is the frequency of vibration, k is the elastic restoring force between two bodies of mass m_1 and m_2, and μ is the reduced mass $m_1m_2/(m_1+m_2)$. A general rule is that lower field strengths of both the cations and anions will move the IR transmittance to longer wavelenths. The field strength is Z/r^2 where Z is the ionic charge and r is the ionic radius. Table 1.5 shows the field strengths for the ions found in this work, along with two typical glass formers, Si and B, for comparison.

Element	*Charge*	*Mass (gm/mole)*	*Radius (nm)*	*Field Strength (Z/r^2)*
Al	+3	27	0.051	12
Mg	+2	24	0.067	5
Y	+3	89	0.092	3.5
Zr	+4	91	0.079	6.4
O	-2	16	0.132	1.15
Si	+4	28	0.042	23
B	+3	11	0.023	57

Table 1.5. Elements with ionic charge, mass, radius and calculated field strength [Dumbaugh (1985)].

As seen in the above table, Zr, Y and Mg additions to Al_2O_3-rich glass will reduce the field strength and possibly extend the range of the IR transparency. Al_2O_3-rich glasses will have more IR transmittance than, for example, silicate glasses. The adsorption edge for silicate glasses occurs between 4-5 μm (2000-2500 cm^{-1}) from the stretching vibration of the Si-O-Si bonds in 0.2 cm thick samples. The addition of CaO and Al_2O_3 moves the IR edge to longer wavelengths. Rapid solidification is an ideal technique in which to obtain glasses with high atomic weight elements in order to increase the IR transmitting range. Table 1.6 lists the IR adsorption edge wavelength and frequency for 10% transmission for the oxides examined in this work, along with SiO_2 for comparison. Data for ZrO_2 was not reported, but it is reasonable to assume that it has the longest adsorption wavelength from the field strength calculation shown in Table 1.5.

Compound	*IR Adsorption Edge (μm)*	*ν (cm^{-1})*
Al_2O_3	10.3	970
Y_2O_3	13.2	760
MgO	13.3	750
ZrO_2	(*)	(*)
SiO_2	7.4	1350

Table 1.6. IR adsorption edge for crystalline compounds Data taken from crushed samples embedded in IR transparent KBr powder. (*) not reported.

1.8.2 UV Spectroscopy

UV spectroscopy measures reflectivity or transmissivity in samples which have a band gap. The adsorption edge in the UV spectra indicates the energy of the optical band gap. There are two types of electronic transitions which may occur; an exiton, in which the electron increases in energy around an ion and is transferred from one orbital to another, or a charge transfer, in which the electron goes into the conduction band. For most glasses which contain light, electropositive cations, the conduction band lies at high energies and the UV adsorption is primarily due to exitons. In glasses containing heavier cations, the conduction band is at lower energies and may overlap the exciton levels. Glasses can transmit from the visible to the UV range up to the point where the energy in sufficient to cause electronic transitions. Table 1.7 lists the compounds examined with their electronic band gaps.

Compound	*Eg (eV)*
Al_2O_3	9.90
MgO	7.77
Y_2O_3	5.60
ZrO_2	4.99

Table 1.7. Compounds and their band gaps at 300 K
From Strehlow and Cook (1973).

2.0 EXPERIMENTAL TECHNIQUES

2.1. Specimen Preparation

The starting powders and their purity level are listed in Table 2.0. For all of the melting techniques used, the specimen size was a pellet, 1.27 cm in diameter and 2.54-3.81 cm in height. The powders were weighed to the desired composition, ball milled for 16 hours overnight, sieved with a 140 mesh (106 μm) screen, cold pressed under 69 MPa with a 1.27 cm die, and then sintered at 1000°C for at least 5 hours. It was not necessary to optimize the density of the pellets. High strength was not required for the subsequent melting experiments, only some chemical mixing was desired.

Oxide	*Purity*	*Major Impurities (by weight)*	*Supplier*
Al_2O_3	99.999%	22 ppm Si, 60 ppm Sn, 100 ppm Mo	Alfa Products
ZrO_2	99.99+	400 ppm Si, 400 ppm Ti, 400 ppm Ag 200 ppm Ba	Alfa Products
Y_2O_3	99.99%	Nd<0.01%, Ho, Dy, Lu, Gd, Tm, Yb, Er each < 0.0001%, and Sm, Si, Fe, Mg, Ca, Al each < 0.005%.	Alfa Products
MgO	99.5%	1880 ppm Si, 470 ppm B, 470 ppm Ca, 350 ppm Fe, 140 ppm Al, 140 ppm Mn	Alfa Products

Table 2.0

Starting powders with purity information.

2.2. Rapid Solidification Techniques

For this work, only substrate quenching was investigated. Five techniques were evaluated, three used flat substrates and two used the rotating cylinder approach.

2.2.1 Solar Splats

Al_2O_3-ZrO_2 eutectic splats were provided from the 3 kW solar furnace at the CNRS Laboratory in Odeillo (France). For this technique, the sample is melted by focusing the sun's rays on the sample placed on a water cooled copper substrate and then solidified by a metallic hammer which impacts the sample at a high speed [Foex et al. (1975)].

2.2.2 Laser Splats

Figure 2.0 shows the apparatus used to rapidly solidify the Al_2O_3–ZrO_2 eutectic and the 21.6 mol% ZrO_2 compositions. A 1500 W CO_2 laser was focused onto the end of a sintered rod of the desired composition. A molten droplet forms on the tip and

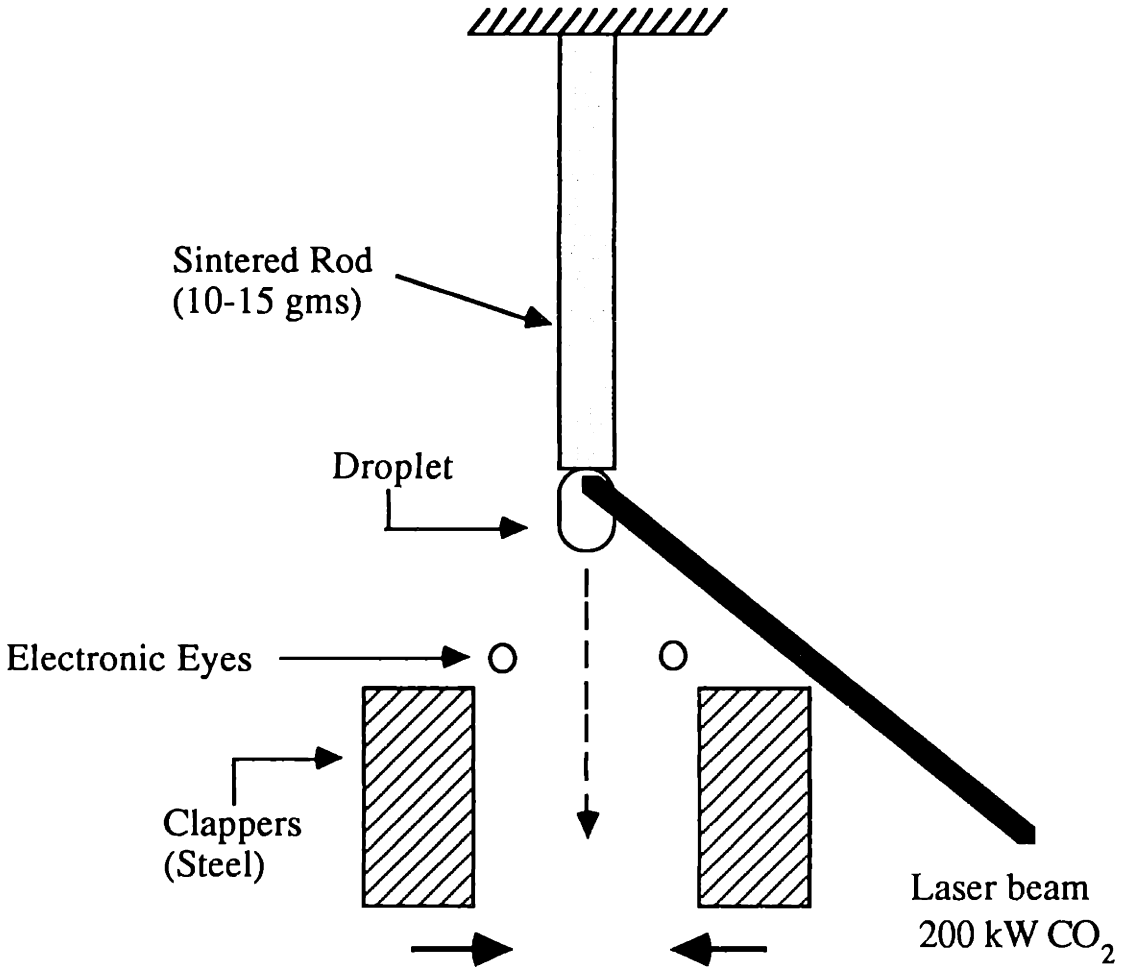

Figure 2.0

Laser splatting apparatus. A rod of sintered material is suspended above a set of electronic eyes, which trigger the clappers to close when the molted droplet passes through them. Clappers are made of stainless steel.

eventually falls under its own weight, which triggers a set of electronic eyes to smash a pair of copper platens on the melt. The double substrate method helps in rapid heat extraction of the melt through both surfaces. The Al_2O_3-ZrO_2 eutectic and hypereutectic compositions were rapidly solidified useing this technique.

2.2.3 Plasma Spraying

Powders, weighed and mixed to the desired composition, were fed into a Bay State[1] 40 KW unit and melted and sprayed with the Model P6-100 plasma gun on copper, glass and NaCl substrates. The heat in this case is most rapidly withdrawn through the bottom substrate although some is released in the air. The Al_2O_3-ZrO_2 eutectic composition was sprayed using this technique.

2.2.4 Melt Extraction

Figure 2.1 is a schematic of the melt extraction apparatus. An oxy-acetylene or H_2–O_2 torch is held in close contact with a sintered pellet of the desired composition. After a molten pool formed on the top of the pellet, which typically takes 1-2 minutes, a spinning copper wheel of 5.08 cm diameter with a flat surface is brought in contact with the melt. The molten material is solidified on the wheel and spun off into a collection chamber. Radial wheel speeds in the range of 800-1400 cm/sec yielded the greatest amount of amorphous materials. Faster wheel speeds tended to produce small, opaque spheres which had been solidified as droplets in air at a slower cooling rate. This indicates that faster wheel speeds produce too much turbulance in the air aboves the melt which would tend to break up the melt and scatter it as droplets. The Al_2O_3-ZrO_2 eutectic, hypereutectic and hypocutectic compositions were rapidly solidified using this technique.

2.2.5 Twin Rolling

Figure 2.2(a) shows a schematic of the main features of the twin-roller assembly along with a more detailed diagram of the twin roller assembly in Figure 2.3(b). This system was designed by Sasayama, Gomez and Geislinger in our laboratory [see Gómez

[1]Bay State Abrasives, Dresser Industrial Products Division, Westboro, MA

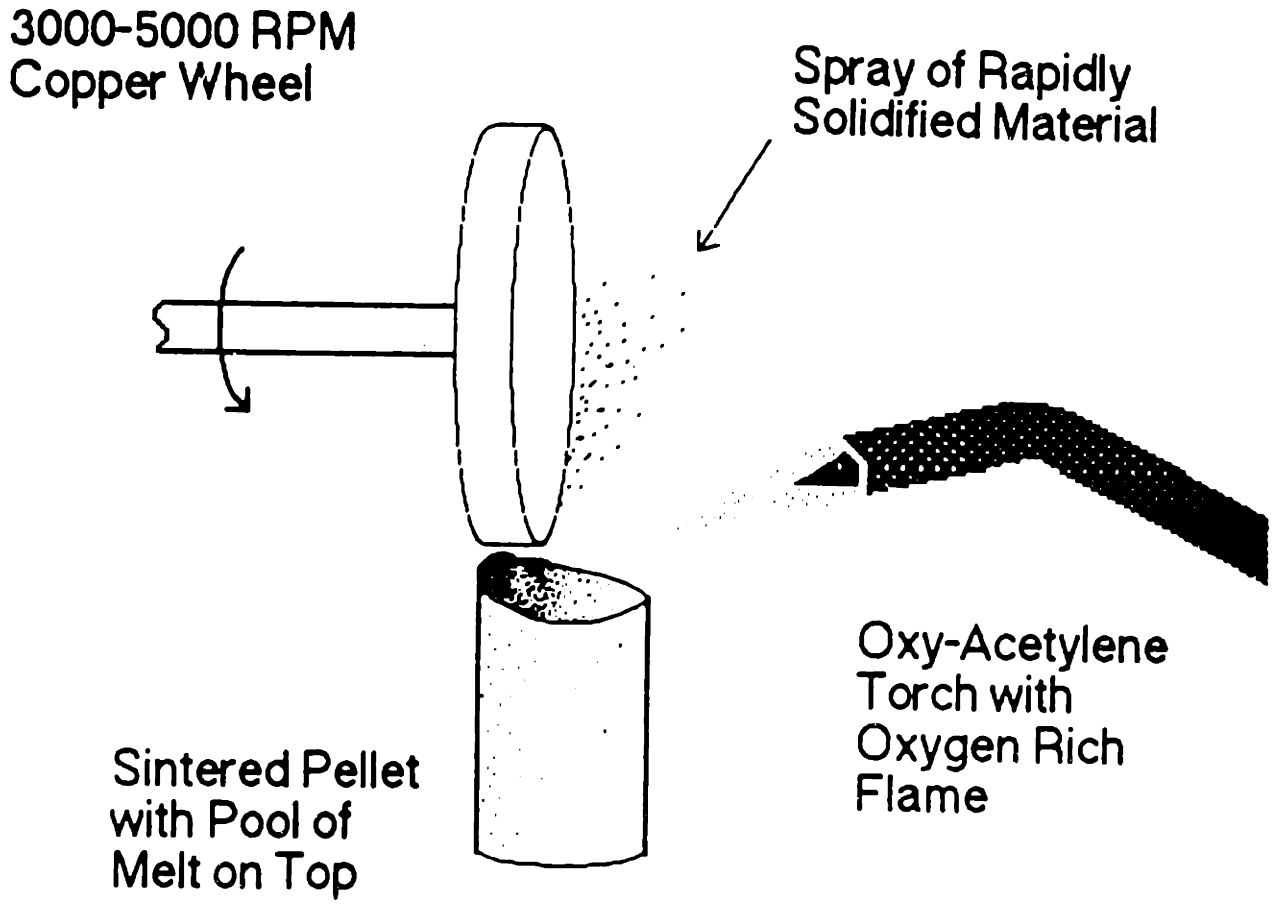

Figure 2.1.
Melt extraction apparatus.

(a)

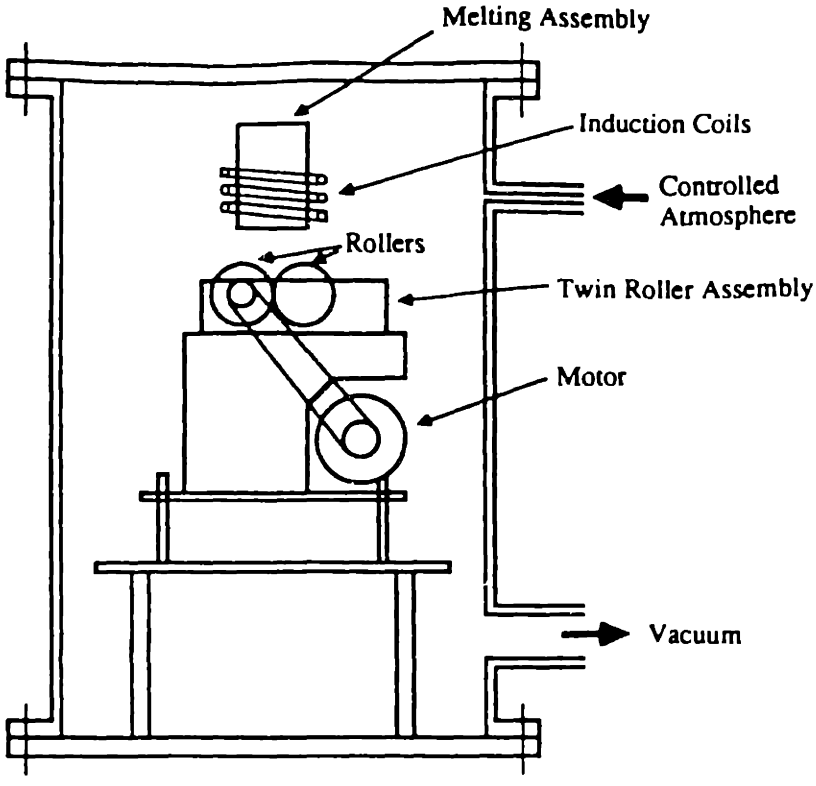

(b)

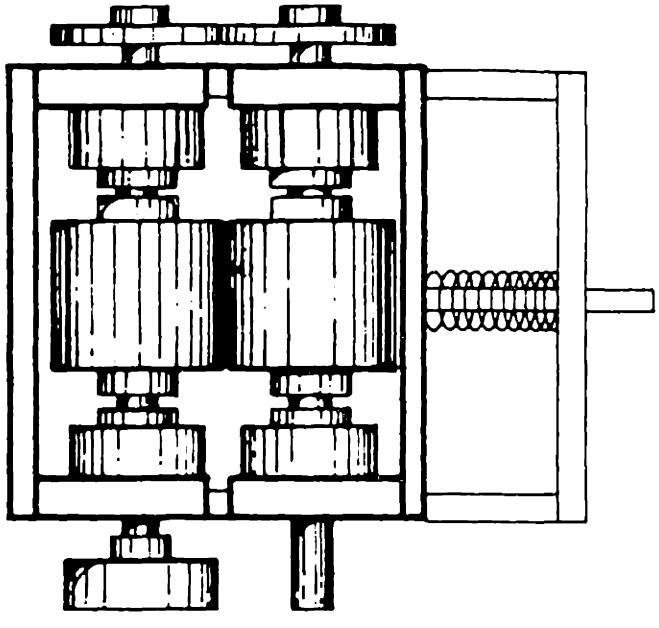

Figure 2.2
(a) Schematic diagram of the main features of the twin rolling device.
(b) Detailed diagram of the twin roller assembly. The rollers are 5.08 cm in diameter.

(1987) and Geislinger (1987) for a more detailed description of the apparatus]. The rollers are 5.74 cm in diameter and 5.08 cm long. The rollers are kept in contact with each other by a very stiff spring. One roller is belt driven by a 1/4 hp motor and the rollers are coupled by gears. The maximum speed the rollers can attain is 16 m/sec (6000 rpm).

It is important to choose rollers made of chrome plated steel, tool steel or any other high hardness steel. Quenching abrasive ceramics like Al_2O_3 and ZrO_2 can cause severe damage to "soft" rollers necessitating frequent replacement. Figure 2.3 shows the thickness of the quenched material as a function of the roller speed. As shown, for roller speeds > 11 m/sec (4000 rpm), the thickness of the flakes do not decrease substantially. This implies that substantial differences in cooling rates are not attained for increasing the wheel speed over 4000 rpm. The roller assembly is placed into a chamber previously designed for gas atomization of ceramics [DeGuire (1987)], as shown in Figure 2.4. Heating is provided by RF coupling through a copper coil from a dual frequency Lepel RF generator. Although the unit is capable of operating in the megacycle range, it was found that tuning the unit at 30 KHz with 30% total power melted all of the compositions within 10 min. Figure 2.5 shows the heating assembly used for melting the ceramic pellets. The pellet is glued with high temperature ZrO_2 cement to a disk of ZrO_2 insulating board and then suspended in the cavity of a graphite susceptor, which is surrounded by a ZrO_2 insulating cylinder. The whole assembly is fitted into the copper coil. The elegance of this method is that a crucible is not needed and thus there is no contamination of the melt, the temperature need not be measured, the insulation and susceptor can be reused repeatably, and the whole assembly can be put together quickly.

This technique is most successfully used with eutectic compositions or compounds which do not melt into a liquid-solid two phase region. If there is a large temperature difference between the solidus and liquidus, the sample could be solidified with a difference in liquid composition as a function of time. In other words, for an off-eutectic composition, the first liquid to form would be the eutectic and as heating and melting proceeded, the remaining liquid would become progressively rich in the primary phase.

The Al_2O_3-ZrO_2 eutectic, Al_2O_3-Y_2O_3-ZrO_2 eutectic and the two Al_2O_3-MgO-ZrO_2 eutectic compositions were rapidly solified using this technique.

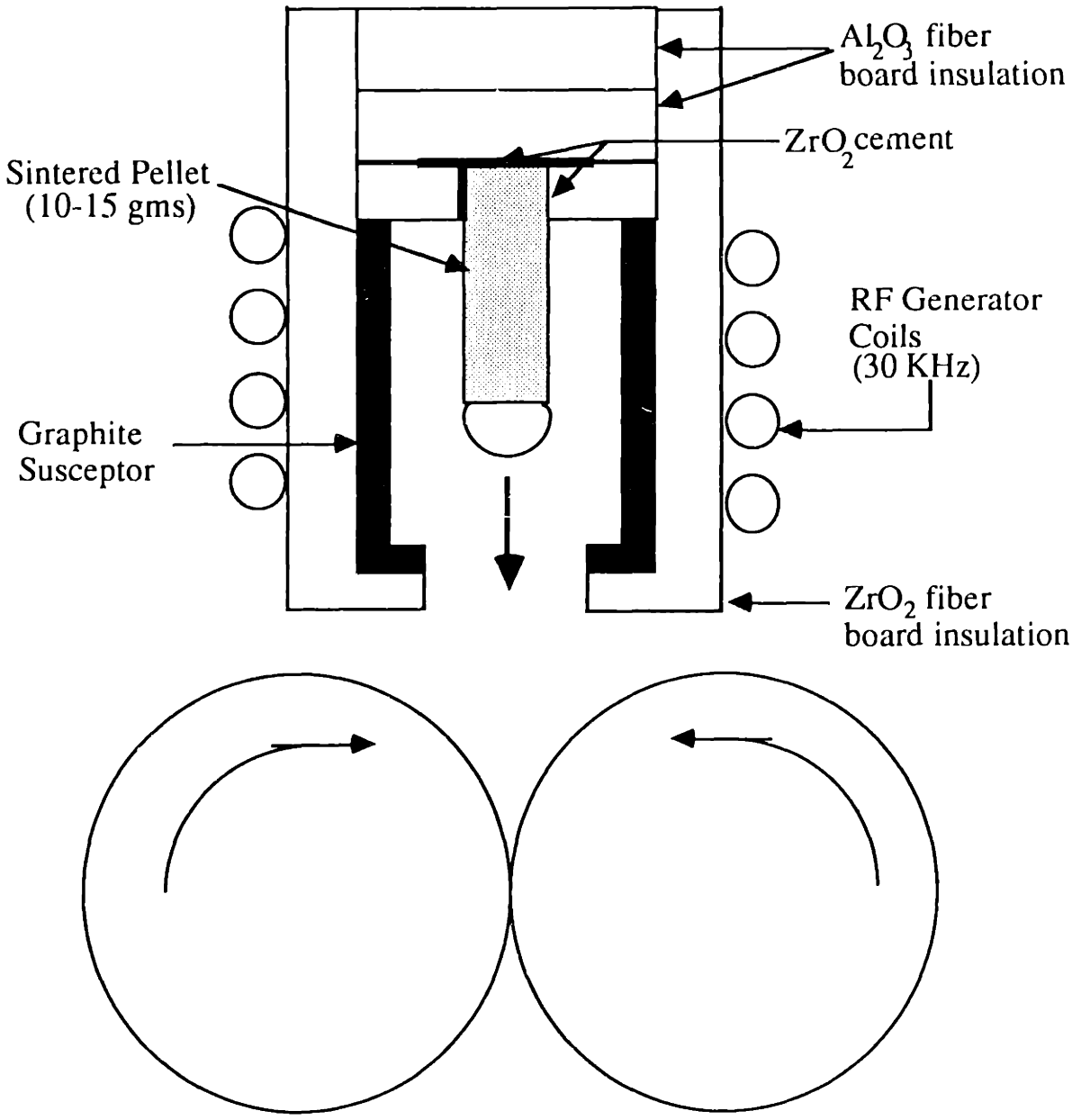

Figure 2.3

Twin rolling apparatus. The pellet is suspended in a graphite susceptor and is heated by convection. The molten droplet falls under its own weight between the rotating twin rollers.

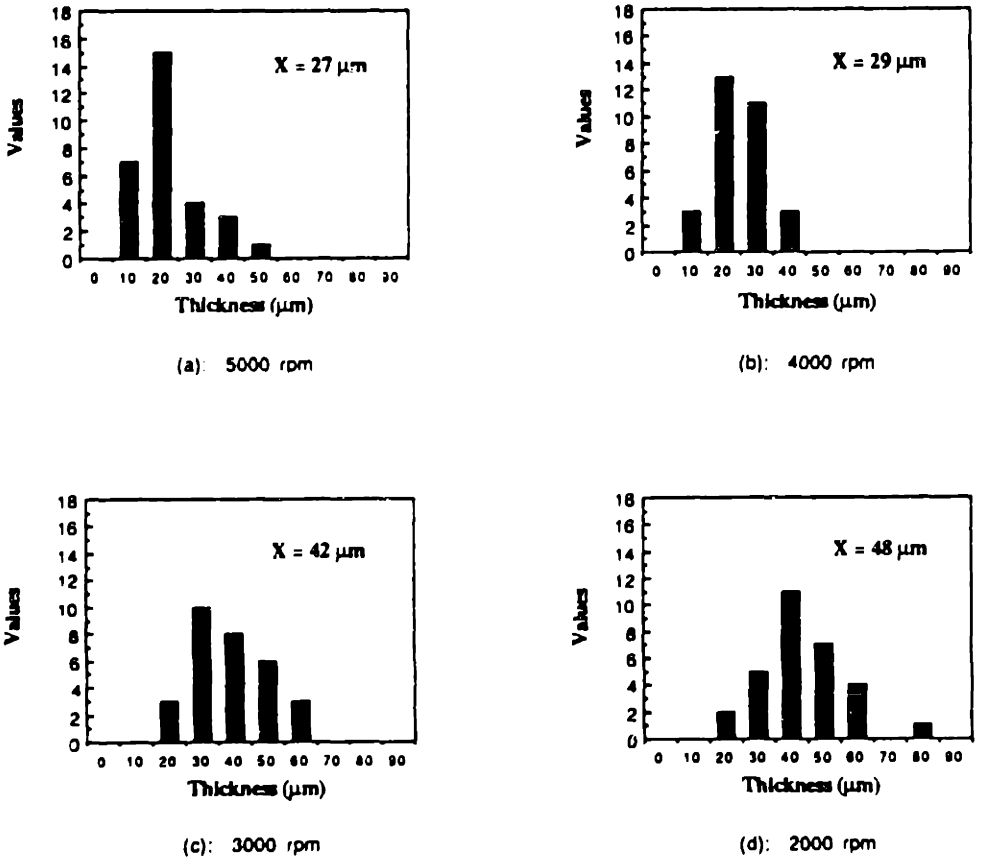

Figure 2.4
Distribution of the thicknesses of $KNbO_3$ flakes obtained by twin roller quenching as a function of roller speed. (a) 5000 rpm, (b) 4000 rpm, (c) 3000 rpm and (d) 2000 rpm.

2.3 Analytical Techniques

The Debye-Scherrer x-ray diffraction technique was used to evaluate the as-quenched and heat treated materials. A small flake was attached to a slender glass rod and inserted into a Gandolphi single crystal holder to ensure no orientation effects were recorded. Data was collected for 10–12 hours at 35 kV and 15 mA. A Rigaku[1] rotating anode diffraction unit operating at 40 kV and 200 mAwas used to examine powder from crushed flakes of a uniform thickness. Due to the x-ray power generated with this unit, only small amounts of sample are needed for accurate data collection. Typically sample sizes of < 500 mg were used.

Samples were thinned in an ion mill for TEM and STEM analysis at 6 kV and 1.5 mA. The materials produced were thin enough in the as-quenched condition to ion mill directly without preliminary grinding. Some samples were milled using a LN_2 cold stage to determine if ion beam heating effected the samples. The samples were sandwiched between two copper specimen support rings and clamped into the tantalum stage. If the samples were too small, they were glued with copper epoxy to the specimen supports. It was desirable to avoid using the epoxy as it tended to outgas in the STEM and cause contamination and charging of the specimen. The TEM used was a 200 keV JEOL 200 CX[2] fitted with a high resolution pole piece. The STEM used was a 100 keV VG HB-5[3] with a Link Systems[4] windowless energy dispersive x-ray analysis system and microdiffraction capabilities. The dual lens system in the microscope forms a probe size of approximately 1.5 nm in diameter on the specimen. With this probe it is possible to obtain the chemical composition and diffraction pattern of areas as small as 5 nm. Some of the samples were examined in the TEM with a hot stage, a single tilt holder capable of reaching 1350°C.

Spectrographic analysis was performed with a Beckman Acculab 10[5] IR spectrophotometer and on a vacuum ultraviolet (VUV) spectrophotometer designed and

---

[1] Rigaku USA, Danvers, MA 01923

[2] Japan Electron Optics Co., Tokyo, Japan

[3] Vacuum Generators Microscopes, East Grinstead, England

[4] Link Systems, High Wycombe, Bucks, England

[5] Beckman Instruments, Inc., 45 Belmont Drive, Somerset, New Jersey 08873

built at MIT by French (1985). The IR unit scans from 4000-250 cm^{-1} (2.5-40 μm wavelength) with a N_2 purge under ambient conditions. The samples were mounted directly into the holder which required a minimum sample size of ~1 cm x 1 cm. VUV spectroscopy was done in the transmission mode from 6-15 eV, which corresponds to a range of wavenumbers from 36,000-55,000 cm^{-1} (180-280 nm wavelength) range. The samples were mounted directly into the holder and required a minimum size of 1 cm x 1 cm.

DTA experiments were carried out on a Perkin-Elmer[1] unit in air with heating and cooling rates of 10-20°C/minute. Density measurements were taken with a stereo pychnometer. Annealing experiments were performed in air in a commercial furnace capable of maintaining temperatures between 800-1700°C. Samples were placed in the furnace at the set temperature, allowed to anneal at the desired time and then were quickly removed from the furnace and air cooled.

3.0 EXPERIMENTAL RESULTS AND DISCUSSION

3.1 Materials Systems Examined

Three compositions in the Al_2O_3-ZrO_2 binary system were rapidly solidified, the eutectic of 62.5 mol% (58 wt%) Al_2O_3-37.5 mol% (42 wt%) ZrO_2, a hypo-eutectic of 78.4 $^{m}/_{o}$ (75 $^{w}/_{o}$) Al_2O_3 - 21.6 $^{m}/_{o}$ (25 $^{w}/_{o}$) ZrO_2, and a hyper-eutectic of 28.3 $^{m}/_{o}$ (25 $^{w}/_{o}$) Al_2O_3-71.3 $^{m}/_{o}$ (75 $^{w}/_{o}$) ZrO_2. The liquidus temperature for the three compositions were determined from the phase diagram shown in Figure 1.0.

The eutectic in the Al_2O_3-Y_2O_3-ZrO_2 ternary system 59 $^{m}/_{o}$ Al_2O_3-4.2 $^{m}/_{o}$ Y_2O_3-36.8 $^{m}/_{o}$ ZrO_2 (52.3 $^{w}/_{o}$ Al_2O_3-8.2 $^{w}/_{o}$ Y_2O_3-39.4 $^{w}/_{o}$ ZrO_2) was also examined along with the two ternary eutectics in the Al_2O_3-MgO-ZrO_2 system, an Al_2O_3-rich composition of 42.1 mol% (43 wt%) Al_2O_3-17.4 mol% (7 wt%) MgO-40.5 mol% (50 wt%) ZrO_2 and a MgO-rich composition of 16.6 mol% (20 wt%) Al_2O_3-42.1 mol% (20 wt%) MgO-41.3

[1]Perkin-Elmer Co., Norwalk, CT 06856

mol% (60 wt%) ZrO_2. The eutectic temperature for the Al_2O_3-Y_2O_3-ZrO_2 eutectic was not reported. The eutectic temperatures for the Al_2O_3-MgO-ZrO_2 compositions were determined by Bierezhnoi and Kordyuk (1964). Table 3.0 lists the compositions and melting temperatures of all of the compositions examined.

	Compositions mol% (wt%)				*Melting Temperature (°C)*
	Al_2O_3	MgO	Y_2O_3	ZrO_2	
Al_2O_3-ZrO_2 eutectic	62.5(58)			37.5(42)	1870
Al_2O_3-ZrO_2 hypoeutectic	78.4(75)			21.6(25)	2000
Al_2O_3-ZrO_2 hypereutectic	28.3(25)			71.3(75)	2100
Al_2O_3-Y_2O_3-ZrO_2 eutectic	58.8(52.3)		4.2(8.3)	36.9(39.4)	*
Al_2O_3-rich ternary eutectic	42.1 (43)	17.4 (7)		40.5 (50)	1830
MgO-rich ternary eutectic	16.6 (20)	42.1 (20)		41.3 (60)	1840

Table 3.0. Compositions and melting temperatures of the Al_2O_3-ZrO_2 eutectic, hypoeutectic and hypereutectic, the Al_2O_3-Y_2O_3-ZrO_2 eutectic and the two Al_2O_3-MgO-ZrO_2 ternary eutectics examined in this work.* Not reported.

3.2 As-Quenched Materials

3.2.1 Visual examination of flakes, thickness

Figure 3.0(a) shows the dimensions of the Al_2O_3–ZrO_2 eutectic materials produced through the laser splat technique, melt extraction and twin rolling. The laser splats were mostly opaque and greyish colored. This indicates that the Al_2O_3 and/or the ZrO_2 was reduced. Other workers [Peterson (1986)] have found that the rapidly solidified eutectic Al_2O_3–ZrO_2 grey and black colored materials turn white when annealed in O_2. The laser splats are from 90–100 μm thick. The melt extracted solidified material was in the shape of small flakes which ranged in size from 1–4 mm in length, 1–2 mm in width and 100–250 μm in thickness. Many of the flakes are transparent, as shown in Figure 3.0(b), and some are microcrystalline with amorphous regions only around the perimeter of the flake. The twin rolling technique produced the thinnest flakes with the largest surface area. Flakes generated from this technique contain the greatest amount of amorphous materials and range in thickness from 10–50 μm, as shown in Figure 3.0(c). Table 3.1 summarizes the size and shapes of the materials produced through different rapid solidification techniques.

3.2.2 X-ray diffraction results

X-ray diffraction patterns revealed only the low angle amorphous hump in all of the compositions for the thinnest flakes produced by the twin-rolling technique. Since there was a distribution of thicknesses, the thicker flakes showed some crystallinity along with amorphous materials. Table 3.2 summarizes the x-ray diffraction results for the as-quenched, microcrystalline materials of different compositions.

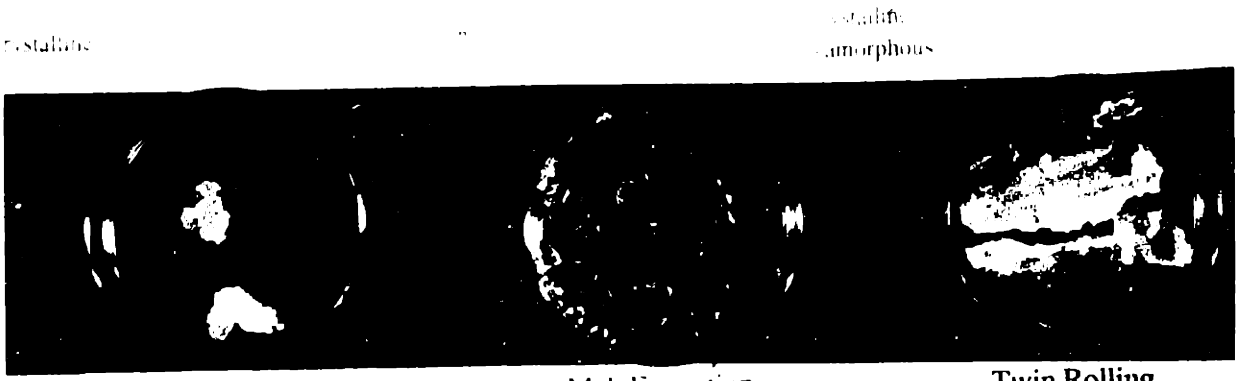

Figure 3.0
(a) Materials produced through laser splatting. (b) Materials produced through melt extraction. (c)Materials produced through twin rolling.

Technique	*Compositions*	*Materials Produced*	*dT/dt (K/sec)(*)*
Laser Splatting	Al_2O_3-ZrO_2 eutectic Al_2O_3-ZrO_2 hypereutectic	White and grey flakes, 90-150 μm thick 1 cm in diameter	10^3-10^4
Melt Extraction	Al_2O_3-ZrO_2 eutectic Al_2O_3-ZrO_2 hypereutectic	Transparent and white opaque flakes, 50-250 μm thick, 0.05 cm-0.3 cm in width, 0.3-0.8 cm in length	10^4-10^7
Twin Rolling	Al_2O_3-ZrO_2, Al_2O_3-Y_2O_3-ZrO_2, and Al_2O_3-MgO-ZrO_2 eutectics	Transparent and opaque white flakes, 50-1500μm thick 0.3-2.0 cm in width 0.3-5.08 cm in length	10^5-10^8
Solar Splats	Al_2O_3-ZrO_2 eutectic	White flakes, 100-300 μm thick	10^3-10^4
Plasma Spraying	Al_2O_3-ZrO_2 eutectic	Transparent and transluscent	10^6-10^8

Table 3.1. Summary of the resuits of visual examination of the quenched materials with their estimated quench rates for the different rapid solidification techniques.

Eutectic Composition (mol%)	*Phases Present (mol% MgO or Y_2O_3)*
62.5 Al_2O_3-37.5 ZrO_2	t-ZrO_2 + glass
58.8 Al_2O_3-4.2 Y_2O_3-36.9 ZrO_2	c-ZrO_2(10.22) + glass
42.1 Al_2O_3-17.4 MgO- 40.5 ZrO_2 (Al_2O_3-rich)	Spinel (22.1), m+c-ZrO_2 (11.6) + glass
16.6 Al_2O_3-42.1 MgO-41.3 ZrO_2 (MgO-rich)	Spinel (46.2), c-ZrO_2 (22.2), MgO+ glass

Table 3.2 Summary of the x-ray diffraction results on the as-quenched crystalline materials produced by twin rolling.

As seen from Table 3.2, in all of the compositions but the MgO-rich ternary eutectic, the nucleation of at least one phase has been suppressed. In the Al_2O_3-ZrO_2 eutectic, only the t-ZrO_2 phase nucleated during the solidification process. The presence of the c-ZrO_2 phase could not be detected. In the Al_2O_3-Y_2O_3-ZrO_2 eutectic, the c-ZrO_2 phase nucleated, leaving an Al_2O_3-rich glass. Nucleation of Al_2O_3 from the melt in the ternary Al_2O_3-rich eutectic composition is inhibited but nucleation of MgO in the ternary MgO-rich eutectic composition occurred. The MgO-Al_2O_3 binary phase diagram shown in Figure 1.4 shows that the spinel phase can range from ~15-60 mol% MgO. The spinel phase in the Al_2O_3-rich ternary eutectic is highly defective with only 18.3 mol% MgO in the compound. The spinel phase in the MgO-rich ternary eutectic is slightly Al_2O_3-rich with 42.5 mol% MgO. The absence of one primary phase in the Al_2O_3-rich system may indicate that surface energy constraints limit the nucleation of that phase to decrease the total

interphase boundary energy. It is not surprising that Al_2O_3 formation is supressed due to the lattice mismatch with the other cubic phases.

It appears that significant supersaturation of MgO in ZrO_2 cannot occur through rapid solidification. As seen in the binary phase diagram, c-ZrO_2 coexists with MgO in a compositional range of 12 mol% MgO and up. Although it is possible to suppress the nucleation of one phase, thereby enriching the other phases(s) in that component, this scenario would require that the MgO content in the ZrO_2 phase to be ~30 mol% in the MgO-rich composition, which corresponds to the compound $Mg_2Zr_5O_{12}$.

No evidence was found in the x-ray diffraction data for the presence of the fluorite related supersturctures, $Mg_2Zr_5O_{12}$ (δ phase, 28.6 mol% MgO) or $MgZr_6O_{13}$ (γ phase, 14.3 mol% MgO). Delamarre (1965) first identified the δ phase in specimens cooled from the melt in a compositional range of 25-35 mol% MgO. It is isostructural with the $Zr_3Sc_4O_{12}$ phase. Rossell and Hannink (1984) found this phase after rapid cooling from the melt a composition of 28.6 mol% MgO or air quenching from T >1900°C. In contrast, Sim and Stubican (1987) identified the δ phase only in samples of 12-21 mol% MgO which were furnace cooled from 2035°C or in samples annealed at 800°C for long periods after rapid quenching from 2035°C. The results in this work agree with Sim and Stubican's results. Readey et al. (1988) were the first to tabulate the x-ray d-spacings for this phase, which they found after annealing Mg-PSZ for 20 min. at 1000°C, but not at temperatures >1200°C.. Unfortunately, the two most intense d-spacings fall close to the $\{111\}_{c+t}$ and $\{220\}_{c+t}$ peaks.

Rossell and Hannink (1984) first identified the $MgZr_6O_{13}$ phase, isostructural with the $Zr_5Sc_2O_{13}$ phase, in samples rapidly quenched from the melt but concluded that the presence of this phase was due to MgO evaporation during the experiment. Sim and Stubican (1987) could not distinguish between the δ and γ phases because the x-ray lines overlap, but found electron diffraction spots which could be assigned to the γ phase in samples slowly cooled from T>2000°C.

The presence of m-ZrO_2 in the Al_2O_3-rich composition can be expained by two factors: (1) From the analysis performed on the x-ray data on the as-quenched materials, MgO vaporization occured during melting. The molten material at the surface of the droplet vaporized as it formed and grew on the pellet. If partial nucleation of ZrO_2 also occured on the surface of the droplet as it is melting, then m-ZrO_2 would form on the surface. (2) Total melting was not attained in the droplet. The starting powder consisted of m+ZrO_2 + spinel + α-Al_2O_3. If there was not complete chemical mixing during the melting process,

small m-ZrO_2 regions could be retained in the melt. If $D_{ave} = 10^{-10}cm^2/sec$ and the sample reached it's melting point in 10 min., then $L \sim 8(Dt)^{1/2} \sim 8$ μm. The initial grain size of the material was >50 μm and it seems posssible that the sample was not totally melted. But (2) cannot explain why there was no m-ZrO_2 found in the MgO-rich eutectic. For this composition, if vaporization occurred on the liquid surface, the relative abundance of MgO would prohibit the nucleation of m-ZrO_2. Thus, it appears that the presence of m-ZrO_2 in the Al_2O_3-rich eutectic is a result of MgO vaporization and subsequent nucleation of ZrO_2 on the surface of the melt during the experiment.

The spinel phase and the c-ZrO_2 phase in both eutectics compete for MgO during the solidification process. In the Al_2O_3-rich eutectic, close to the minimum amount of MgO is dissolved in the spinel and ZrO_2 phases to maintain both structures. In the MgO-rich composition, close to the maximum amount of MgO is dissolved in each phase, with the balance present as pure MgO.

The compositions of the c-ZrO_2 and $Mg_xAl_{2(1-x)}O_{3-2x}$ phases were determined by the lattice parameters calculated from the x-ray diffraction data. The lattice parameters from the four most intense peaks for both the spinel and c-ZrO_2 phases were averaged. For c-ZrO_2, the Aleksandrov et al.(1976) equation, originally developed to calculate the lattice parameter change for Y_2O_3 stabilized c-ZrO_2, was used:

$$a\,(\text{Å}) = \frac{4}{\sqrt{3}}\left[r_{Zr} + r_O + \frac{\sum_k (P_k M_k \Delta r_k)}{100 + \sum_k M_k (P_k - 1)} \right] \qquad (3.0)$$

where a_o = c-ZrO_2 lattice parameter, R_{Zr}, R_O, R_k = ionic radii of zirconium, oxygen and the *kth* stabilizing element, P_k = the amount of ions of each stabilizing element in the oxide molecule, M_k = mol% of stabilizing element and ΔR_k = difference between ionic radii of zirconium and the stabilizing element. As the amount of stabilizing element is increased, the lattice parameter of the ZrO_2 decreases due to the substitution of smaller ions on the Zr sites, according to the reaction shown in Eq. (3.0) for Y_2O_3. The ionic radius of Mg^{2+} in the ZrO_2 lattice was determined to be 0.0648 nm with r_{Zr}=0.0824 nm and r_O=0.14 nm, by using the lattice parameter found in c-ZrO_2 with 10-20 mol% MgO from the data presented

by Sim and Stubican (1987). For MgO, P_k=1 and substituting these values into Eq.(3.0), the lattice parameter as a function of mole fraction (x) in a range of 0-0.3 is:

$$a_o \text{ (nm)} = 0.5136\text{-}0.0407\ x \qquad (3.1)$$

and is shown in Figure 3.1.

The compositions of the spinel phase were determined by the lattice parameters calculated from the x-ray diffraction data. Chiang and Kingery (1988) have recently determined the lattice parameter of magnesium aluminate spinel as a function of Al_2O_3, *f*, in mole fraction to be:

$$a_o \text{ (nm)} = .8334\ \text{-}0.0496f, \qquad (3.2)$$

for Al_2O_3 contents from 0.50-0.85. The data were taken from samples of known composition which were annealed at 1600°C for 0.5 hours and rapidly cooled in air. The decrease of the spinel lattice parameter with increasing Al_2O_3 content is due to the creation of vacancies on the cation sublattice and with the substitution of the smaller Al^{3+} ions to the larger Mg^{2+} ions, expressed by:

$$4Al_2O_3 \xrightarrow{3MgAl_2O_4} > (z+5)Al_{Al} + (3\text{-}z)Al_{Mg}^{\cdot} + (1\text{-}z)V_{Al}^{'''} + (z)V_{Mg}^{''} + 12O_O \qquad ()$$

for $0 \le z \le 1$. For z=0, all of the cation vacancies are on the octahedral sites and for z=1, they are on the tetrahedral sites. The value of z is a sensitive function of processing temperature and cooling rate, since it is a measure of the disorder on the cation sublattice.

The as-quenched x-ray data were evaluated to determine if the calculationed lattice parameters are valid to use in these systems. For the Al_2O_3-rich ternary eutectic, the x-ray data yields a_{spinel}=0.79546 nm and $a_{c\text{-}zirconia}$=0.50839 nm. Inserting these values into Eq (3.2) and (3.1), respectively, the MgO concentration (in mol%) is found to be 22.1% for the spinel phase and 11.6% for the c-ZrO_2 phase. It is assumed that all of the Al_2O_3 is in the spinel due to the absence of any pure Al_2O_3 phase. With the starting composition of 41.2 moles Al_2O_3, it is found that 11.9 moles of MgO is in the spinel phase and 5.3 moles are in the c-ZrO_2 phase, which gives a total of 17.2 moles of MgO present in the as-

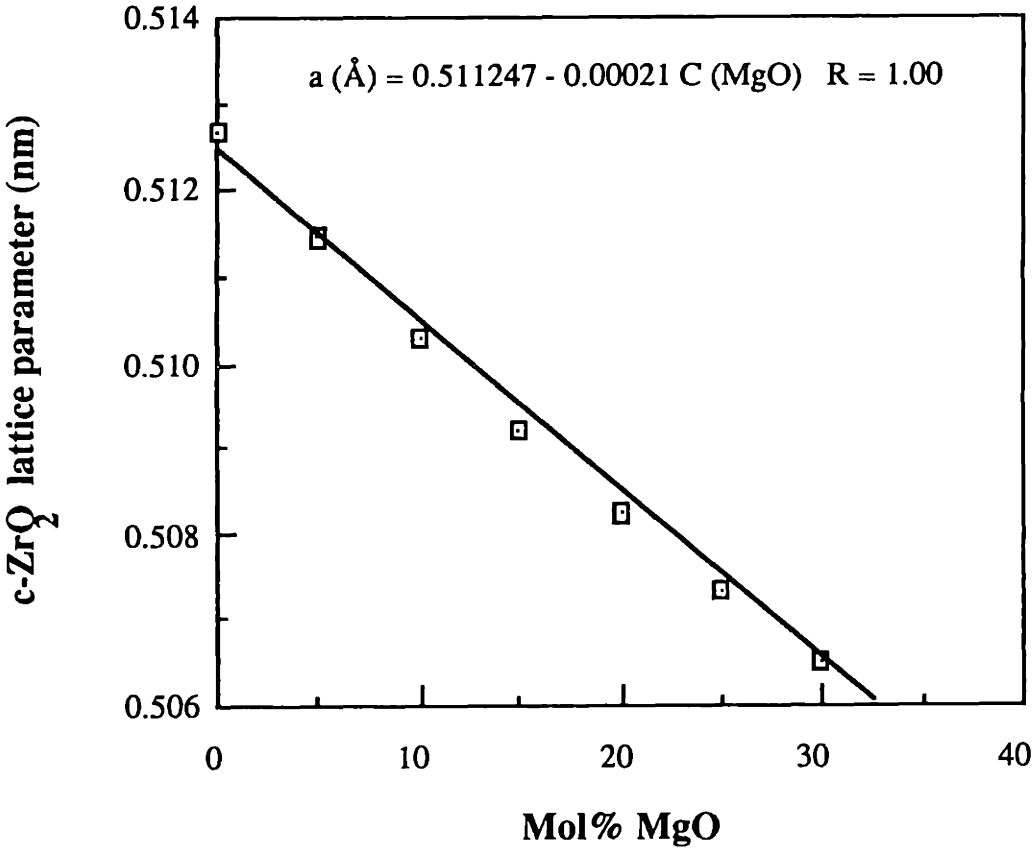

Figure 3.1
Calculated c-ZrO_2 lattice parameter as a function of MgO content.
Used r_{Zr} = 0.082 nm, r_O = 0.14 nm and r_{Mg} = 0.7036 nm in the Aleksandrov (1976) equation.

quenched material. This is in good agreement with the starting composition of 17.4 moles within experimental error. The lattice parameters calculated from the diffraction patterns have a standard deviation error of ~0.0003 nm, which corresponds to an error in the MgO content of ±1.5 mol% in both the c-ZrO_2 and spinel phases. It is likely that some of the MgO vaporized during the melting and solidification experiment, which could also account for the error.

In Chiang and Kingery's work, it is possible there was a depletion of magnesium in the samples, which would shift the stoichiometric spinel lattice parameter to a higher value, but da_o/df should remain the same. In fact, the slope found in this experiment is identical to the one found by Sarjeant and Roy (1967) for splat quenched compositions of magnesium aluminate spinels (see Figure 3.26). This comparison also points to the negligible influence z in Eq. (3.3) has in determining the lattice parameter. Rapidly solidified materials should have a higher degree of cation disorder then in air quenched samples, hence a different da_o/df value. In addition, the lattice parameter measured from a sample cooled from 1600°C is not necessarily the lattice parameter the sample would have after rapid solidification. Thus, the absolute value of what is calculated to be a_o for stoichiometric spinel may be in error, but the change in composition as measured by the lattice parameter is expected to be accurate.

3.2.3 DTA results and density measurements

Figure 3.2(a) shows the DTA results from the Al_2O_3-ZrO_2 eutectic glass. The only peak occurs at 944°C, which is the crystallization temperature for the t-ZrO_2. Figure 3.2(b) shows the DTA results for the Al_2O_3-Y_2O_3-ZrO_2 eutectic glass. The crystallization peak occurs at 932°C, a slightly lower temperature than for the Al_2O_3-ZrO_2 eutectic glass.

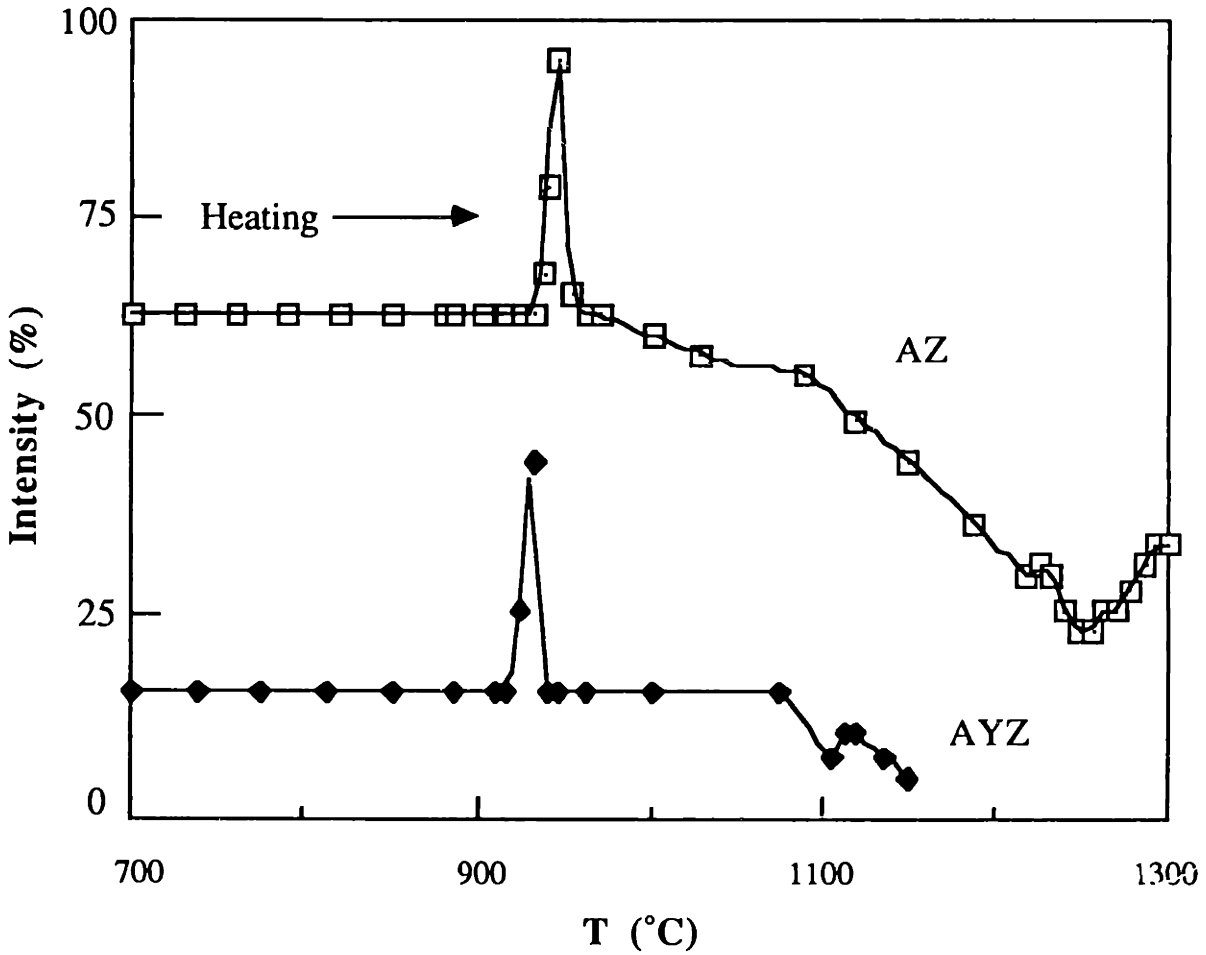

Figure 3.2
DTA results on the Al_2O_3 - ZrO_2 and Al_2O_3-Y_2O_3- ZrO_2 eutectic glasses. Only one peak is observed for each composition which corresponds to the crystallization of a zirconia phase.

Table 3.3 lists the results for density measurements made on the as-quenched, amorphous materials.

Composition (Eutectic)	*Density (gm/cm^3)*	*Density of crystalline material (calculated in gm/cm^3)*	*% Change*
Al_2O_3-ZrO_2	4.48	4.65	-3.8
Al_2O_3-Y_2O_3-ZrO_2	4.24	4.57	-7.8
Al_2O_3-MgO-ZrO_2 (high Al_2O_3)	4.76	5.16*	-8.4
Al_2O_3-MgO-ZrO_2 (high MgO)	4.61	5.23*	-13.45

Table 3.3 Results for density measurements on the amorphoustwin rolled flakes for the binary and three ternary eutectics.
* These densities were calculated by using the densities of the rapidly solidified crystalline materials as outlined in Appendix I.

The density of the amorphous rapidly solidified compositions is smaller than their crystalline counterparts. A glass is typically up to 12% less dense than its crystalline analogue and all of the compositions fall roughly within this range. The larger decrease for the Al_2O_3-Y_2O_3-ZrO_2 composition over that of the Al_2O_3-ZrO_2 eutectic is most likely due to the lower viscosity of the melt. The Stokes-Einstein equation for viscosity, η is:

$$\eta = \frac{kT}{3\pi\lambda D} \qquad (3.4)$$

where λ is the jump distance for atom mobility and D is the diffusion coefficient. D and λ are expected to be larger for the Al_2O_3-Y_2O_3-ZrO_2 glasses. This is in agreement with the predictions made from solidification theory. Under identical solidification conditions, the Al_2O_3-Y_2O_3-ZrO_2 eutectic should be an easier glass former than the Al_2O_3-ZrO_2 eutectic, based on the interlamallar spacings measured from unidirectional solidification studies.

The densities of the Al_2O_3-MgO-ZrO_2 ternary eutectics were calculated by summing the volume fraction multiplied by the density of each phase. For the Al_2O_3-rich eutectic, there is only a two phase assemblege of an Al_2O_3-rich spinel+c-ZrO_2 in the as-quenched crystalline material. For the MgO-rich eutectic, there is a three phase assemblegde of spinel+c-ZrO_2 +MgO. Appendix I outlines how these calculations were made. For the Al_2O_3-rich eutectic, the density is found to be:a function of x, the mole fraction of MgO in the spinel phase:

$$\rho_{Al\text{-}rich} = 5.3636 - 1.2118x + 2.7062x^2 - 6.2148x^3 \quad R=1.00 \qquad (3.5)$$

The density of the MgO-rich eutectic was found to be a function of x as well as the mole fraction of MgO in the material, C_M:

$$\rho_{Mg\text{-}rich} = 4.6433 + 0.9017x + 1.7065x^2 - 1.9495x^3 \quad R=0.99,\ C_M = 0.17 \qquad (3.6)$$

Eqs. (3.5) and (3.6) are plotted in Figure 3.3. As shown, the density of the Al_2O_3-rich eutectic decreases and the density of the MgO-rich eutectic increases with increasing MgO content in the spinel. For the Al_2O_3-rich composition, as the mole fraction of MgO increases in the spinel phase, depleting its concentration in the c-ZrO_2 phase, its density increases. For the MgO-rich composition, as the mole fraction of MgO increases in the spinel phase, the amount of pure MgO decreases, its density increases.

The densities of the Al_2O_3-MgO-ZrO_2 ternary eutectics glasses are smaller than the crystalline densities calculated by the above method.

3.2.4 Microstructural Analysis

Figure 3.4 shows a high resolution TEM micrograph of the amorphous rapidly solidified Al_2O_3-ZrO_2 material. The typical salt-and-pepper structure of a glass is seen along with the amorphous diffraction pattern. Figure 3.5 shows a TEM micrograph of the as-quenched Al_2O_3-ZrO_2 material produced by the melt extraction technique which shows an amorphous region with a lamellar eutectic crystalline area. In this micrograph, it is seen that there are two different solidification fronts which appear to have occured due to the presence of two cooling mechanisms. The interlamellar spacing is too coarse for the

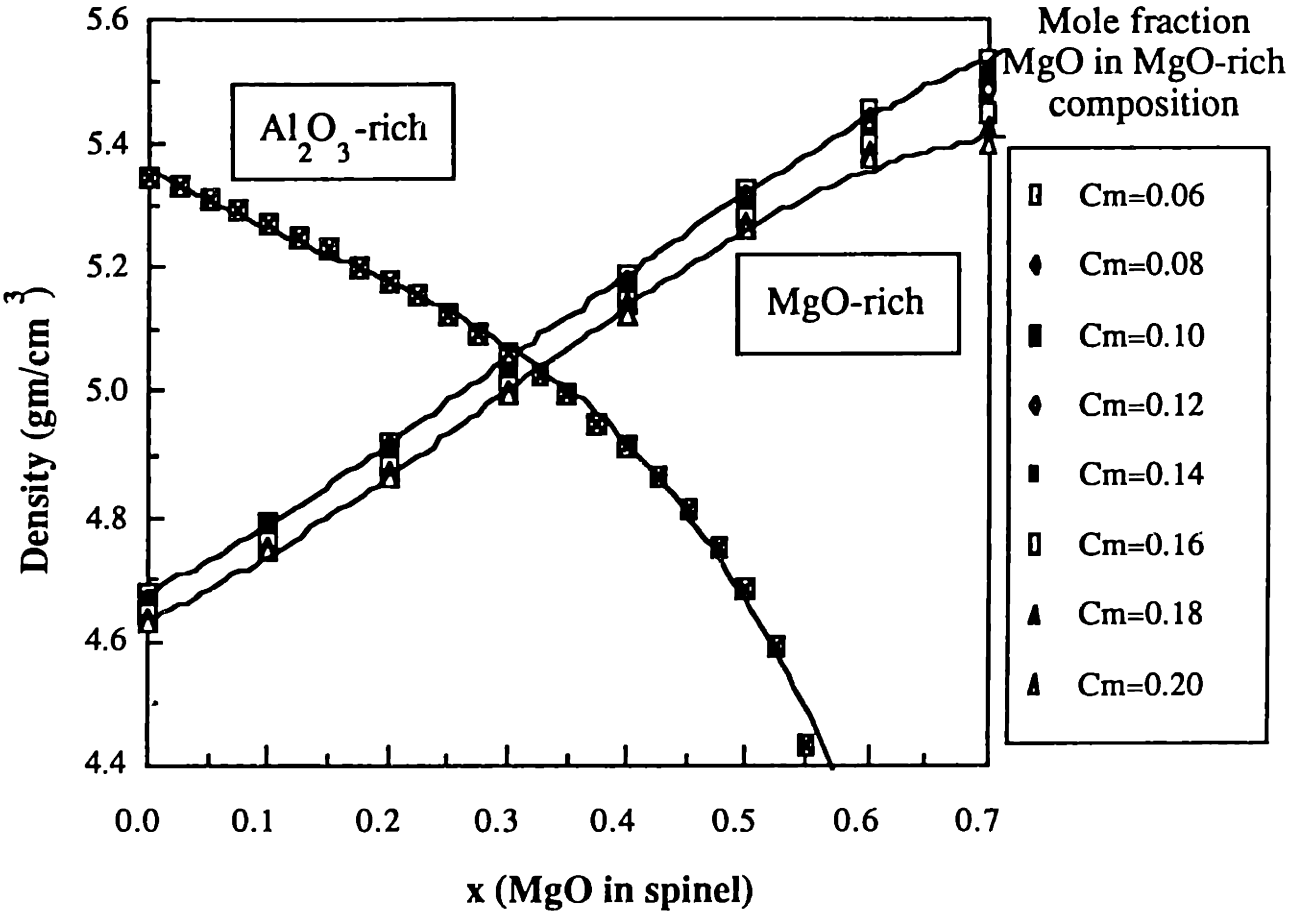

Figure 3.3

Density of the Al_2O_3 -rich and MgO-rich ternary eutectics as a function of MgO content in the spinel phase. The Al_2O_3 -rich eutectic consists of spinel+c-ZrO_2. The MgO-rich composition consists of spinel+c-ZrO_2 +MgO.

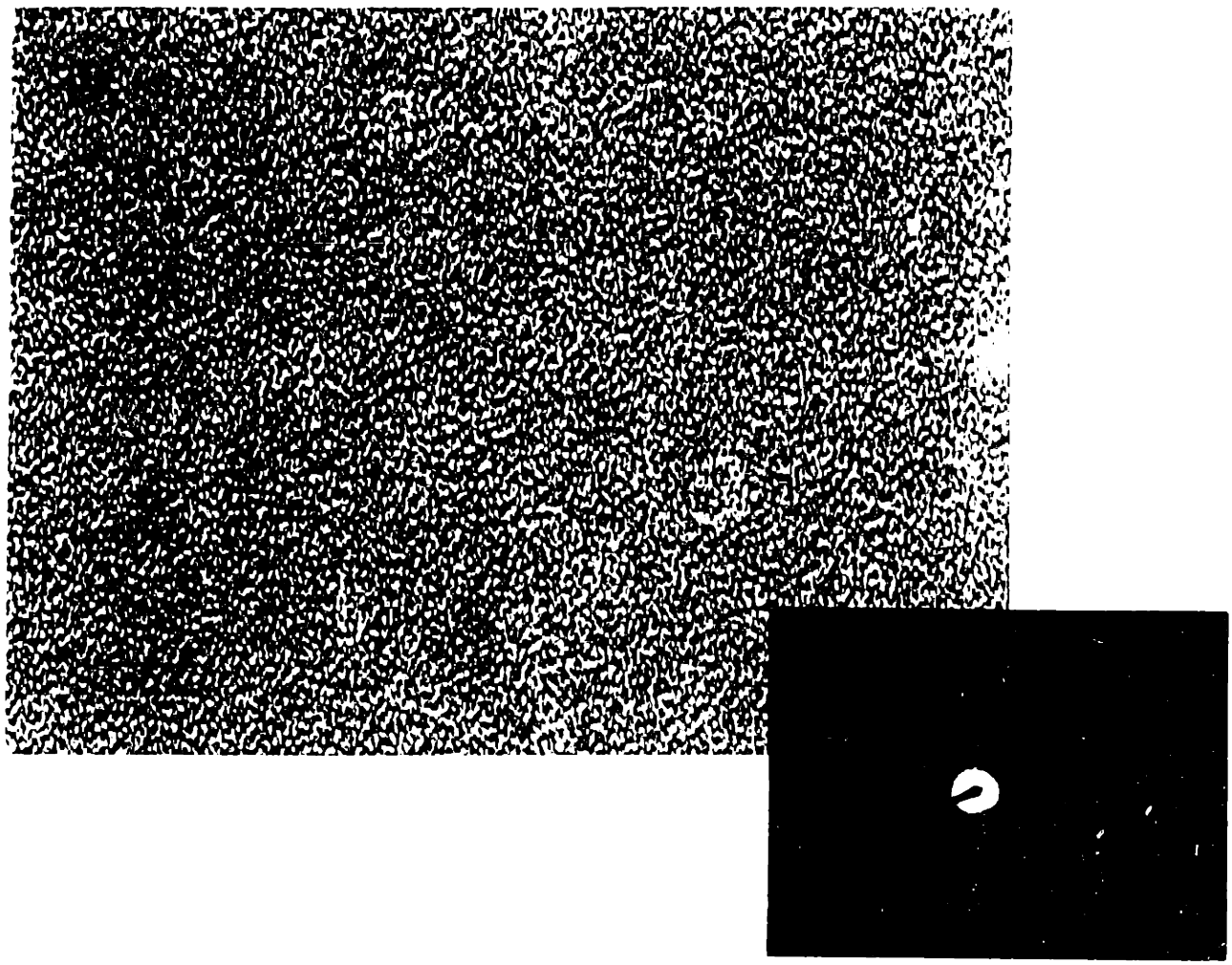

Figure 3.4
High resolution TEM micrograph of amorphous Al_2O_3-ZrO_2 produced by the twin rolling technique.

0.1 μm

Figure 3.5

TEM micrograph of the as-quenched Al_2O_3-ZrO_2 eutectic composition showing an amorphous and crystalline regions in samples generated from the melt extraction technique. Radial growth of the crystalline region occured from surface cooling.

scenario of the solidification front travelling fast enough to produce a glass and then slowing down enough to produce crystalline materials. Furthermore, the crystalline microstructure clearly shows a radial growth with a positive curvature into the glass. The most probable explanation of this is that there was cooling from the air on the top surface of the melt as well as from the single roller. The air cooling caused nucleation and growth of the crystalline phase whereas the roller quenched the melt quickly enough to form a glass. Single substrate quenching methods do not seem to be optimal for quenching these oxides with the intent of forming totally amorphous materials.

The crystalline microstructures from the three Al_2O_3-ZrO_2 compositions show a variation of growth morphologies. The wide variation of eutectic spacings found in the eutectic indicate that there was a spectrum of cooling rates in the materials. When the droplet hits the platens, it solidifies at a fast rate and the remaining liquid is sheared over the solidified part and cools at a slower rate. There is also evidence that the liquid had partially crystallized before the platens closed on it. When this occurs, the temperature gradient in the liquid is negative due to the release of the latent heat of fusion. This can lead to the formation of dendrites even at the eutectic composition. Figure 3.6 shows a TEM micrograph of the eutectic composition with α-Al_2O_3 dendrites surrounded by the eutectic microstructure However, in the laser-splatting technique, the heat is primarily withdrawn through the platens and growth occcurs perpendicular to them and the temperature gradient in the liquid is positive.

Minford et al. (1979) have found a relationship in binary eutectic compositions between the volume fraction of the minor phase and the surface energy per volume which predicts fibrous growth for volume fractions < 0.28 and lamellar growth for higher values. Hunt and Jackson (1966) examined binary eutectic solidification in terms of the minimum undercooling required for each phase and have predicted fibrous growth for volume fractions up to 32%. For the Al_2O_3-ZrO_2 eutectic, the volume fraction of ZrO_2 minor phase is 0.34 [Schmid and Viechnicki (1970)], which falls in the lamellar regime but lies close to the boundary between rod and lamellar growth. Thus, small changes in the undercooling or solidification rate can yield fibrous growth. In unidirectional solidification studies, Schmid and Viechnicki (1970) found fibrous growth for growth velocities between 1.3-15.6 cm/hr and Cocks et al. (1973) found lamellar growth between 1.4-50.8 cm/hr.

Both fibrous and lamellar growth are found in this system. Figure 3.7(a) shows the fibrous microstructure and 3.7(b) shows the lamellar structure.microstructures. These microstructures were taken from the samples which were solidified with the laser splatter.

Figure 3.6
TEM micrograph of the as-quenched Al_2O_3-ZrO_2 eutectic produced through the laser splatting technique. α-Al_2O_3 dendrites are surrounded by a lamellar eutectic microsturcture. The solidification front in this micrograph has moved from a coupled zone into a dendritic growth zone.

(a)

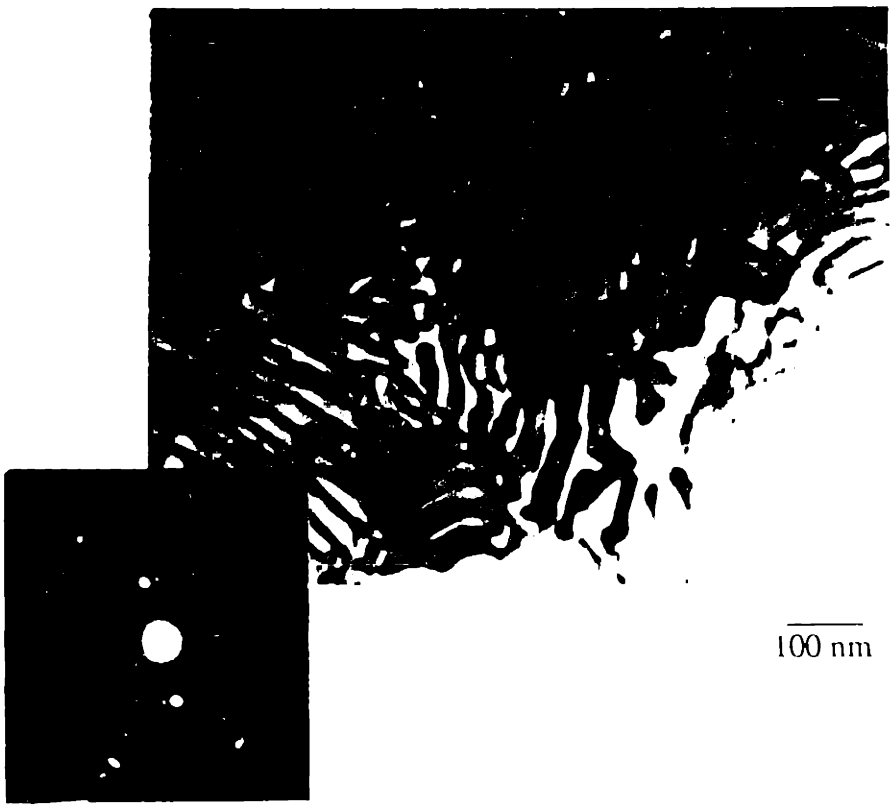

(b)

Figure 3.7
TEM micrograph of (a) lamellar eutectic growth and (b) fibrous (rod-type) growth in the Al_2O_3-ZrO_2 composition produced by laser splatting.

Figure 3.8
TEM micrograph of the as-quenched Al_2O_3-ZrO_2 eutectic composition produced by the melt extraction technique. Note δ-Al_2O_3 dendrites perpendicular to the solidification front (out of the page). Dendrites are surrounded by rod-type eutectic microstructure.

The amount of undercooling and the solidification rate must be different in these two regions. These microstructures are regular eutectics, they do not display faceting of either phase which indicates that both phases have a low entropy of fusion ($\Delta S_f/R<2$).

Another eutectic microstructure is shown in Figure 3.8 as produced by the melt extraction technique. Shown here are δ-Al_2O_3 dendrites surrounded by a degenerate eutectic microstructure. In this case the same phenomena is found as described for the laser-splat material. The fastest cooled material is generated next to the roller but the surface cooling is also present, and resulted in the formation of two solidification fronts which are perpindicular to each other. The liquid on the surface is sufficiently undercooled to nucleate dendrites which grow perpendicular to the solidification front on the roller. It originally seemed possible to explain this phenomenon in terms of a change in solidification front velocity. A change in velocity could move the growth from a coupled zone to a dendritic zone, as shown in Figure 1.8(c). But this is unlikely due to the orientation of the δ-Al_2O_3 dendrites. For a zone change, the dendrites should be parallel to the solidification front.

Figure 3.9 shows the hypoeutectic composition produced through laser splatting. Dendritic growth of the primary α-Al_2O_3 phase is seen surrounded by the eutectic microstructure composed of t-ZrO_2 and α-Al_2O_3. These materials have been formed at moderate solidification rates. Figure 1.8 predicts that at high solidification rates, the primary dendrites should be surrounded by a glass of the eutectic composition. This microstructure was not observed for this composition. Figure 3.10 shows the microstructure of a twin rolled sample of the hypereutectic. In this case, the primary dendrites are t-ZrO_2 which are embedded in a glass. In this case, the solidification velocity was high enough for the eutectic to form a glass.

Plasma sprayed samples were smaller in diameter and thicker than the laser splats, melt extrasion or twin rolled flakes. They were also stuck to the glass slide on which the material was sprayed. These factors made the samples harder to prepare for TEM analysis. One sample was examined and was found to be amouphous, but no further analysis was performed. The solar splat material was all crystalline. Only a few samples were examined and were found to consist of a uniform microstructure. No further analysis was performed on them.

The samples milled on the cold stage in the ion mill showed no difference in microstructure with samples milled on the standard stage. The temperature can reach as

Figure 3.9
TEM micrograph of the as-quenched hypoeutectic Al_2O_3-ZrO_2 composition produced by laser splatting. α-Al_2O_3 dendrites are surrounded by the eutectic microstructure.

Figure 3.10
TEM micrograph of the as-quenched hypereutectic Al_2O_3-ZrO_2 composition produced by the twin rolling device. t-ZrO_2 (dark phase) dendrites are surrounded by a glass.

high as 200°C in samples milled with no cooling. No low temperature transformations were identified by the DTA except release of hydroxyl groups.

3.2.5 Spectroscopy

IR Spectroscopy

Figure 3.11 shows the IR results for the Al_2O_3-ZrO_2, Al_2O_3-Y_2O_3-ZrO_2 and MgO-rich Al_2O_3-MgO-ZrO_2 glasses. The Al_2O_3-rich composition was not examined due to the small sample size. For transmission of 10%, the IR transparency is extended out to 1000 cm^{-1} for Al_2O_3-ZrO_2 glasses and 950 cm^{-1} for Al_2O_3-Y_2O_3-ZrO_2 glasses for samples ~50 μm thick. The close values reflect the fundamental adsorption of the Al-O vibrational bond, which occurs between 900-1100 cm^{-1}, is the dominant adsorption mechanism. The zirconium and yttrium additions to the Al_2O_3 glass appear to have no affect on shifting the adsorption edge, which indicates that these cations act as intermediates in the glass, not as network formers or modifiers. Other evidence for Y_2O_3 acting as an intermediate is found from solidification theory. As pointed out in Sec. 1.6.1, under identical solidification conditions, the Al_2O_3-Y_2O_3-ZrO_2 eutectic should be an easier glass former than the Al_2O_3-ZrO_2 eutectic. This indicates that the melt viscosity of the Al_2O_3-Y_2O_3-ZrO_2 is lower which implies that the Y_2O_3 does not act as a modifier, which would decrease the viscosity, but instead is incorporated as an intermediate.

The Al_2O_3-MgO-ZrO_2 adsorption edge occurs at 900 cm^{-1}. Again, the dominant adsorption mechanism is the Al-O bond even though this composition has only 17 mol% Al_2O_3. This indicates that the Al_2O_3 and MgO are both network formers.

Significant scattering by second phase particles is unlikely in these samples. The glasses were visibly transparent and if there is some crystallinity, the particle size is <~0.5 μm. The adsorption edges occur at much higher values.

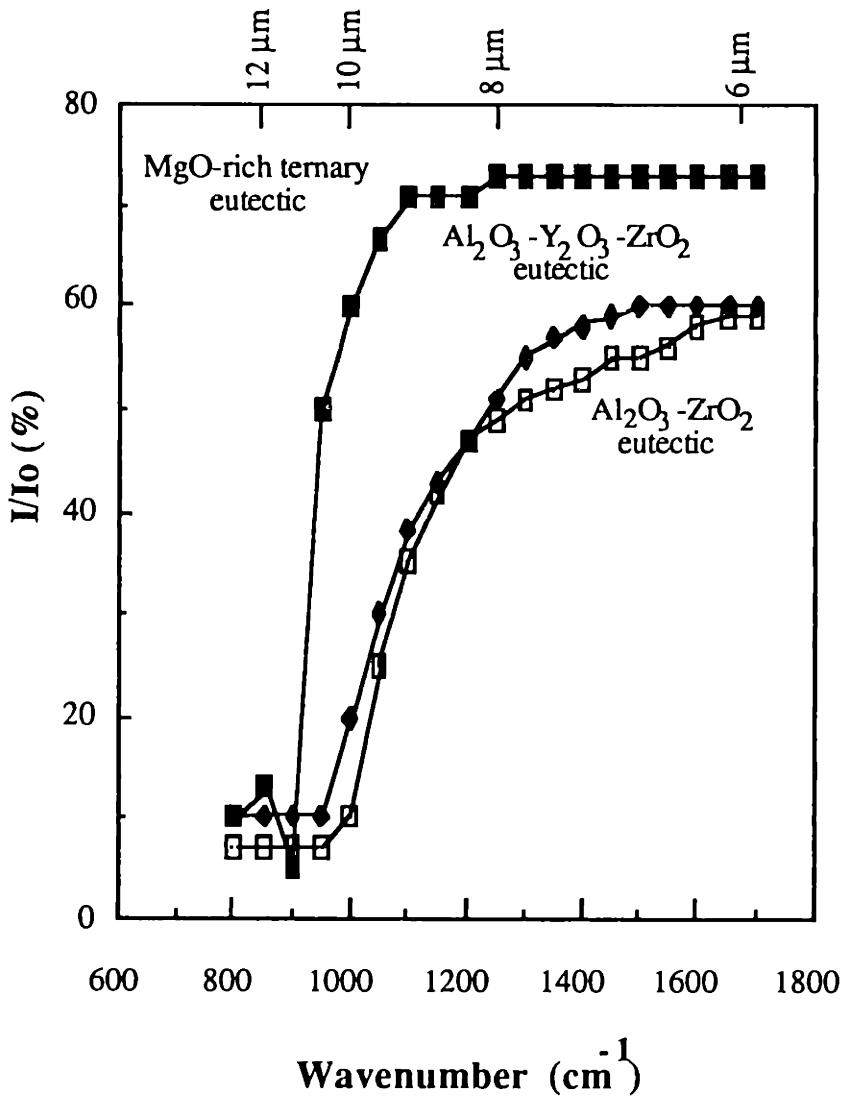

Figure 3.11

Normalized transmitted intensity as a function of wavenumber and wavelength for the amorphous samples in the IR range.

VUV Spectroscopy

The VUV results are shown in Figure 3.12 which shows the transmission as a function of wavelength. The Al_2O_3-Y_2O_3-ZrO_2 glass has the highest adsorption edge at which there is 10% transmission of the initial intensity (5.52 eV), followed closely by Al_2O_3-ZrO_2 glasses (5.4 eV) and the MgO-rich Al_2O_3-MgO-ZrO_2 eutectic glass (5.17 eV) with the lowest value. The band gaps for the pure, crystalline oxides are shown in Figure 3.13, along with the band gaps measured for the eutectic glasses. The band gaps for the Al_2O_3, and MgO are high and do not contribute to the electronic excitation at the adsorption edge. The band gaps for crystalline Y_2O_3 and ZrO_2 are 5.6 and 4.99 eV, respectively, and the glasses fall within this range. Thus, the UV adsorption arises from an electronic charge transfer in the ZrO_2 for the Al_2O_3-ZrO_2 and Al_2O_3-MgO-ZrO_2 eutectic glasses and not from an exciton. The slightly higher value for the Al_2O_3-Y_2O_3-ZrO_2 glass is possibly due to a charge transfer excitation in the Y_2O_3. The shapes of the curves are slightly different and is most likely due to increased Rayleigh scattering in the glass from small crystallites. In addition, the atomic fraction of ZrO_2 is different for each composition, and this will affect the shape of the adsorption edge.

3.2.6 Estimates of Cooling Rates

There are several techniques available to estimate the cooling rates for the substrate quenched materials. Figure 3.14 shows the geometrical outline for an estimate of the cooling rate as a function of solidified material thickness for the twin roller system using a relationship modified from the derivation of Chen and Miller (1970). The velocity of the liquid-solid solidification front is taken to be equivalent to the roller speed. Assuming that the liquid impinges between the rollers and solidifies at their contact point forcing the rollers to move apart the thickness of the liquid stream and that the liquid is at its melting temperature at the contact point, the cooling rate can be written as:

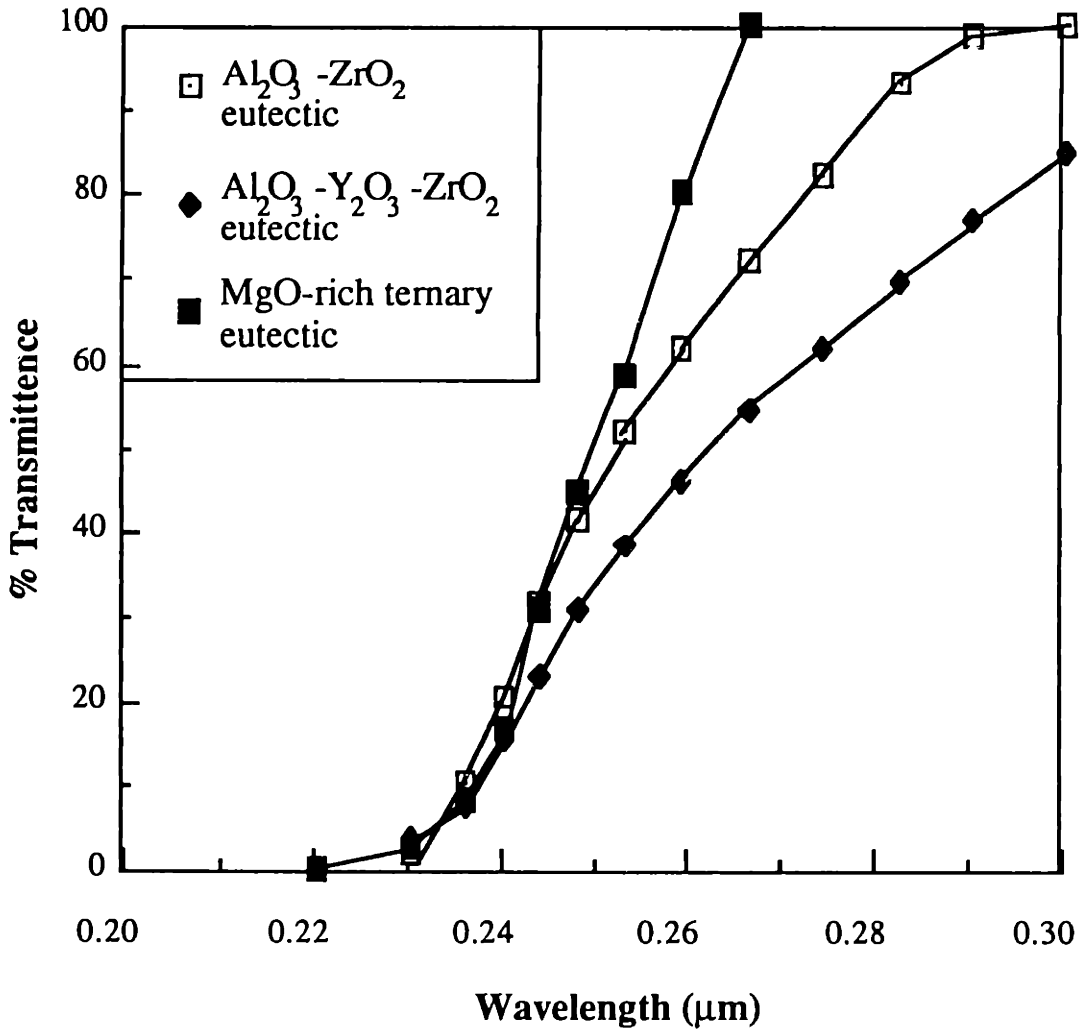

Figure 3.12

% Transmittence as a function of wavelength for amorphous samples in the UV range.

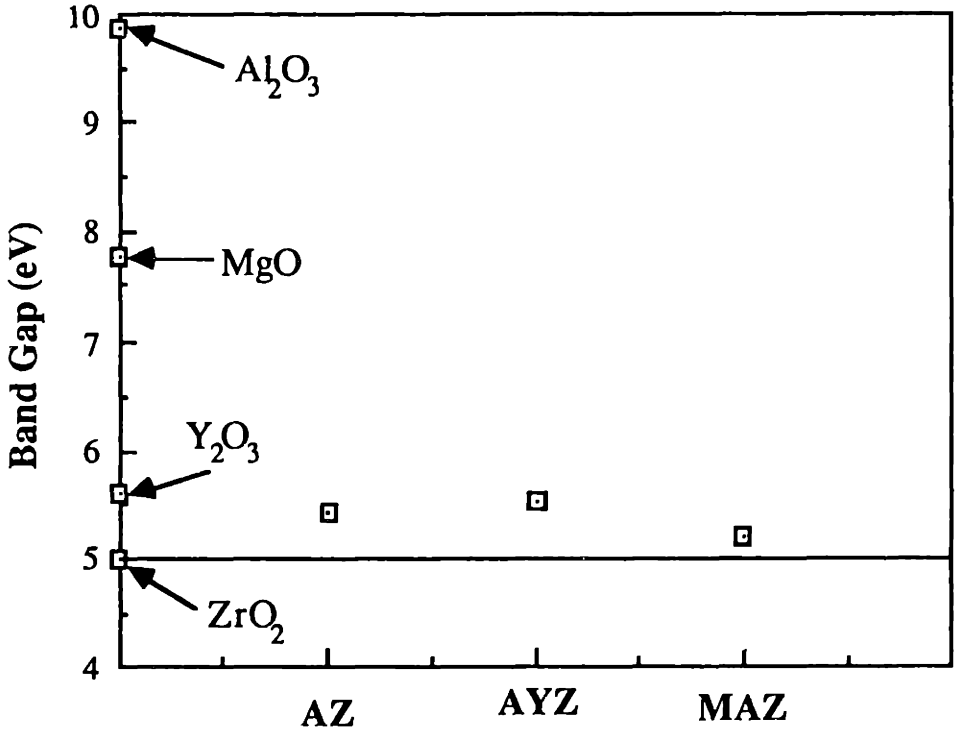

Figure 3.13

VUV spectroscopy results showing optical band gap for Al_2O_3 -ZrO_2, Al_2O_3 -Y_2O_3 -ZrO_2, and the MgO-rich MgO-Al_2O_3 -ZrO_2 eutectic glasses. Band gaps for the pure crystalline oxides are shown for comparison.

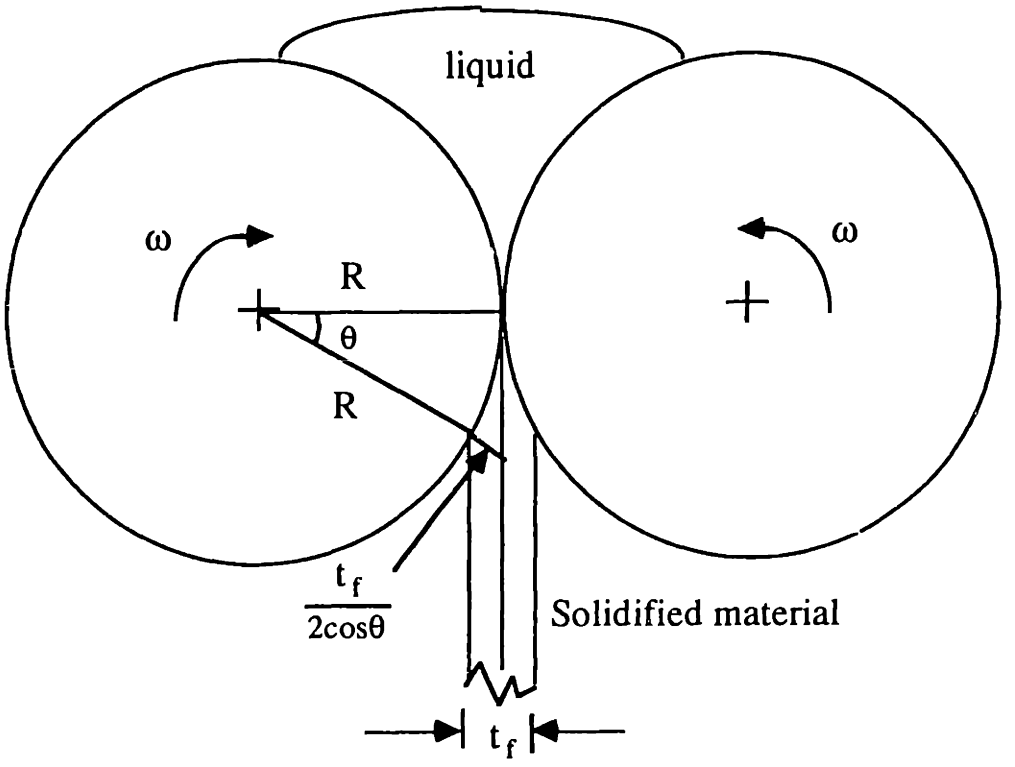

$$\frac{dT}{dt} = \frac{dT}{d\theta} \cdot \frac{d\theta}{dt} \qquad \cos\theta = 1 - \frac{t_f}{2R}$$

$$\dot{T} = \frac{\Delta T}{\Delta\theta}\,\omega \qquad \Delta T = T_m - T_f$$

$$\frac{dT}{dt} = \frac{(T_m - T_f)\,\omega}{\arccos\left[1 - \frac{t_f}{2R}\right]}$$

R=radius of the wheel
T_m= melting point
T_f = exit temperature
ω=wheel speed in rad/sec

Figure 3.14
Cooling rate estimation from geometrical parameters
in the twin rolling system.

$$\frac{dT}{dt} = \frac{\Delta T}{\left\{ \frac{\text{Arccos}\left[\frac{R - \frac{1}{2} t_f}{R} \right]}{\omega} \right\}} \qquad (3.7)$$

where ΔT is the difference between the liquid temperature and the temperature of the solidified material as it leaves the rollers, R is the radii of the wheels, t_f is the thickness of the solidified product, and ω is the wheel speed. Figure 3.15 shows the results for the cooling rate for the various thicknesses of flakes obtained with different wheel speeds. For the Al_2O_3-ZrO_2 eutectic, with a wheel speed of 6000 rpm, a flake thickness of 50 μm, and assuming that the solidified materials is approximately 250°C at the exit point which gives a cooling rate of ~3 x10^7 K/sec.

In another approach, Revcolevschi (1976) has estimated the cooling rate for splat quenched materials to be for ideal cooling:

$$\frac{dT}{dt} = \frac{L_F R}{c_p \lambda} \qquad (3.8)$$

Where L_F is the latent heat of fusion, R is the growth rate, c_P is the specific heat and λ is the interlamellar spacing. Using L_F and c_P for Al_2O_3 to be 26 kcal/mol and 32.65 cal/(mol K), and for ZrO_2 to be 20 kcal/mole and 17.8 cal/(mol K) and applying the rule of mixtures, a composite value of 24.01 kcal/mol and 27.01 cal/(mol K) for L_F and c_P is obtained. Using the values obtained from Eq (3.7) with R = 10 cm/sec and the smallest interlammelar spacing observed λ = 10 nm, the cooling rate is found to be 9.2x10^6 K/sec. This value represents the maximum cooling rate for the generation of crystalline materials. Higher cooling rates would lead to glass formation.

The two estimates reveal that the highest cooling rate for the twin roller quenched materials is ~10^7 K/sec, which agrees with other estimates found for attaining glass formation in rapidly solidifying refractory oxides. Since these two cooling rate estimates are similar, it appears that the rate limiting process is the heat extraction from the sample (ideal cooling) and not from interfacial thermal resistance between the rollers and the splat

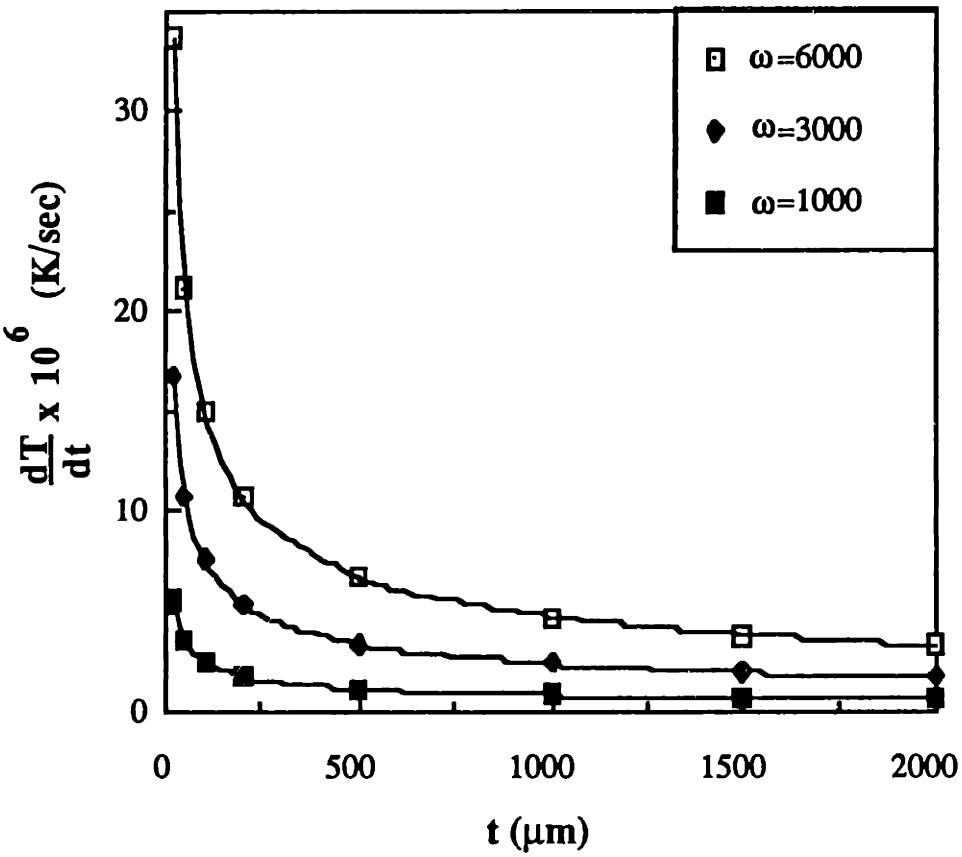

Figure 3.15

Cooling rate as a function of thickness of the solidified material for different wheel speeds for the twin roller system.

(Newtonian cooling). If Newtonian cooling was rate limiting, much smaller cooling rates would be calculated, as pointed out in Sec. 1.4.

3.3 Heat Treated Samples

The Al_2O_3-ZrO_2 and Al_2O_3-Y_2O_3-ZrO_2 eutectic glasses were heat treated in a furnace and with the hot stage in the TEM. The Al_2O_3-MgO-ZrO_2 ternary eutectics were heat treated only in a furnace.

3.3.1 Al_2O_3-ZrO_2 and Al_2O_3-Y_2O_3-ZrO_2 Eutectics

X-ray Diffraction

Table 3.4 lists the x-ray diffraction results for the heat treated Al_2O_3-ZrO_2 eutectic glasses. For the t-ZrO_2 phase, there was no detectable change in lattice parameter for all of the heat treatments.

Heat Treatment Conditions	*Phases Present*
800°C/all times	Amorphous
950°C/45 min. 1200°C/5 min.	t-ZrO_2 only
1000°C/15-105 min. 1200°C/45-105 min.	t-ZrO_2 with δ-Al_2O_3
1000°C/20 hours	t-ZrO_2 with δ+α-Al_2O_3
1450°C/2-45 min.	t+m-ZrO_2 with α-Al_2O_3

Table 3.4 X-ray diffraction data for the heat treated Al_2O_3-ZrO_2 eutectic glass.

As seen in the above table, the amorphous material was stable until 950°C was reached. At this temperature, devitrification of the glass occured by the nucleation of t-ZrO_2 but not of any Al_2O_3 phase. This is corroberated by the DTA results shown in Figure 3.2. At 1000°C, the presence of δ-Al_2O_3 is seen along with the t-ZrO_2. The δ-Al_2O_3 polymorph is tetragonal with a triple spinel block along the c-axis. The occurance of other polymorphs of Al_2O_3 for small grain sizes has been reported by numerous other workers. At higher temperature heat treatments, the transformation of δ-Al_2O_3 to α-Al_2O_3 occurs. Only at the highest heat treatments do the t-ZrO_2 grains grow sufficiently large to transform to m-ZrO_2 upon cooling.

Hot Stage TEM

A series of TEM micrographs are shown in Figure for the Al_2O_3-ZrO_2 eutectic glass. In Figure 3.16(a), the sample is shown after heating to 1148°C for 30 minutes. The microstructure consists of small t-ZrO_2 crystallites embedded in a glass. The crystallites are ~2 nm in diameter. Smaller crystallites were not observed. The nucleation is homogeneous; the particles are evenly and randomly distributed in the glassy matrix. Further development of the microstructure is shown in Figure 3.16(b) at 1194°C for 5 minutes. The crystallites have grown to 5 nm and amorphous material is still present. Figure 3.16(c) shows the microstructure at 1194°C after 30 minutes. t-ZrO_2 crystallites are seen of size 10 nm. Due to the decrease in density, holes have developed in the sample. Higher temperatures produced the nucleation of the δ-Al_2O_3 phase, as shown in Figure 3.16(d). The microstructure is very uniform with an average grain size of ~50 nm. Figure 3.16(e) shows the microstructure after a heat treatment at 1450°C. The sample consists of small t-ZrO_2 and larger m-ZrO_2 grains surrounded by an α-Al_2O_3 matrix. The m-ZrO_2 is clearly distinguished by the presence of twins.

Figure 3.17 shows the hot stage TEM micrographs of the Al_2O_3-Y_2O_3-ZrO_2 eutectic. Figure 3.17(a) shows the sample in the as-quenched consition. The material is amorphous with a featurless bright field micrograph and amorphous ring diffraction pattern. Figure 3.17(b) shows the sample after heating for 5 minutes at 1100°C. C-ZrO_2 has homogeneously nucleated in the glass. The crystallite size is ~5 nm. Figure 3.17(c) shows the microstructure after an anneal at 1150°C for 15 minutes. The c-ZrO_2 crystallites are ~10 nm and δ-Al_2O_3 is present.

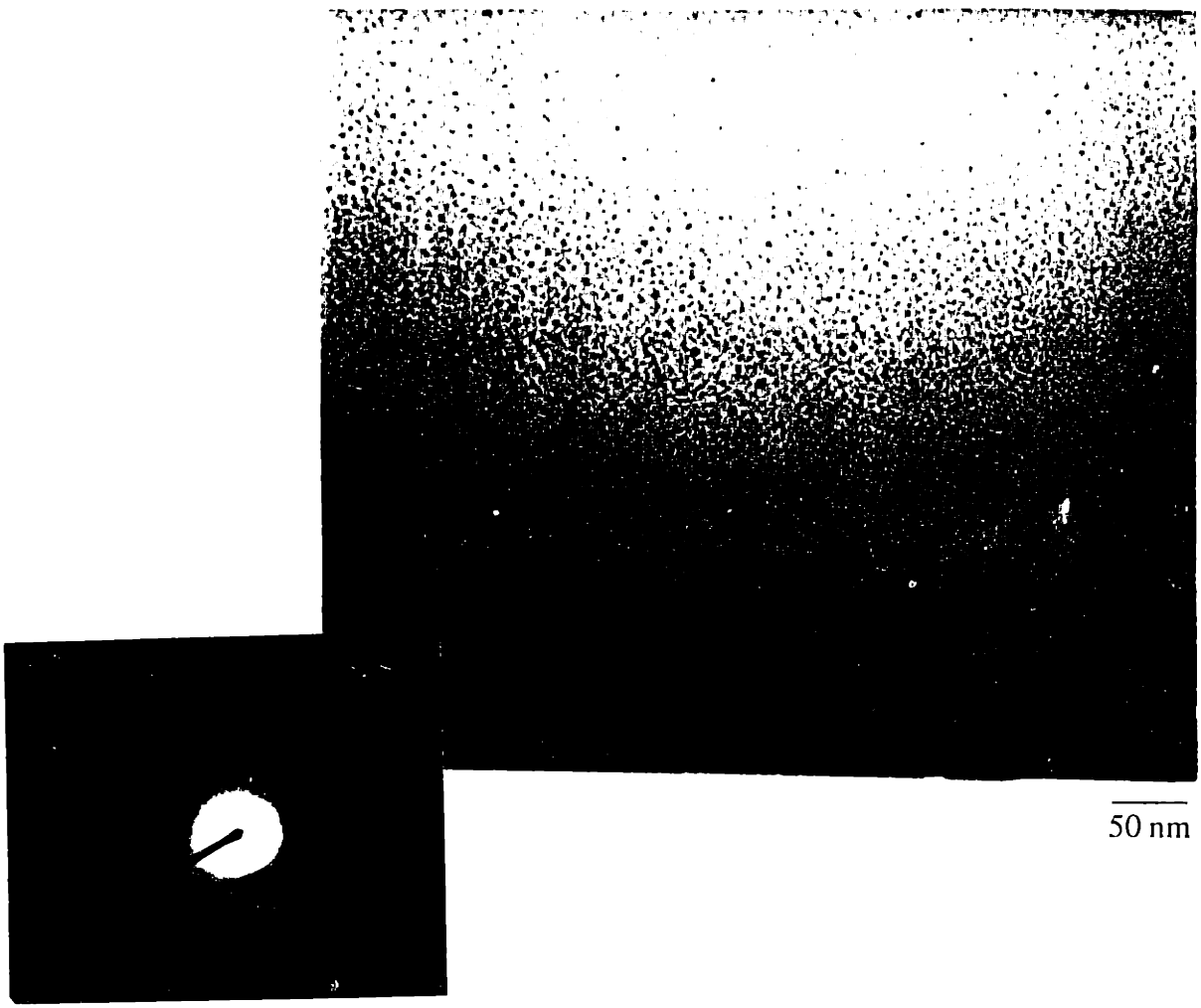

Figure 3.16
Hot stage TEM bright field micrographs and diffraction patterns for the Al_2O-ZrO_2 eutectic glass. (a) 1148°C, 30 minutes, t-ZrO_2 crystallites (~2 nm) are embedded in a glass.

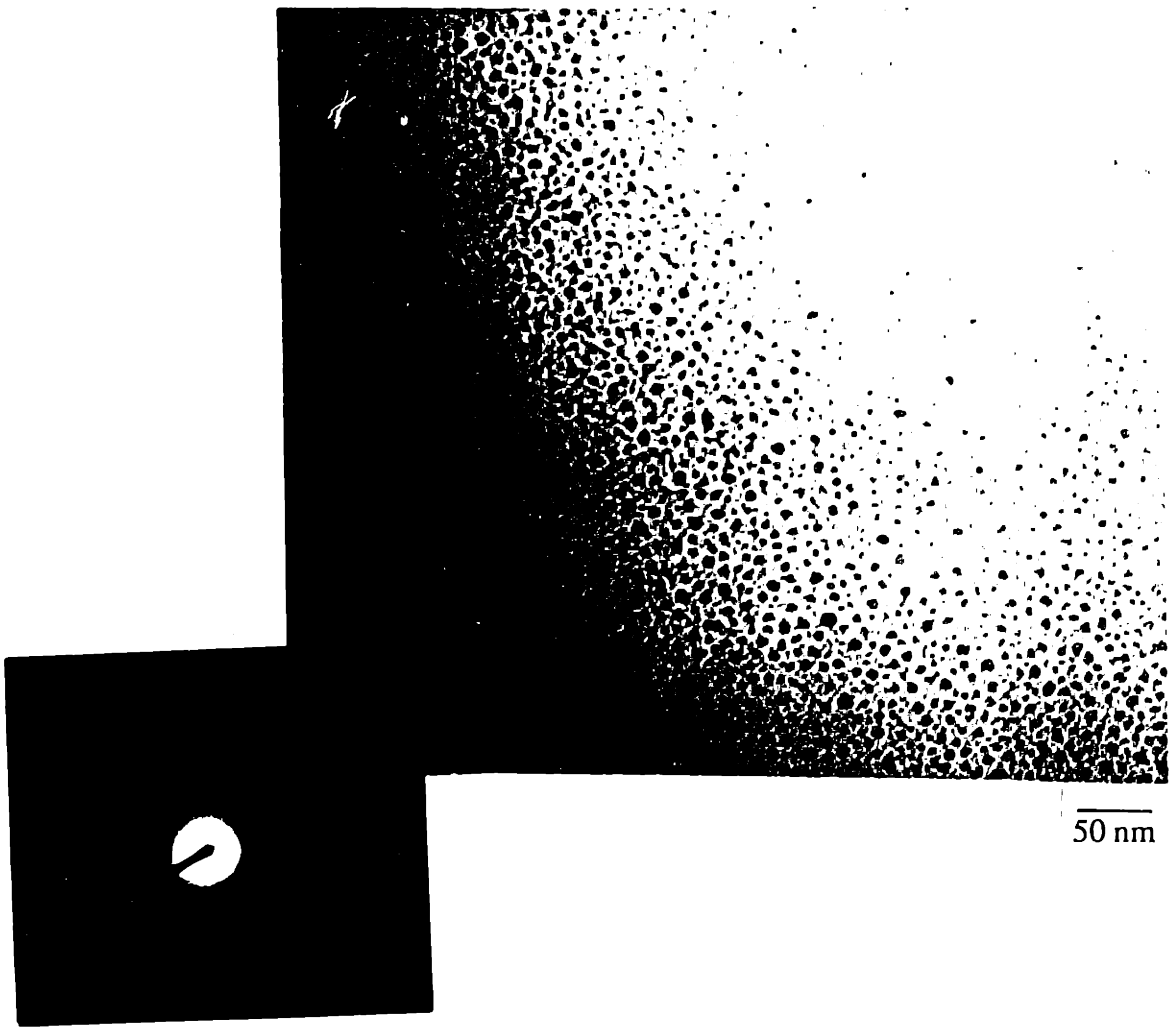

Figure 3.16(b)
At 1194°C, 5 minutes. The t-ZrO_2 has grown to ~5 nm, but a faint amorphous ring is still present.

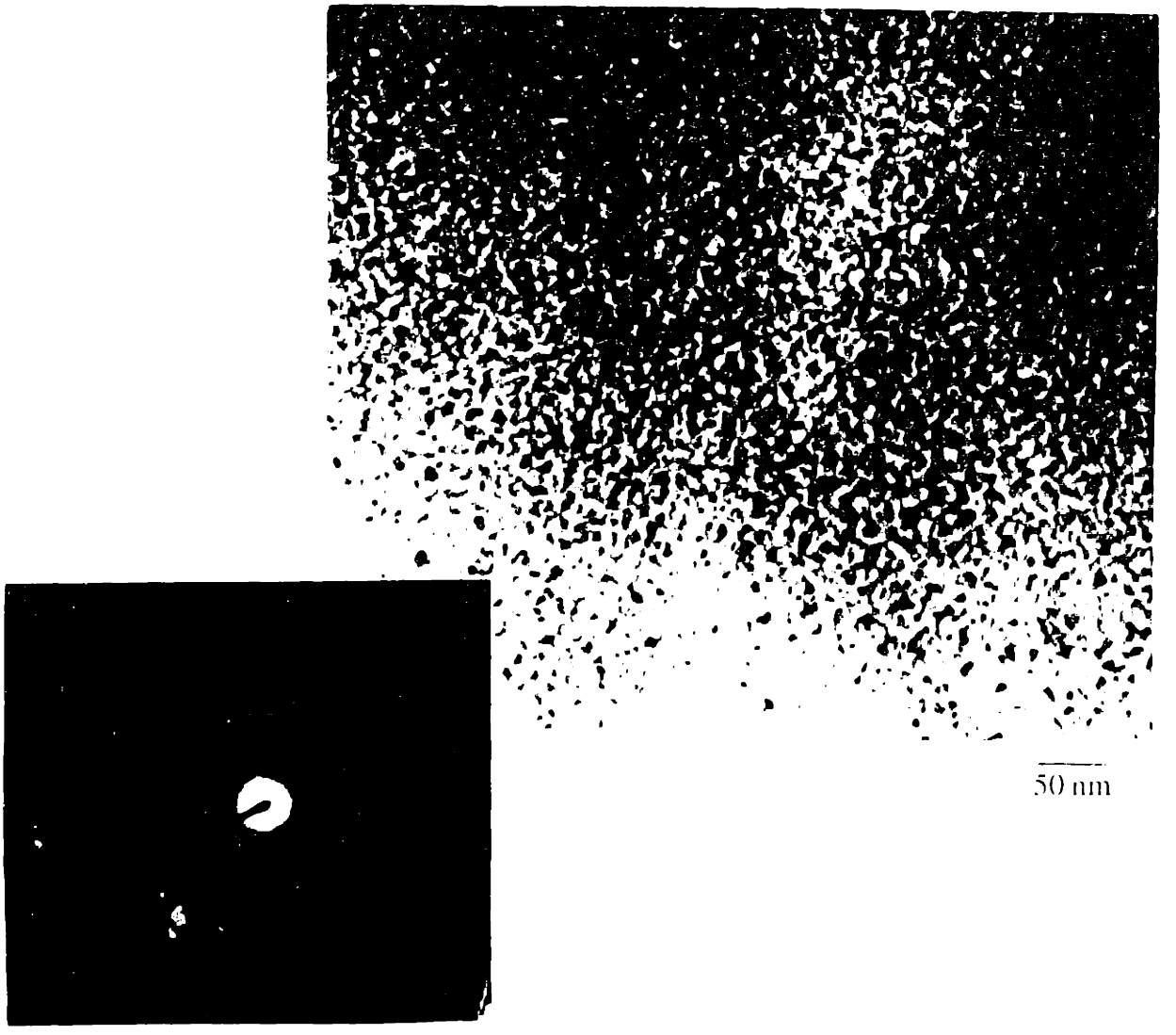

3.16(c) At 1194 C, 30 minutes. The t-ZrO_2 crystallites have grown to ~7 nm. No amorphous material is present, the diffraction pattern shows only well defined, sharp rings..

(d)

(e)

Figure 3.16 (d) at 1200°C, 30 minutes. t-ZrO_2 with δAl_2O_3. (e) 1450°C, 1 hour. Microstructure consists of α-Al_2O_3 and t+m-ZrO_2. m-ZrO_2 is clearly identified by the twinned structure. t-ZrO_2 particles are featureless.

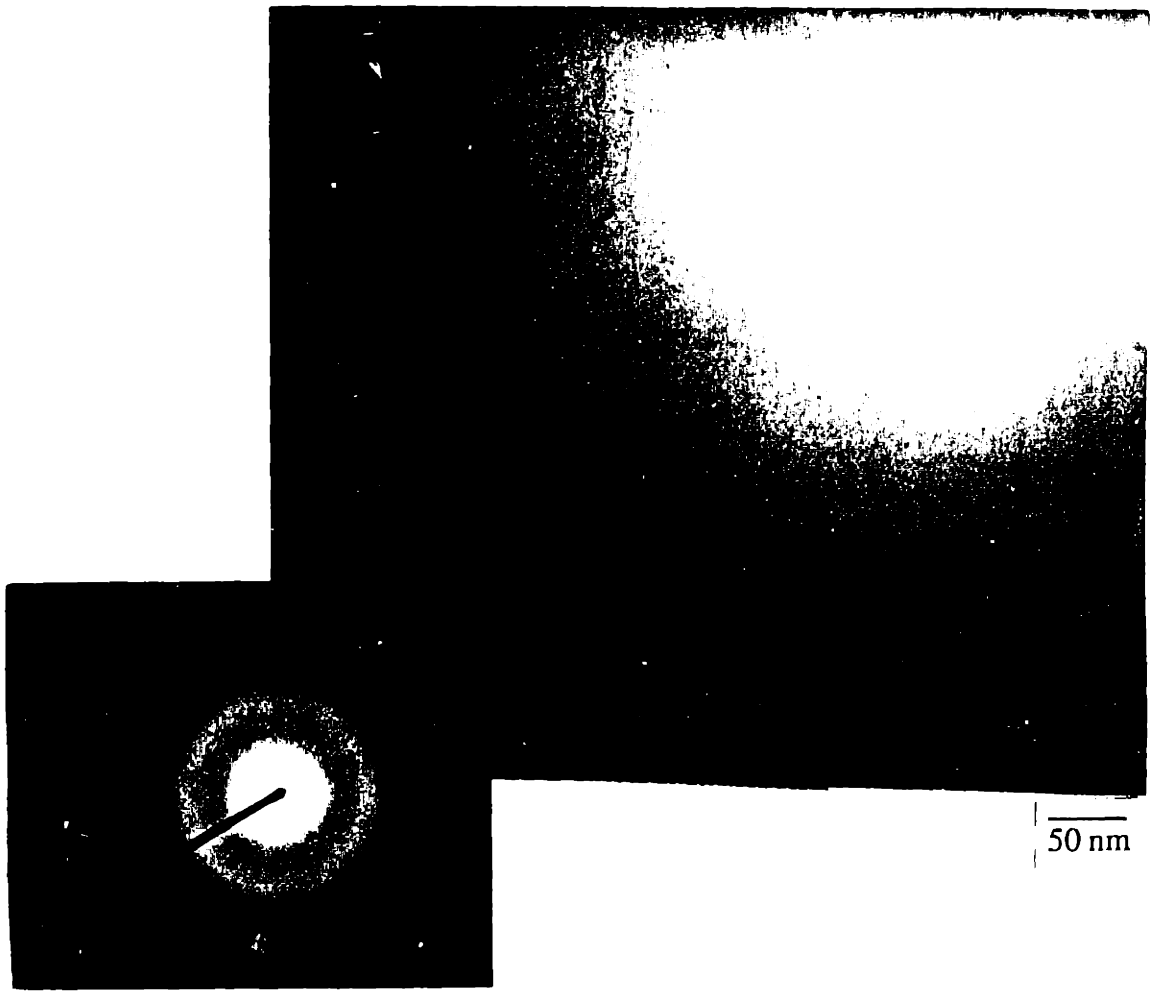

Figure 3.17 (a)
Hot stage TEM bright field micrograph and diffraction pattern for the Al_2O_3-Y_2O_3-ZrO_2 eutectic glass in the as-quenched condition.

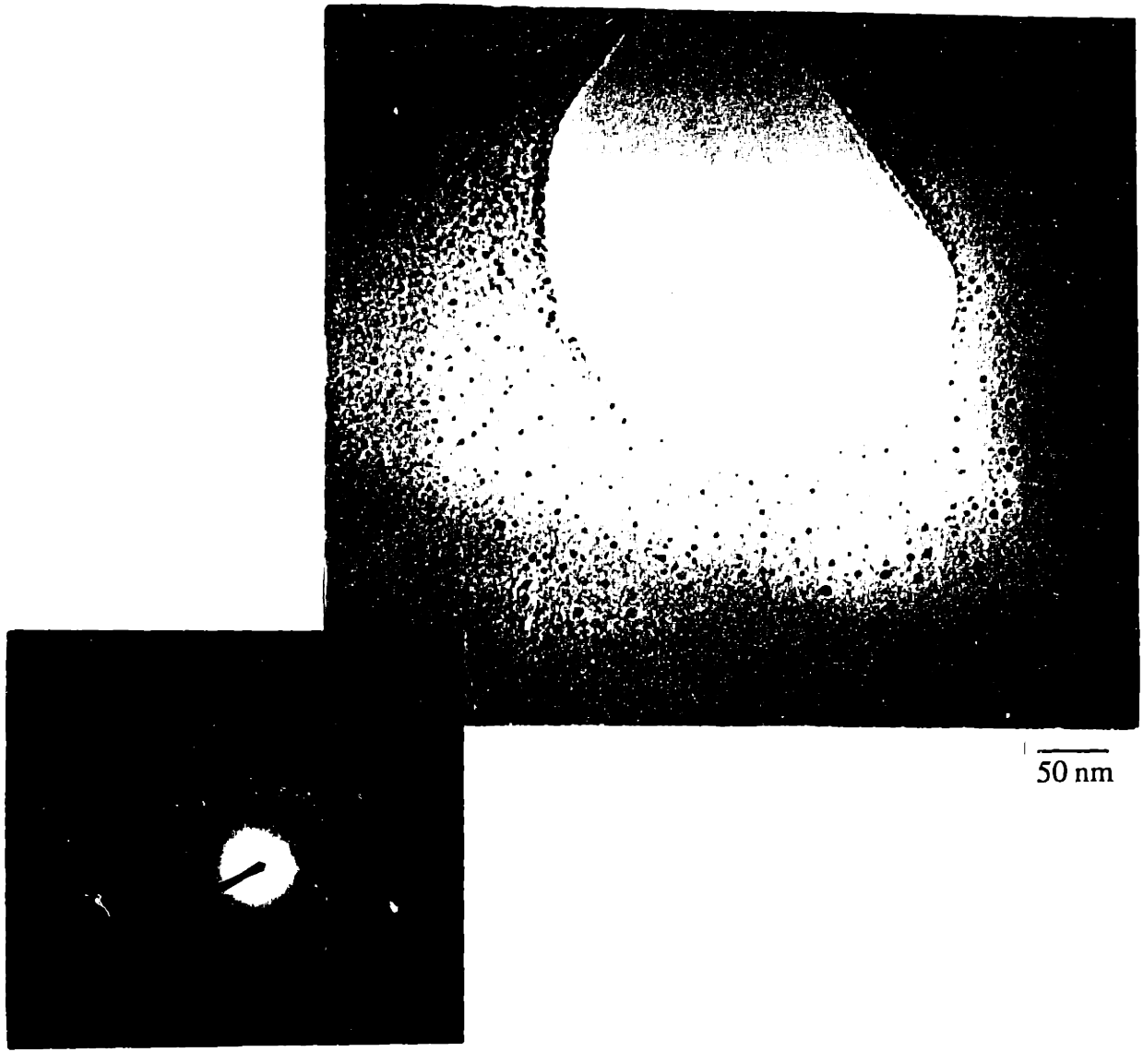

Figure 3.17 (b)
At 1100°C for 5 minutes. c-ZrO_2 crystallites (~2.5 nm) are embedded in the glass. The (111) crystalline ring from c-ZrO_2 is seen in the diffraction pattern along with the amorphous halo.

Figure 3.17 (c)
At 1194°C for 30 minutes. Further growth of the c-ZrO_2 crystallites to a size ~7 nm. Note the uniform grain size of the crystalline materials in both (b) and (c).

STEM

The Al_2O_3-ZrO_2 heat treated samples were examined in the STEM in order to determine the chemical composition of the phases. To interpret the x-ray spectra, the method devised by Cliff and Lorimer (1972) for a thin film was employed which is given by:

$$\left[\frac{C_{Al}}{C_{Zr}}\right] = k_{AlZr}\left[\frac{I_{Al}}{I_{Zr}}\right] \tag{3.9}$$

Where C_{Al} and C_{Zr} are the concentrations of Al and Zr by weight in the examined area and k_{AlZr} is the factor which relates the concentrations to the integrated Kα x-ray counts for Al and Zr, I_{Al} and I_{Zr}. The concentrations of Al_2O_3 and ZrO_2 can be easily calculated from the known concentrations of Al and Zr, assuming a stoichiometric composition of oxygen. This is a good assumption as our rapidly solidified flakes are either transparent or white. This indicates that the material has not been depleted in oxygen to a significant degree, as reduced rapidly solidified Al_2O_3-ZrO_2 compositions are grey or black.

The thin film criterion assumes there was no electron energy loss or scattering and no x-ray absorption or fluorescence in the specimen. To determine if the sample is in a thin film regime, the Philibert-Tixier (1968) equation is used:

$$t_i < \frac{0.1}{\chi_i \rho} \tag{3.10}$$

where t is the thickness, χ_i is the product of the mass adsorption coefficient (μ/ρ) of the *i* th element and the detector angle. If any element fails this criterion, the thin film approximation is not met and an adsorption correction must be made. For Al_2O_3-ZrO_2 compositions, $(\mu/\rho)_{Al}$ = 1723.2 gm/cm^3 and $(\mu/\rho)_{Zr}$ = 5.5 gm/cm^3 [Heinrich (1966)], ρ is estimated to be 4.2 gm/cm^3 and the detector is at an 20° angle from the sample. Inserting these numbers in Eq.(), it is found that the thickness must be < 50 nm for the thin film criterion to apply.

It is possible to calculate k_{AlZr} for a thin film if the elemental x-ray generation parameters are known along with the detector efficiencies, as outlined by Zaluzec (1979). To ensure the thin film criterion was met while collecting the spectra, the experimental value obtained during the data collection were compared to the calculated value and analyzed only those areas where there was close agreement, usually near the edges of the specimen. The experimental values were obtained by scanning a bulk region approximately 0.2 by 0.2 μm in size, counting for 60 sec.

Figure 3.18 shows the analytical results for the STEM analysis for Al_2O_3-ZrO_2 samples heat treated for various temperatures The smaller crystallites are from lower temperature and time heat treatments. The larger crystallites are from the high temperature heat treatments. For small particle sizes, the grains of both phases are supersaturated with the other component. For grains <100 nm, the t-ZrO_2 phase has between 15-30 mol% Al_2O_3 and the δ-Al_2O_3 phase has between 10-18 mol% ZrO_2. Under extended heat treatments, the grains grow and their compositions move to the equilibrium concentrations at sizes >200 nm. A linear relationship between composition and crystallite size in this temperature range can be fitted for both phases:

$$C_Z = 0.8055+1.192\text{x}10^{-3}\, d_Z\ (\text{nm}) \qquad (3.11)$$

$$C_{Z_A} = 0.1343-6.09\text{x}10^{-4}\, d_A\ (\text{nm}) \qquad (3.12)$$

where C_Z is the concentration of ZrO_2 in the ZrO_2 phase, d_Z is the size of the ZrO_2 crystallite, C_{Z_A} is the concentration of ZrO_2 in the Al_2O_3 phase and d_A is the size of the Al_2O_3 crystallite.

The probe was also placed on t- and m-ZrO_2 grains of similar size to determine if there was a compositional difference. The maximum t-ZrO_2 grain size found was ~0.3 μm, grains larger than this size transformed to the monoclinic form upon cooling. No detectable change in Al_2O_3 composition was found between the two polymorphs of similar size.

If Al_2O_3 chemically stabilizes the ZrO_2 polymorph, the lattice would shrink from:

$$Al_2O_3 \xrightarrow{2\,ZrO_2} 2Al'_{Zr} + 3O_O + V^{\cdot\cdot}_O \qquad (3.13)$$

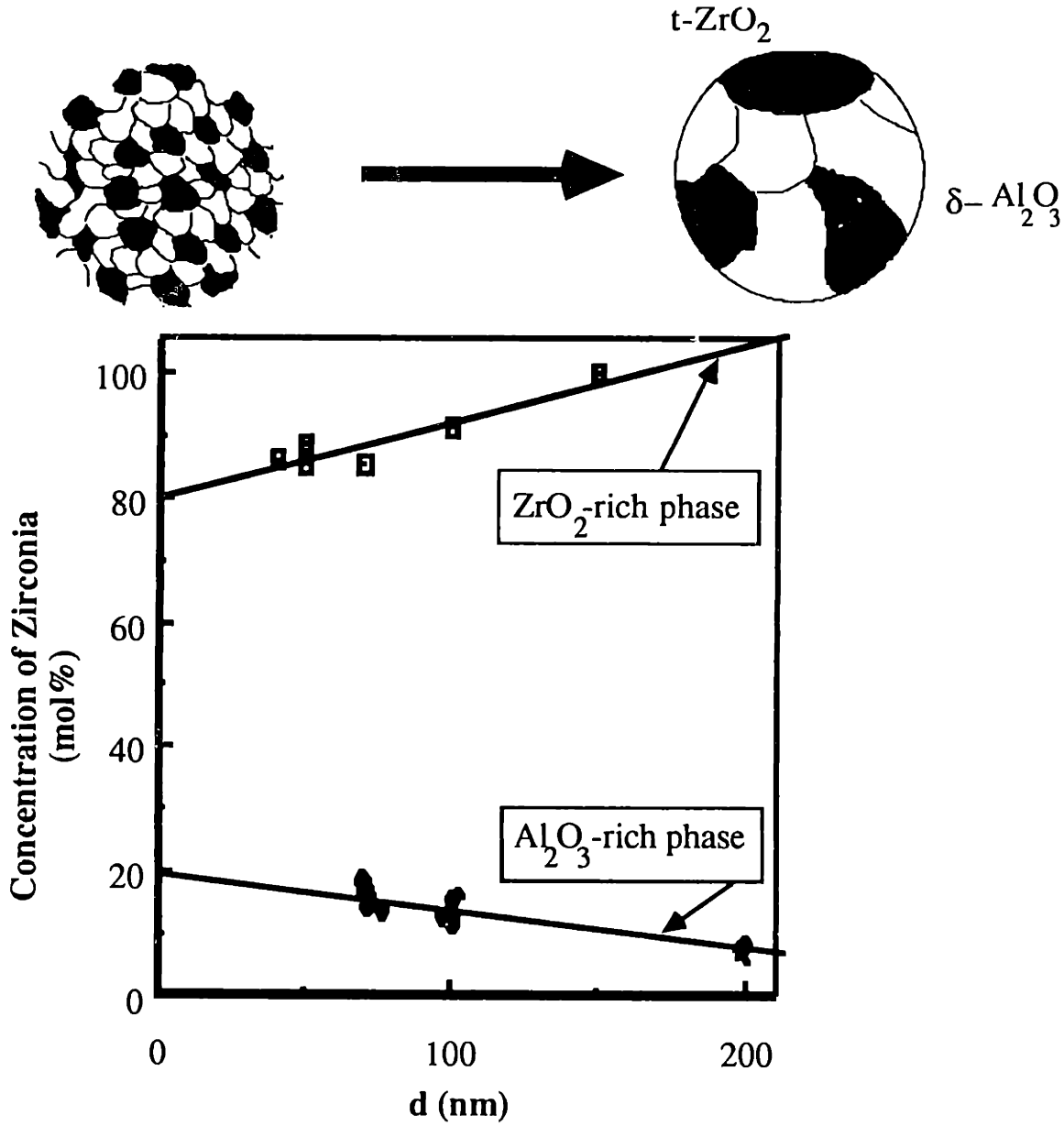

Figure 3.18

Concentration of ZrO_2 as a function of crystallite size for ZrO_2 and Al_2O_3 rich phases. The smaller crystallites are from lower temperature and time heat treatments. The larger crystallites are from the high temperature heat treatments.

However, the x-ray diffraction data did not show any detectable lattice parameter change with Al_2O_3 content, which suggests that the Al ions are most likely sitting in the center of the oxygen octahedron in the center of the cell according to this reaction:

$$Al_2O_3 \xrightarrow{\frac{3}{2}ZrO_2} Al_i^{\cdots} + 3O_O + \frac{3}{2}V_{Zr}^{''''} \qquad (3.14)$$

In this case, vacancies on the Zr sublattice are created. It would be possible to write the reaction such that oxygen vacancies are also generated, but this would point to chemical stabilization by a decreased coordination of oxygen around the Zr ions, as indicated in Eq (3.14). In addition, if enough oxygen vacancies were created, then stabilization of c-ZrO_2 should result for large Al_2O_3 concentrations, which did not occur. The Al^{3+} ionic radius (0.053 nm) is much smaller than cation radii in other sesquioxides, such as Y_2O_3 (0.089 nm); hence the size of the alloying cation appears to be the limiting factor in whether an oxide will stabilize c-ZrO_2.

Figure 3.19 shows the grain size as a function of reciprocal temperature for three separate samples. The data was plotted from measuring the sizes from the TEM micrographs for samples which had the t-ZrO_2 and δ-Al_2O_3 phases coexisting. The growth of the t-ZrO_2 crystallites is linear in an Arrhenius plot in a temperature range of 950-1150°C. It is clear that the mechanisms of growth of the tetragonal particles must vary through the course of the heat treatments. The activation energy for the growth would change when the δ-Al_2O_3 transforms into α-Al_2O_3. Interface controlled continuous grain growth occurs in situations where there is a high driving force for the transfer of atoms across the boundary and the interface is disordered or diffuse. In this case, the boundary is unstable and can add material across the interface at all points with equal ease. Due to the extremely fine grain size found in these materials, it is a reasonable to assume that long-range diffusional transport within the grains is not the limiting factor in the growth of the crystallites. The velocity of the boundary can be modeled using absolute reaction rate theory, expressed by:

$$v = \delta_B \nu \left[\frac{\Delta g^C}{kT}\right] \exp\left[\frac{-\Delta g^+}{kT}\right] \qquad (3.15)$$

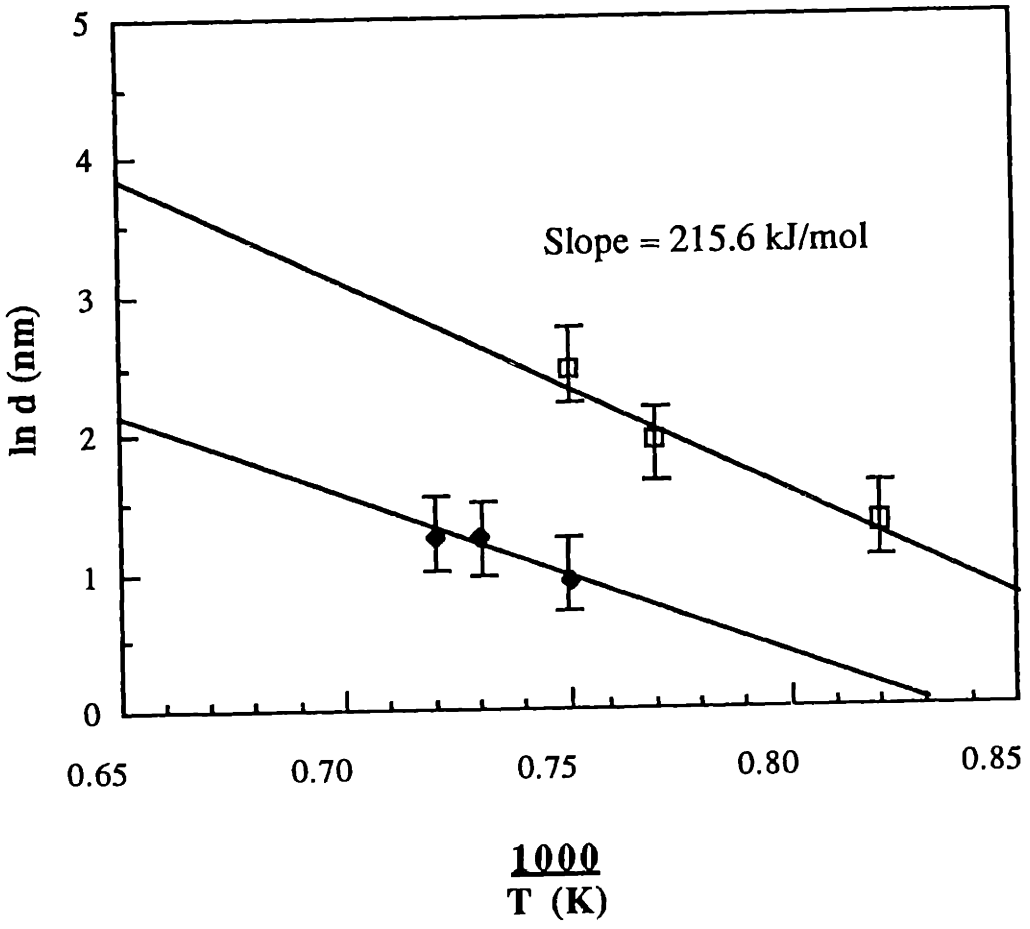

Figure 3.19

Plot of the t-ZrO_2 crystallite size as a function of reciprocal temperature growing in a δ -Al_2O_3 matrix for two different experiments.

where v=dr/dt, the change of the radius with time, δ_B is the width of the interface, v is the attempt frequency, Δg^+ is the activation barrier that the must be overcome when the atoms move across the interface, and $\Delta g^C/kT$ is the chemical driving force for the reaction, which can be generalized for a uniform grain size to be $2\sigma/r$. The attempt frequency can be expressed as $\nu=kT/Nh$, where N is the number of atoms surrounding the grain that can cross the interface and h is Planck's constant. Inserting these expressions into Eq.(3.15) and integration, the expression for the size of the grain can be written as:

$$r = \left\{ \frac{2\delta_B \sigma t}{Nh} \right\}^{\frac{1}{2}} \exp\left[\frac{\Delta s^+}{2k} \right] \exp\left[\frac{-\Delta h^+}{2kT} \right] \qquad (3.16)$$

where the initial size of the crystallite is taken as zero. Thus, the activation energy measured in Figure 3.19 for grain boundary migration is found to be 107.8 kJ/mole or 1.1 eV. For comparison, the migration energies for defects in pure, c-ZrO_2 are presented in Table 3.5, calculated by Mackrodt and Woodrow (1986). The migration energy of the Zr vacancies is smaller in the lattice than for the one measured for diffusion across the grain boundary, which is further evidence that the growth of the t-ZrO_2 phase is interface controlled.

This comparison is not entirely valid as the migration energy taken from Table 3.5 is for c-ZrO_2 where there are only intrinsic Zr vacancies present and a high oxygen vacancy population. Also, in the above analysis, not only are Zr atoms jumping into the ZrO_2 grains but Al atoms are moving out of the grains into the Al_2O_3 phase, and should be taken into account in the rate expression in Eq (3.15) This increases the total migration energy and would lead to a smaller effective boundary migration energy and thus a smaller growth rate.

Defect	*Activation Energy for Migration[kJ/mole (eV)]*
$V_{Zr}^{\cdot\cdot}$	63 (0.6)
$V_O^{\cdot\cdot}$	826 (8.5)
$V_{Zr}^{\cdot\cdot}$-$V_O^{\cdot\cdot}$	846 (8.7)
$V_O^{\cdot\cdot}$ in the presence of $Al_{Zr}^{'}$	36 (0.3)

Table 3.5 Migration energies calculated for c-ZrO_2. From Mackrodt and Woodrow (1986).

3.3.2 Al_2O_3-MgO-ZrO_2 Eutectics

The crystalline samples were annealed in air at different times and temperatures and analyzed by x-ray diffraction and the results are shown in Table 3.6.

Composition	*Heat Treatment Conditions*	*Phases Present*
17.4 MgO-42.1 Al_2O_3- 40.5 ZrO_2	800-1200°C-12 min 800°C-30 min 800°C-60 min	Spinel + m+c-ZrO_2
	1600°C-12 min.	Spinel+γ-Al_2O_3 m+t+c-ZrO_2
	1000-1200°C- 30 and 60 min.	Spinel+γ-Al_2O_3 m+c-ZrO_2
	1400-1600°C- 30 and 60 min.	Spinel, γ+α-Al_2O_3 m+t+c-ZrO_2
42.1 MgO-16.6 Al_2O_3-41.3 ZrO_2	800-1600°C-12 min. 800-1000°C-30 min. 1000°C-60 min.	Spinel+MgO+c-ZrO_2
	1600°C-60 min	Spinel+MgO m+t+c-ZrO_2

Table 3.6. Summary of the results for the annealed rapidly solidified Al_2O_3-MgO-ZrO_2 ternary eutectics.

Appendix I tabulates the raw composition data in both the spinel and c-ZrO_2 phases as determined from the lattice parameters calculated from the x-ray data.

3.2.2.1 Al_2O_3-rich Eutectic

For the Al_2O_3-rich composition, the Al_2O_3-rich spinel phase is present along with c+m-ZrO_2 for heat treatments for 12 minutes for T=800°C-1200°C and at 800°C for 30-60 minutes. Although this is the same phase assemblage found in the as-quenched materials,

this does not imply that the oxide compositions in each phase are identical. The compositions of the spinel and c-ZrO_2 phases change under annealing, as discussed in the next paragraph. Nucleation of γ-Al_2O_3 occurs in samples held at 1600°C for 12 minutes and in those held at 1000°C for 30 minutes. The γ polymorph is a cubic polymorph with a spinel structure and its lattice parameter exactly matchs that of the Al_2O_3-rich spinel (see Table 1.4). In rapidly solidified MgO-Al_2O_3 compositions, the γ-phase has been found by Sarjeant and Roy (1967) for high Al_2O_3 compositions. This polymorph is stable over a wide variety of temperatures for anneal times up to 60 minutes. The transformation to α-Al_2O_3 occurs for samples held at 1400°C for 30-60 minutes. The stability of γ-Al_2O_3 is similar to the δ-Al_2O_3 phase found in the Al_2O_3-ZrO_2 binary system, which was also present up to ~1200°C. t-ZrO_2 nucleates in the c-ZrO_2 matrix only ~under anneals of 30-60 minutes for T>1400°C and under annelas of 12 minutes for T>1600°C. This is consistent with the phase diagram which reports the eutectoid decomposition temperature at 1400°C. It is possible that incipient nucleation of t-ZrO_2 occured in these samples below 1400°C, but it was not detectable from the x-ray measurements. Careful scrunity of the x-ray diffraction patterns show no indication of t-ZrO_2. The (111) d-spacings are too small for t-ZrO_2 and characteristic splitting of the c-(220) into t-(202) and t-(220) and the c-(113) into t-(113) and t-(131) peaks were not found.

As with the as-quenched material, $Mg_2Zr_5O_{12}$ was not detected. It is possible that t-ZrO_2 must be present to nucleate this phase. The results of Sim and Stubican (1987) showed that $Mg_2Zr_5O_{12}$ nucleated from single phase c-ZrO_2 only after annealing for long periods of time at 800°C where t-ZrO_2 also nucleated and Readey et al. (1988) found the presence of $Mg_2Zr_5O_{12}$ after annealing the two phase t+c-ZrO_2 below 1000°C. For these samples, t-ZrO_2 was found only after annealing above 1400°C. At lower temperatures only c-ZrO_2 was present.

Figure 3.20 shows data from the annealing experiments on the Al_2O_3-rich eutectic. The plot shows the concentration of MgO in the spinel phase and in c-ZrO_2 as a function of reciprocal temperature for annealing times of 12, 30 and 60 minutes. As shown, the MgO concentration increases in the spinel phase and decreases in the ZrO_2 phase. The MgO content increases in the spinel due to two factors. MgO diffuses from c-ZrO_2 to the spinel; simultaneously Al_2O_3 diffuses out of the spinel to form γ-Al_2O_3. Recall that the δ-Al_2O_3 phase in the binary Al_2O_3-ZrO_2 eutectic nucleated and grew with t-ZrO_2. In contrast, the γ-Al_2O_3 phase forms in this system. Presumably this may occur to minimize the surface energy between the γ-Al_2O_3 phase and the two co-existing cubic phases, spinel and

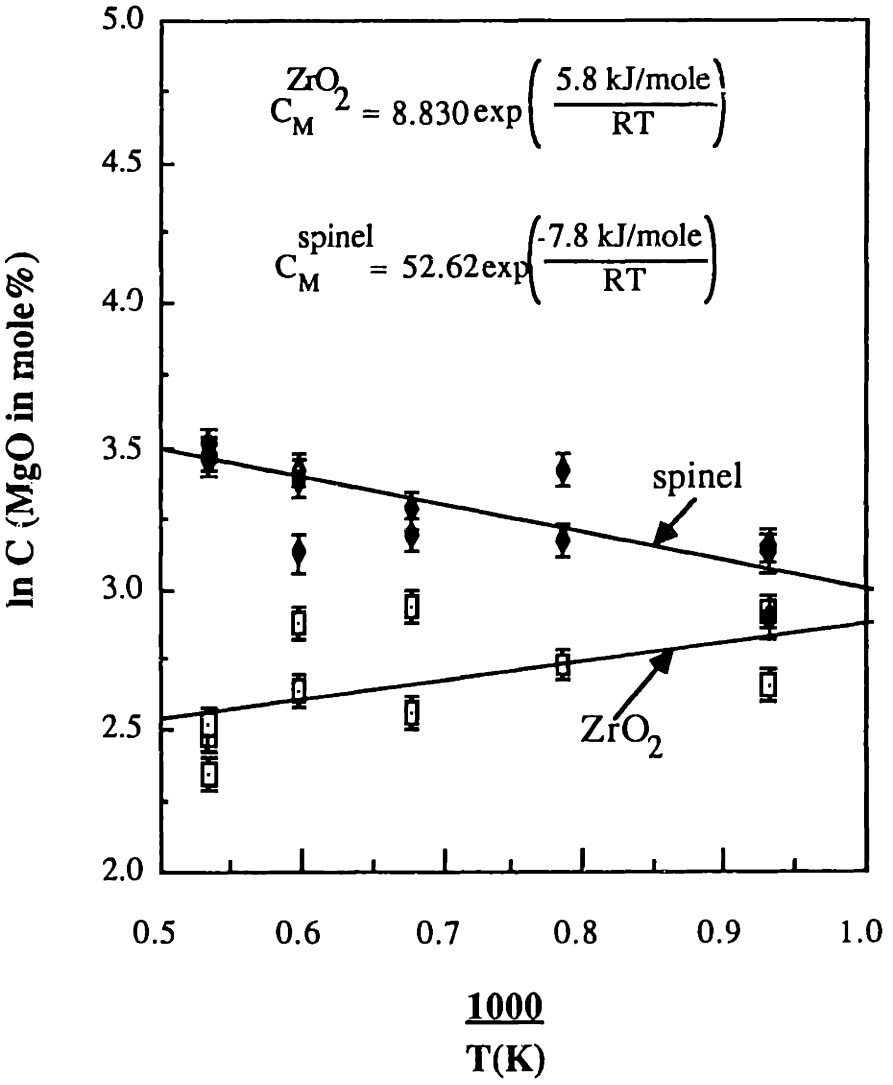

Figure 3.20
MgO concentration in ZrO_2 and spinel as a function of heat treatment temperature for the Al_2O_3-rich ternary eutectic

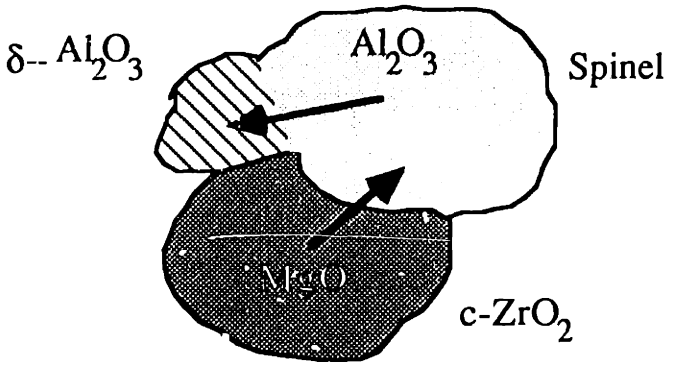

c-ZrO_2. The slopes of the concentration vs. reciprocal temperature for the three annealing times are roughly the same. When averaged they yield a slope for compositional change as a function of reciprocal temperature of 7.80 kJ/mole (0.8 eV) for the MgO concentration in spinel and 5.8 kJ/mole (0.06 eV) for the MgO concentration in c-ZrO_2. Depletion of MgO in the c-ZrO_2 results in the formation of t-ZrO_2, in accordance with the phase diagram. MgO-depleted t-ZrO_2 has been shown to nucleate and grow in regions of the cubic structure under thermal aging above 1200°C [Heuer (1981)].

The amount of Al_2O_3 diffusing out of the spinel phase can be found from a mass balance for the system, expressed by:

$$C_S Mg_x Al_{2(1-x)} O_{3-2x} + C_Z Mg_y Zr_{1-y} O_{2-y} + C_A = 1.00 \qquad (3.17)$$

where C_x is the mole fraction of each phase. The expression can be reduced to one containing only the values of x and y, the mole fraction of MgO in the spinel and c-ZrO_2 phase, respectively:

$$C_{Al_2O_3} = A - \left[M \frac{Zy}{1-y} \right] \left[\frac{1-x}{x} \right] \qquad (3.18)$$

where A, M and Z are the mole fraction of Al_2O_3, MgO, and ZrO_2, respectively. The values of x and y are found from the data presented in Figure 3.3 and are:

$$x = C_{MgO}^{spinel} = 0.5262 \exp \left[\frac{-7.8 \text{ kJ/mole}}{RT} \right] \qquad (3.19)$$

$$y = C_{MgO}^{ZrO_2} = 0.0883 \exp \left[\frac{5.8 \text{ kJ/mole}}{RT} \right] \qquad (3.20)$$

Substituting Eq.(3.19) and (3.20) into (3.18), for T>1000°C the mole fraction of Al_2O_3 forming in the system is:

$$C_{Al_2O_3} = 0.3991 \exp\left[\frac{-12.7\ \text{kJ/mole}}{RT}\right] \qquad (3.21)$$

Figure 3.21 is a plot of the mole fractions of the spinel, c-ZrO_2, and γ-Al_2O_3 phases as a function of annealing temperature. The mole fractions of the spinel and Al_2O_3 phases change significantly whereas the c-ZrO_2 does not. This indicates that the compositional change in the spinel is mostly due to the depletion of Al_2O_3 and not from the enrichment of MgO from the c-ZrO_2 phase.

The energies expressed in Eqs. 3.19 and 3.20 represent the driving force for the compositional changes in the spinel and c-ZrO_2 phases, respectively. For a dilute solution approximation, for which the activity coefficient is not a function of composition, the difference in the chemical potential between two phases, α and β for a solute of concentration $C_{i\alpha}$ in the α-phase is expressed by:

$$\frac{\Delta\mu_{\alpha\beta}}{kT} = \ln\left[\frac{C_{i\alpha}}{C_{s\alpha}}\right] \qquad (3.22)$$

where $C_{s\alpha}$ is the equilibrium composition of C_i in the α-phase, which lies along the phase boundary between the α and β phases. In the c-ZrO_2 phase, the driving force for the compositional change is the difference in the chemical potential of MgO in the spinel and c-ZrO_2. In the spinel phase, the driving force for the compositional change is the difference of the chemical potential of Al_2O_3 between the spinel and γ-Al_2O_3 phases in addition to the difference of chemical potential of MgO between the spinel and c-ZrO_2. Panda and Raj (1986) have estimated the driving force for preecipitation of γ-Al_2O_3 in Al_2O_3-rich spinel to be between 0.003-0.016 eV (0.3-1.5 kJ/mole) at 1550°C. In contrast, the driving force measured in this work is higher (Eq. 3.19) which appears to reflcet the dual driving forces for the overall compositional change. The dilute solution approximation may not be valid for the spinel system since both MgO and Al_2O_3 are considered. It is also possible that the chemical potentials for each specie are coupled, which would alter Eq. 3.21.

The fraction of m-ZrO_2 as a function of annealing temperature and time is shown in Figure 3.22. The relative amount of m-ZrO_2 is found from the x-ray diffraction results by the ratio of the (111) peak intensities:

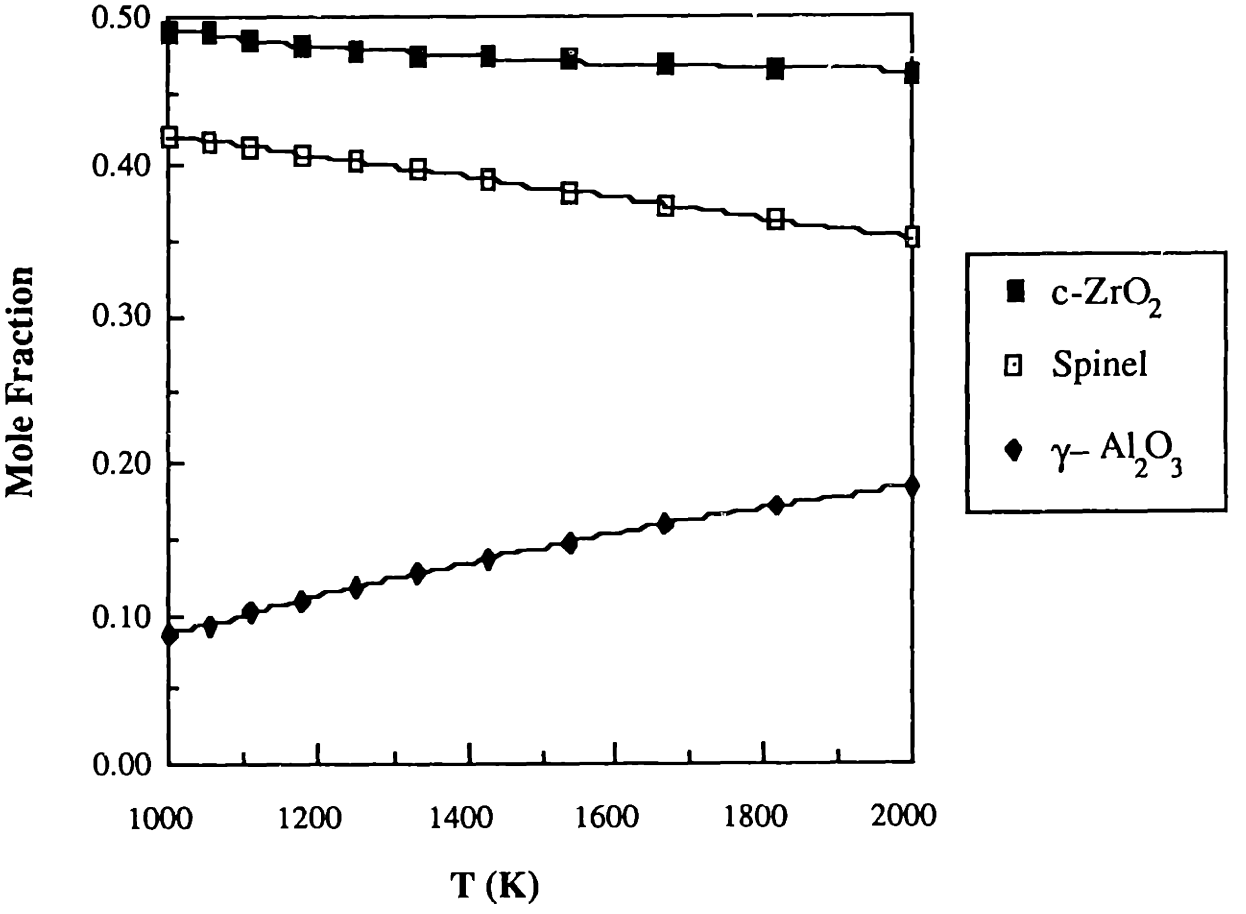

Figure 3.21

Mole fraction of each phase as a function of annealing temperature for the Al_2O_3 -rich ternary eutectic.

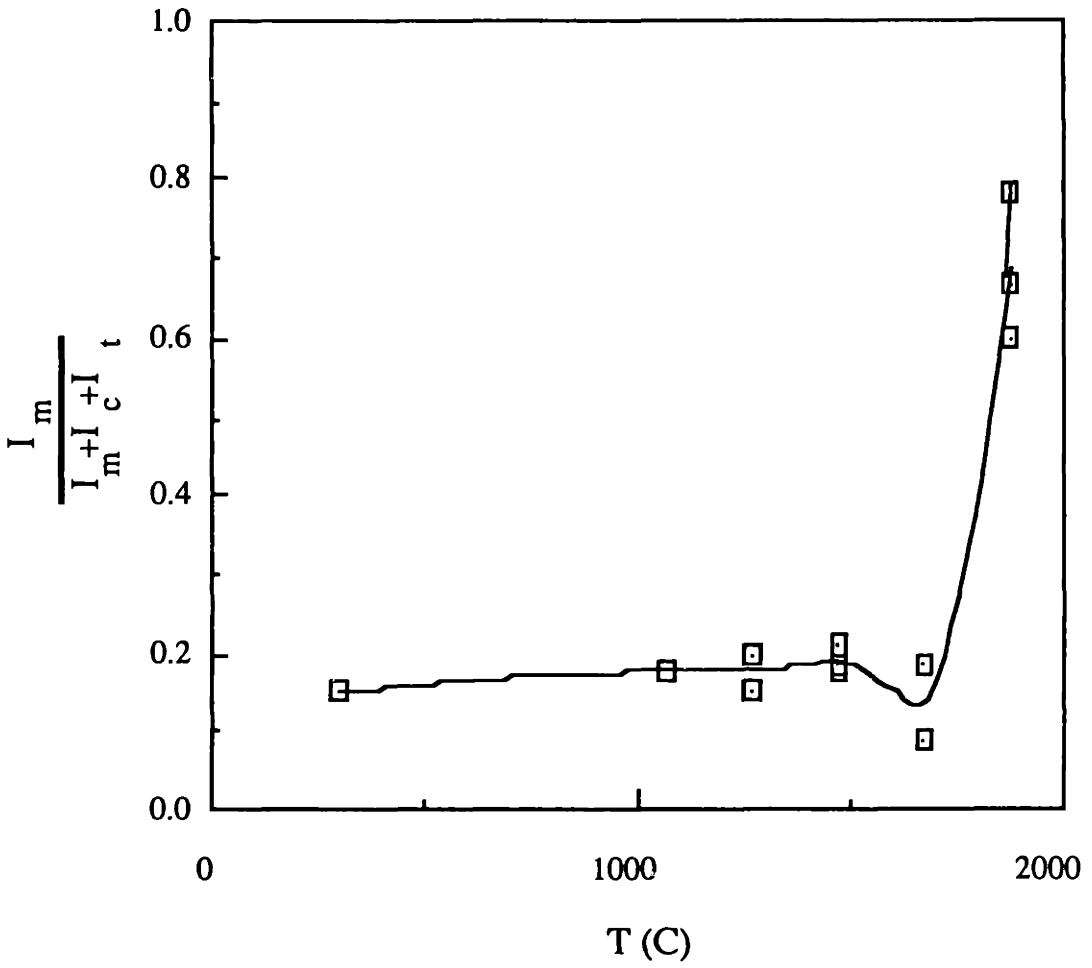

Figure 3.22
Relative fraction of monoclinic ZrO_2 as a function of annealing temperature in the Al_2O_3 -rich ternary eutectic composition for 12, 30 and 60 min.

$$f_m = \frac{I_m(111)}{I_m(111)+I_c(111)+I_t(111)} \qquad (3.23)$$

where I_m, I_c and I_t are the intensities of the 100% (111) peaks. As shown, a small fraction of m-ZrO_2 is initially present (as discussed in Sec.3.2.2). The amount does not change appreciably over temperature until 1600°C, where the relative amount is between 0.6-0.8 of the total ZrO_2. These results further indicate that the m-ZrO_2 presence in these systems is not a solidification product. If the m-ZrO_2 was quenched in from the melt, the phase would grow under heat treatments. Only at 1600°C is the temperature high enough for the decomposition of c-ZrO_2 into a MgO-rich c-ZrO_2 and an MgO-poor t-ZrO_2. The t-ZrO_2 can subsequently transform to m-ZrO_2 from cooling if the grain size is large enough or from the stress induced t->m transformation induced from crushing the sample for powder x-ray work.

Composition as a Function of Quench Rate

The spinel composition as a function of quench rate was determined. These samples consist of spinel and c+t+m-ZrO_2. The twin rolled samples ranged in thickness from 20-1600μm, depending on the speed of the rollers. The range of thicknesses found in these materials is due to several factors: (1) the liquid volume in the droplet is not constant as a function of time (2) the rollers progressively become gouged due to the abrasiveness of the solid material (3) the intense heat from the heating source causes the rollers to deform causing uneven an separation and (4) the liquid does not always hit the rollers at the same point. The cooling rate for twin roller quenched materials can be estimated from the thickness of the product by applying Eq.(3.7) using $\Delta T \sim 1530$ K, the estimated temperature difference between the liquid and the solid, R=2.54 cm, and ω = 6000rpm. A plot of the MgO concentration in the spinel as a function of cooling rate and flake thickness is shown in Figure 3.23. For increasing cooling rates (decreasing thicknesses), the MgO concentration increases, which is in agreement with the trend in the annealing data so far presented. Thus, it is possible to tailor the composition of the spinel by varying the roller speed. The oomposition in the spinel is very sensitive to small

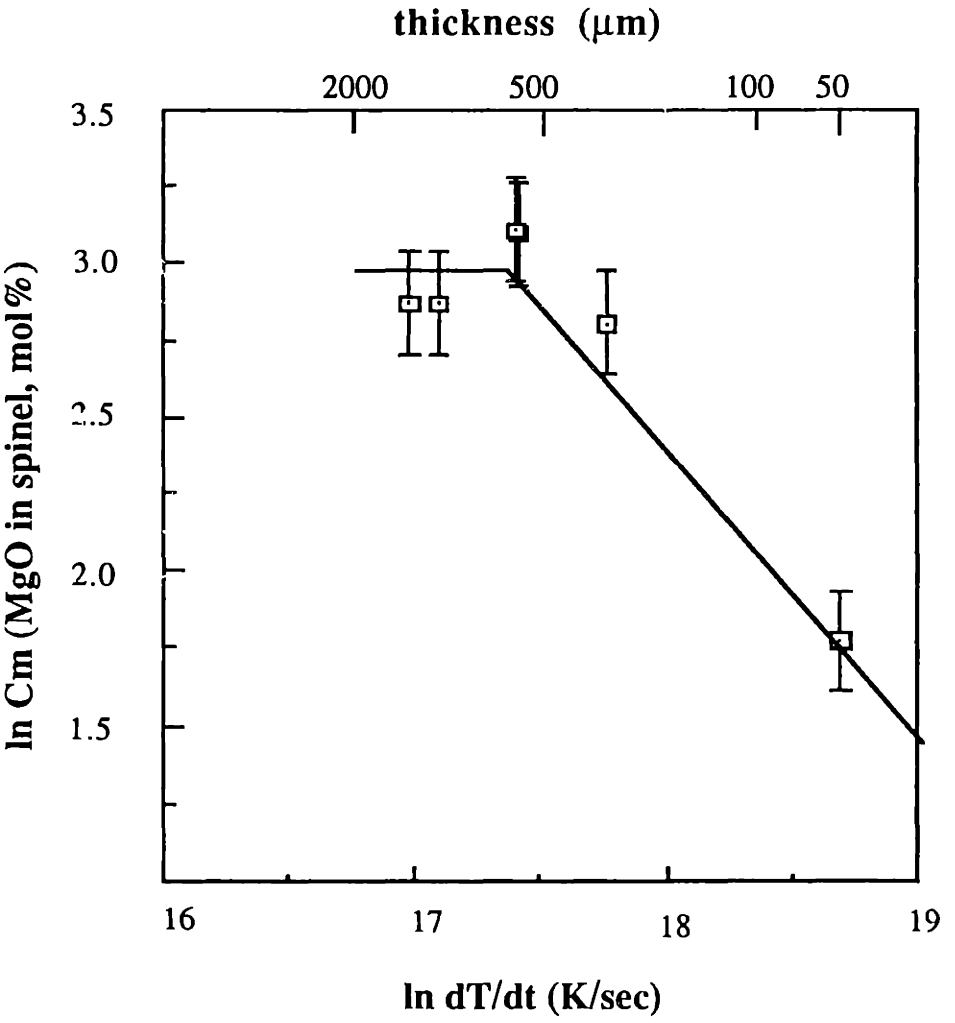

Figure 3.23

Concentration of MgO in the spinel phase in the Al_2O_3 -rich eutectic as a function of cooling rate and flake thickness.

changes in cooling rate. A cooling rate range between 1-4x10^7 K/sec can result in the variation of spinel composition from 17-50 mol% MgO, which was found in this system.

The fraction of m-ZrO_2 found in the as-quenched Al_2O_3-rich eutectic samples is also found to be a function of the cooling rate. Figure 3.24 shows the fraction of m-ZrO_2 found with t-ZrO_2 as a function of flake thickness. For comparison, the as-quenched data for the 50μm thick flakes with c+m-ZrO_2 are included. As shown, for flake thicknesses smaller than ~300μm, the monoclinic fraction is very small. It increases rapidly up to thicknesses of 1000μm, at which point almost all of the ZrO_2 is in the monoclinic polymorph. The presence of t-ZrO_2 is due to the depletion of MgO in the ZrO_2 phase which makes the composition fall in the two phase c+t region. The monoclinic ZrO_2 occured from the factors mentioned in Sec.3.2.2 in tandem with the larger grain size generated during the slower cooling process. As with the monoclinic fraction found under annealing, these large grains could have undergone the stress induced t->m phase transformation during cooling or from crushing the samples for the powder x-ray work.

3.2.2.2 MgO-rich Eutectic

For the heat treated MgO-rich eutectic, the spinel, MgO and c-ZrO_2 phases co-exist over a large temperature range for various times. As with the Al_2O_3 -rich composition, these phases are changing in composition during annealing. Only in samples held at 1600°C for 60 minutes is the presence of m+t-ZrO_2 detected along with c-ZrO_2. As with the as-quenched materials, $Mg_2Zr_5O_{12}$ was not detected. Rossell and Hannink (1984) found the phase after rapid quenching in the high MgO region of the phase diagram. It is possible that the phase is present, but undetectable by the x-ray measurement in this work. For their work, they employed electron diffraction to verify the presence of the phase.

Figure 3.25 shows the data from the annealing experiments on the MgO-rich eutectic. As shown, the MgO content in the spinel remains constant within experimental error over the annealing temperature range while the c-ZrO_2 shows a marked decrease in MgO concentration with increasing annealing temperature. The MgO diffuses out of the c-ZrO_2 phase into the MgO phase in accordance with the phase diagram. The starting composition of c-ZrO_2 is so rich with MgO (as-quenched composition of 38.2 mol% MgO) that only under extended heat treatments below 1400°C did t-ZrO_2 nucleate and grow in the cubic matrix. This behavior is in contrast with the ZrO_2 in the Al_2O_3-rich eutectic where

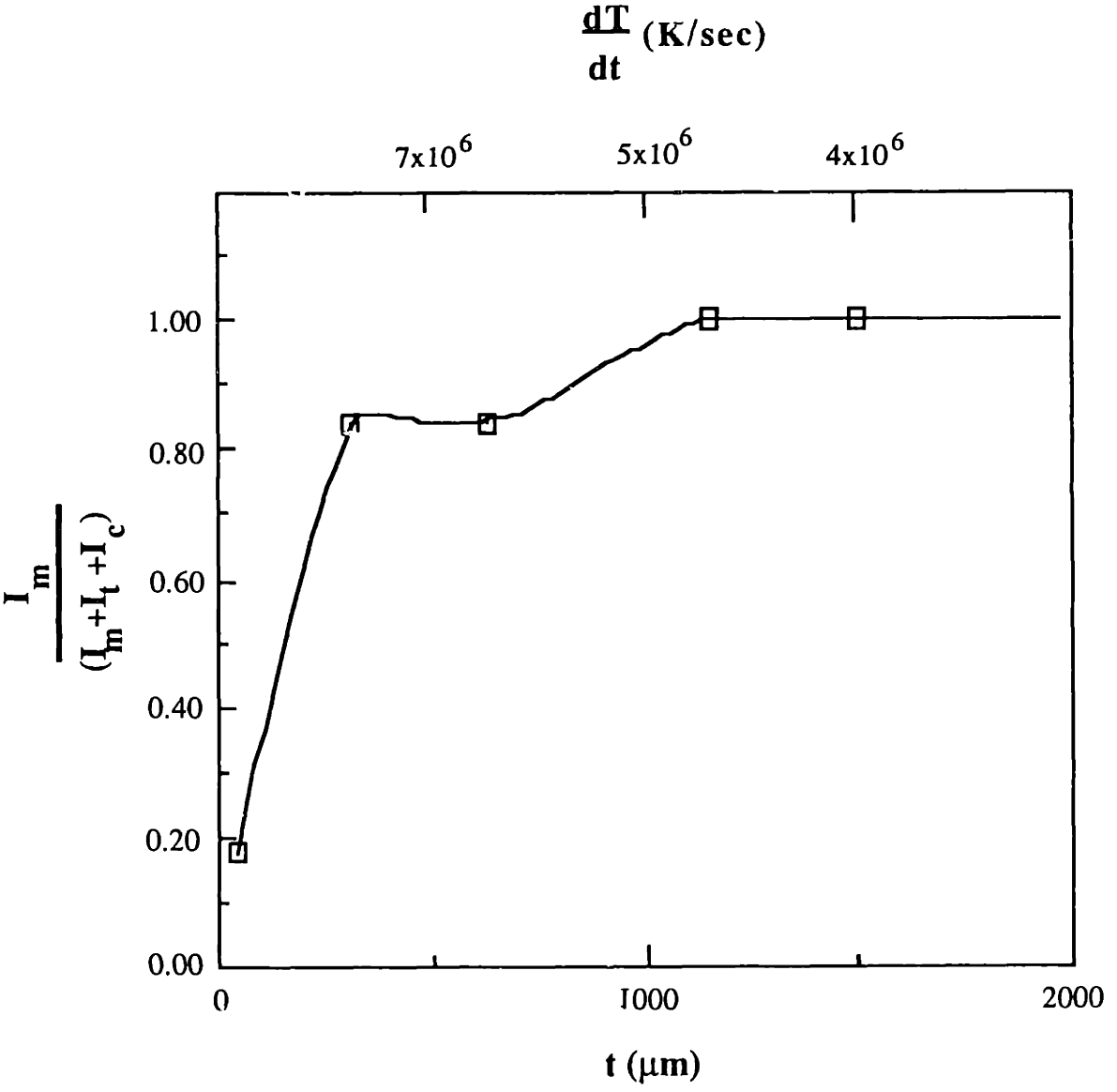

Figure 3.24

Fraction of m-ZrO_2 as a function of thickness and cooling rate for the Al_2O_3 -rich ternary eutectic..

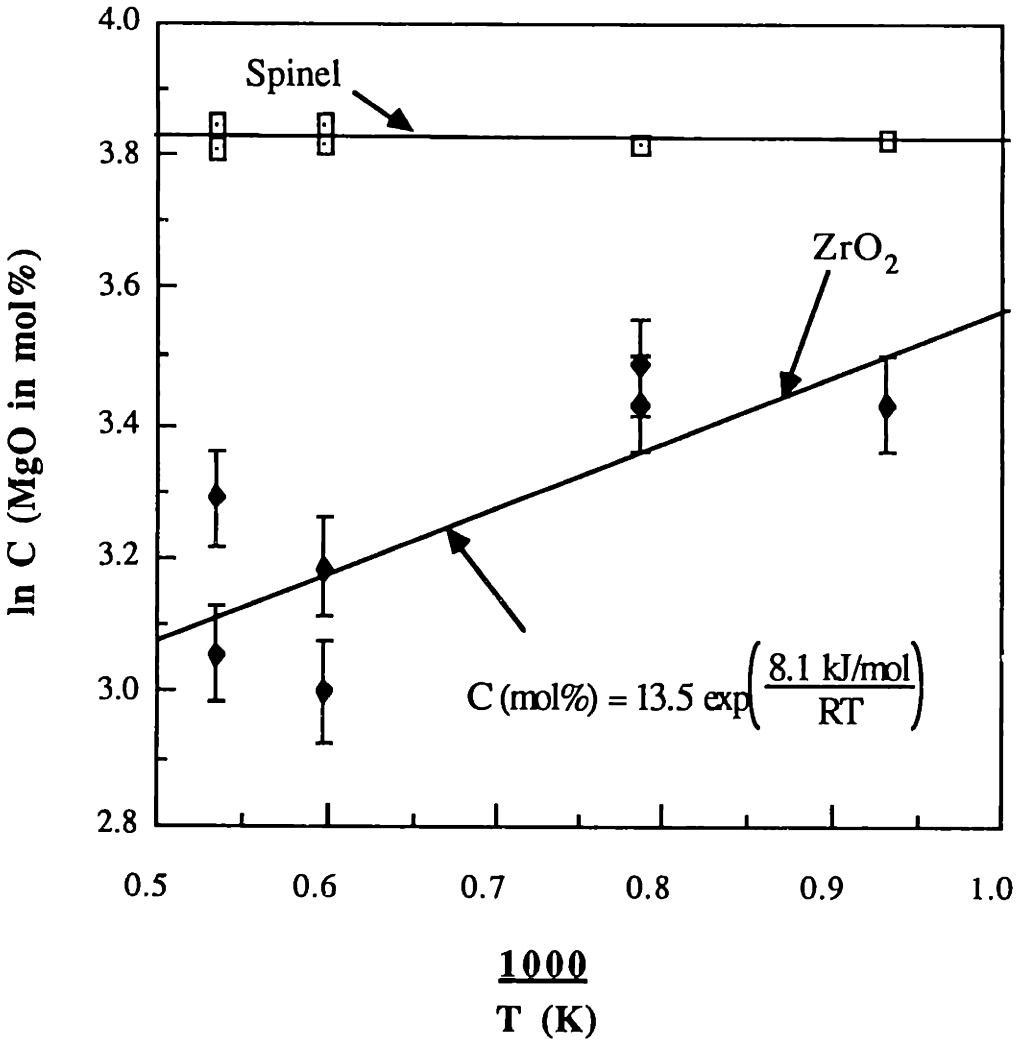

Figure 3.25
Concentration of MgO in the ZrO_2 phase (bottom) and spinel phase (top) as a function of heat treatment temperature for the MgO-rich ternary eutectic.

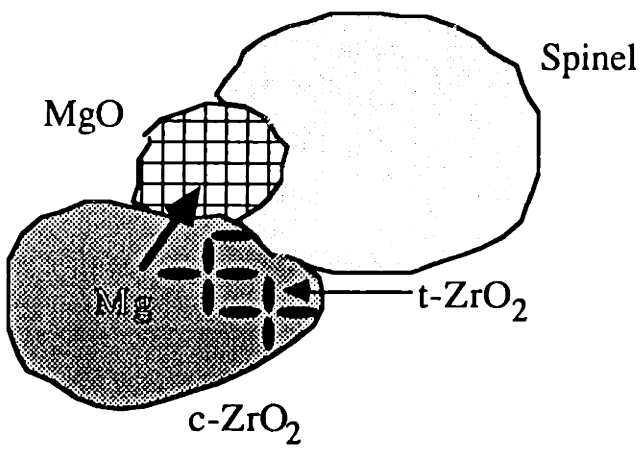

t-ZrO_2 is found for most annealing conditions. It should be noted that the composition of MgO in the MgO-rich eutectic falls above the eutectoid composition (13.1 mol% MgO) whereas in the Al_2O_3-rich composition it falls below. The compositional change follows Arrhenius behavior, expressed by:

$$C\ (MgO,\ mol\%) = 13.5 \exp\left[\frac{8.1\ kJ/mole}{RT}\right] \tag{3.24}$$

For the spinel phase, the calculated as-quenched composition (46.2 mol% MgO) is nearly the stoichiometric one; however, as indicated in Sec. 3.22, there is uncertainty as to the exact lattice parameter of stoichiometric spinel in this work. It is assumed that during annealing at high enough temperatures, the spinel composition would go to equilibrium and maintain a stoichiometric composition. Starting with 46.2 mol% MgO, a change of 3.8 mol% would yield a difference in lattice parameter of 0.0019 nm, which is a measurable amount by x-ray diffraction. Since this was not measured, it is possible that the as-quenched composition was closer to the stoichiometric one. Chiang and Kingery (1988) did not detect changes in lattice parameter for small deviations (~40 mol% MgO) in the two phase (spinel +MgO), MgO-rich portion of the phase diagram whereas Sarjeant and Roy did in rapidly solidified magnesia aluminate spinels. Figure 3.26 shows the lattice parameter of spinel as a function of MgO content from the results of these works. Other workers have also reported no change in lattice parameter with MgO excess compositions [Alper et al.(1962)]. The results of Sergeant and Roy seem doubtful as they present a linear relationship over the entire MgO-Al_2O_3 range. For the Al_2O_3-rich compositions, vacancies are created on the cation sublattice along with Al substitutions on the Mg sites . For the MgO-rich compositions, cation intersititial are created along with the substitution of Mg on the Al sites. These two reactions should not give rise to a the same dependence on lattice parameter with composition..

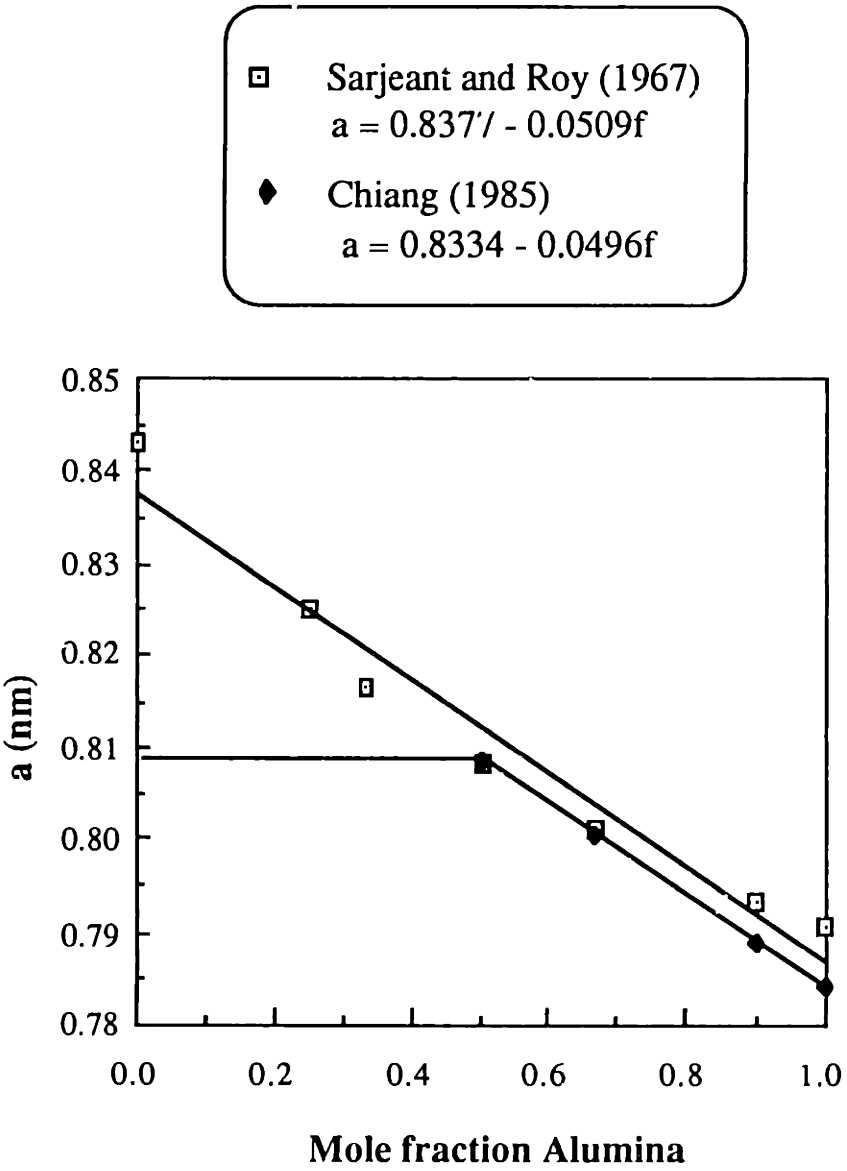

Figure 3.26

Lattice parameter of magnesia aluminate spinel as a function of alumina content. Data taken from Sarjeant and Roy (1967) on rapidly solidified compositions. Data from Chiang (1985) taken from sintered powder work.

4. CONCLUSIONS

Binary and ternary eutectic and off-eutectic compositions in ZrO_2 containing ceramics were melted and rapidly solidified with several different techniques. The method which generated the highest quench rates and largest volume of amorphous materials was the crucibleless melting technique with RF heating and twin roller quenching. Cooling rates were determined to be ~10^7 K/sec. The other techniques had significantly lower cooling rates. Al_2O_3-ZrO_2 ceramics rapidly soldified using different techniques exhibit a wider variety of microstructures, depending on local solidification conditions. The microstructural development may be understood in terms of the theory of rapid solidification of eutectic systems. For all quench rates examined, tetragonal ZrO_2 was stabilized unless a chemical stabilizer (MgO, Y_2O_3) was added. The microcrystalline materials in the Al_2O_3-ZrO_2 system exhibit a degree of supersaturation of one phase in the other. This indicates that local equilibrium at the liquid-solid interface is not attained during solidification. Under heat treatments of the Al_2O_3-ZrO_2 eutectic glasses, the first phase to nucleate is t-ZrO_2 followed by δ-Al_2O_3. Al_2O_3 does not chemically stabilize t-ZrO_2; it only provides mechanical stabilization due to its higher elastic modulus. The apparent activation energy for grain growth of t-ZrO_2 growing in a δ-Al_2O_3 matrix was calculated. Growth of these crystallites involves a change in composition, which is approximately a linear function of grain size.

The addition of Y_2O_3 to form the Al_2O_3-Y_2O_3-ZrO_2 eutectic increases the viscosity of the melt and makes it an easier glass former than the binary system. The yttrium atoms are not network formers but act as intermediates in the glassy structure. Devitrification of the glass results in the formation of c-ZrO_2, in contrast with the Al_2O_3-ZrO_2 binary where the t-ZrO_2 phase nucleated first.

The addition of MgO to the system causes the formation of highly defective spinels which co-exist with c-ZrO_2 in the Al_2O_3-rich ternary eutectic composition. The nucleation of the primary Al_2O_3 phase is completely suppressed. Annealing these materials results in the formation of the γ-Al_2O_3 phase, in contrast to the nucleation of δ-Al_2O_3 in the binary Al_2O_3-ZrO_2 eutectic composition. This phase grows by depleting the Al_2O_3-rich spinel of Al_2O_3. The composition of the spinel changes due to two factors, diffusion of Al_2O_3 into γ-Al_2O_3 and diffusion of MgO out of the c-ZrO_2. The apparant activation energies for growth were calculated from x-ray data.

For the MgO-rich ternary eutectic, rapid solidification yielded a three phase assemblage of MgO, a nearly stoichiometric spinel and c-ZrO_2. Annealing these materials results in the growth of the MgO phase from diffusion of MgO out of c-ZrO_2. The spinel composition does not change significantly. Depletion of MgO from the c-ZrO_2 results in the eventual formation of t-ZrO_2, but only at high temperatures.

APPENDIX I

Raw data for the annealing results for the Al_2O_3-rich ternary eutectic composition.

	Composition (mol%) of MgO in spinel for 12, 30 and 60 min.			Composition (mol%) of MgO in c-ZrO_2 for 12, 30, and 60 min			Phases Present					
T (C)	C_{Ms}-12	C_{Ms}-30	C_{Ms}-60	C_{Mz}-12	C_{Mz}-30	C_{Mz}-60	γ-Al_2O_3	α–Al_2O_3	spinel	c-ZrO_2	t-ZrO_2	m-ZrO_2(*)
800												
1000												
1200	24.3			19.2			no	no	√	√	no	0.18
1400												
1600	31.7			15.3			√	√	√	√	√	0.67
800		23.4			17		no	no	√	√	no	0.18
1000		23.9			15.9		√	no	√	√	no	0.2
1200		24.1			13.4		√	no	√	√	no	0.18
1400		31.8			14.6		no	√	√	√	√	0.53
1600		29.4			12.5		no	√	√	√	√	0.79
800			22.6			21.8	no	no	√	√	√	0.17
1000			21			13.7	√	no	√	√	no	0.15
1200			23.2			21.8	√	no	√	√	no	0.21
1400			22.6			14.2	no	√	√	√	√	
1600			32.2			14.8	no	√	√	√	√	0.4

(*) Relative amount of m-ZrO_2 present.

Raw data for the annealing results for the MgO-rich ternary eutectic composition.

	Composition of MgO (mol%) in spinel for 12, 30, and 60 min.			Composition of MgO (mol%) in c-ZrO_2 for 12, 30 and 60 min.			Phases Present				
T(C)	C_{Ms}-12	C_{Ms}-30	C_{Ms}-60	C_{Mz}-12	C_{Mz}-30	C_{Mz}-60	MgO	spinel	c-ZrO_2	t-ZrO_2	m-ZrO_2(*)
800	45.8			38.4			no	√	√	no	no
1000	48.3			33.9			no	√	√	no	no
1200											
1400	46.9			25.9			no	√	√	no	no
1600	46.7			29.8			√	√	√	no	no
800											
1000		45.6			40.8		no	√	√	no	no
1200											
1400											
1600											
800											
1000			38.7			52.1	√	√	√	no	no
1200			57.8			7.1	no	√	√	√	√
1400											
1600											

(*) Relative amount of m-ZrO_2 present.

APPENDIX II

DENSITY CALCULATIONS

The as-quenched crystalline materials in the Al_2O_3-rich Al_2O_3-MgO-ZrO_2 system consist of spinel [$Mg_xAl_{2(1-x)}O_{3-2x}$] and c-ZrO_2 [$Mg_yZr_{1-y}O_{2-y}$], where x=mole fraction of MgO in the spinel phase and y=mole fraction of MgO in ZrO_2. The total density of the material is:

$$\rho_t = \sum_{i=1}^{n} V_{f_i} \rho_i \tag{1A}$$

where n=number of phases and V_f is the volume fraction of the phase, which is expressed by:

$$V_{f_i} = \frac{V_i}{\sum_{j=1}^{n} V_j} = \frac{\dfrac{(MW)_i C_i}{\rho_t}}{\sum_{j=1}^{n} \dfrac{(MW)_j C_j}{\rho_j}} \tag{2A}$$

In the above expression, $(MW)_i$ is the molcular weight of each phase and C_j is the mole fraction of that phase. The density of a phase can be written:

$$\rho_i = \frac{(MW)_i Z_i}{N a_o^3} \tag{3A}$$

where Z_i is the number of molecular units per cell, N is Avodgadro's number and a_o is the lattice parameter. Then, inserting Eqs. (2A) and (3A) into (1A), the total density of the *n*-phase material is:

$$\rho_t = \sum_{i=1}^{n} \left[\frac{\frac{(MW)_i C_i}{N}}{\sum_{j=1}^{n} \frac{a_j^3 C_j}{Z_j}} \right] \qquad (4A)$$

The c-ZrO_2 lattice parameter is written as [Aleksandrov et al.(1976)]:

$$a\,(\text{Å}) = \frac{4}{\sqrt{3}} \left[r_{Zr} + r_O + \frac{\sum_k (P_k M_k \Delta r_k)}{100 + \sum_k M_k (P_k - 1)} \right] \qquad (5A)$$

where r_{Zr} and r_O are the ionic radii of the Zr and O, respectively, $\Delta r_k = r_{Mg} - r_{Zr}$, P_k is the number of anions in the stabilizing oxide and M_k is the mole fraction of the stabilizing oxide. The lattice parameter of the spinel phase is [Chiang (1985)]:

$$a_o(\text{Å}) = 8.313 - 0.46(1-x) \qquad (6A)$$

And

$$MW_Z = AW_{Mg}(y) + AW_{Zr}(1-y) + AW_O(2-y) \qquad (7A)$$

$$MW_S = AW_{Mg}(x) + AW_{Al}[2(1-x)] + AW_O(3-2x) \qquad (8A)$$

To determine the amount of each phase in the material, let M=mole fraction MgO, A=mole fraction Al_2O_3 and Z=mole fraction ZrO_2, where A+M+Z=1.00. For the Al_2O_3-rich eutectic. If there are C_S moles of $Mg_xAl_{2(1-x)}O_{3-2x}$ and C_Z moles of $Mg_yZr_{1-y}O_{2-y}$ and $C_S+C_Z=1$, and the relationship between x and y is:

$$y = \frac{M-(A+M)x}{1-A-x} \qquad (9A)$$

For the MgO-rich eutectic, the expression is more complicated because there are three instead of two phases. In this case there are C_S moles of $Mg_xAl_{2(1-x)}O_{3-2x}$, C_Z moles of $Mg_yZr_{1-y}O_{2-y}$ and C_M moles of MgO. Then,

$$y = \frac{M-C_M-x(A+M-C_M)}{Z+M-C_M+x(C_M-1)} \qquad (10A)$$

Substituting Eqs. (5A)-(10A) into Eq.(4A) leads to an expression of the density of the Al_2O_3-rich composition as a function of x, the mole fraction MgO in the spinel phase, and for the MgO-rich composition, as a function of x and C_M, the mole fraction MgO in the as-quenched material. Table 1A lists the parameters used in the expressions.

Parameter	*Value*
AW_{Zr}	91.22 gm/mol
AW_O	16.00 gm/mol
AW_{Mg}	24.31 gm/mol
AW_{Al}	26.98 gm/mol
P_k	1
P_{O_k}	1
$Z_{zirconia}$	4
Z_{spinel}	16
r_{Zr}	0.0824 nm
r_O	0.1400 nm
r_{Mg}	0.0648 nm
Al_2O_3-rich	
A	0.421 moles
M	0.174 moles
Z	0.405 moles
MgO-rich	
A	0.166 moles
M	0.421 moles
Z	0.413 moles

Table 1A. Parameters used in the equations to determine the density of the two phase mixtures in the Al_2O_3-MgO-ZrO_2 eutectics.

The densities for the materials were plotted and a polynominial regression was performed on the data. The functional representations are:

$$\rho_{Al\text{-}rich} = 5.3636 - 1.2118x + 2.7062x^2 - 6.2148x^3 \qquad R=1.00 \qquad (11A)$$

$$\rho_{Mg\text{-}rich} = 4.6433 + 0.9017x + 1.7065x^2 - 1.9495x^3 \qquad R=0.99,\ C_M = 0.17 \qquad (12A)$$

These densities are plotted in Figure 3.3 for both compositions. The density of the MgO-rich composition is plotted for C_M = 0.06-0.20, the practical limits for the mole fraction of MgO in the material. From the phase diagram in Figure 1.4(a), it is seen that the minimum to maximum solubility of MgO in c-ZrO_2 ranges from 0.13-0.22 at 2200°C. The minimum to maximum solubility of MgO in the spinel phase ranges from 0.5-0.6 at 2000°C, assuming that an Al_2O_3-rich spinel will not form in this system. For x=0.5 and y=0.13, C_M=0.20. For x=0.6 and y=0.22, C_M=0.06. A polynomial regression of order 3 was performed on the equation for C_M=0.17, the composition found in the as-quenched crystalline material.

REFERENCES

T. Ando, Y. Shiohara and M.C. Flemings, "Process Structure Relationships in Rapidly Solidified Al_2O_3-ZrO_2 Ceramics", Presented at the MRS Fall Meeting, Dec. 2-7, 1985, Boston, MA.

V.I. Aleksandrov, G.E. Val'yanc, B.V. Lukin, V.V. Osiko, A.E. Rautbort, V.M. Tatarintsev and V.N. Filatova, "Structure of Single Crystals of Stabilized Zirconium Oxide", *Izves.Akad.Nauk SSSr (Neorg.Mat.)*, **12**[2](1976)273-277.

A.M. Alper, R.N. McNally, P.H. Ribbe and R.C. Doman, "The System MgO-$MgAl_2O_4$", *J.Am.Ceram.Soc.*, **45**, 263-268 (1962)

J.C. Baker and J.W. Cahn, "Thermodynamics of Solidification" in Solidification, ASM, Metals Park, Ohio, 1971, 23-58.

B.A. Bender, R..P. Ingel and S.C. Semken, "Dependence of Eutectic Nanostructures on Cooling Rates", Ceramographic Exhibit, *Ceramics Abstracts*, **65** [1-2](1986).

A.S. Bierezhnoi and R.A. Kordyuk, "Melting of the System MgO-Al_2O_3-ZrO_2", *Dopovidi Akad. Nauk Ukr. RSR*, **4** 506-508 (1964).

D.P. Birnie and W.D. Kingery, "Quenching of Solid Samples for High Temperature Equilibrium Measurement", *J.Mater.Sci.*, **20**, 2193-2198 (1985).

W.J. Boettinger, "Growth Kinetic Limitations During Rapid Solidification", in Rapidly Solidified Amorphous and Crystalline Alloys, B.H. Kear, B.C. Giessen and M. Cohen, eds., Elsevier Science Publishing Co., Inc., New York, 1982, 15-31.

M.C. Brockway and R.R. Wills, "Rapid Solidification of Ceramics-A Technology Assessment", Metals and Ceramics Information Center Report, MCIC 84-49, Battelle Columbus Laboratories, Columbus, Ohio, 1984.

H.S. Chen and C.E. Miller, *Rev.Sci.Instrum.*, **41** (1970) 1237.

Y.-M. Chiang, "Grain Boundary Mobility and Segregation in Non-Stoichiometric Solid Solutions of Magesium Aluminate Spinel", Ph.D. Thesis, MIT, 1985.

Y.-M. Chiang and W.D. Kingery, "Grain Boundary Migration and Nonstiochiometry in Magnesium Aluminate Spinel: Part I, Measurements of Grain Growth and Grain Boundary Segregation", accepted *J.Am.Ceram.Soc.* (1988)

Y,-M. Chiang, personal communication, 1988.

N. Claussen and J. Jahn, "Tranformation of ZrO_2 Particles in a Ceramic Matrix", *Ber.Dtsch.Keram.Ges.*, **55**[11](1978)487-91.

N. Claussen, G. Lendemann and G. Petzow, "Rapid Solidification of Al_2O_3-ZrO_2 Ceramics", *Ceram.Int..*, **9**[3](1983)83-86.

G. Cliff and G.W. Lorimer, "Quantitative Analysis of Thin Metal Foils Using EMMA-4--The Ratio Technique", Proc. 5th European Congress on Electron Microscopy, The Institute of Physics, London, England, (1972) 140-143.

H.E. Cline, *Tran..Met.Soc.AIME*, **242**(1968)1613-1618.

T.W. Clyne and A. Garcia, "The Application of a New Solidification Heat Flow Model to Splat Cooling", *J.Mater.Sci.*, **16**, 1643-1653 (1981).

F.H. Cocks, J.T.A. Pollock and J.S. Bailey, in Conference of In Situ Composites, Vol. I, National Academy of Sciences, Washington D.C., 1974, Tech. Rept. No. NMAB-308, pp.141-52.

M.R. DeGuire, "Phase Equilibria and Rapid Solidification in the System CoO-Fe_2O_3-P_2O_5", Ph.D. Thesis, Deprtment of Materials Science and Engineering, MIT, February 1987.

C. Delamarre, "Existance and Structure of a New Compound of Formula M_7O_{12} in Zirconia-Magnesia and Hafnia-Magnesia Systems" *C.R. Hebd.Seances AcadSci.Ser.C.*, **269** 113-15 (1965)

W.H. Dumbaugh, "Infared Transmitting Glasses", *Op.Eng.*, **24**[2](1985)257-262.

P. Duwez, R.H. Willens and W. Klement, *J.Appl.Phys.*, **31**, 1960, 1136.

P. Duwez, *Trans.Am.Soc.Met.*, **60**, 1967, 607.

J. Echigoya, Y. Takabayashi, K. Sasaki, S. Hayashi and H. Suto, "Solidification Microstructure of Y_2O_3-Added Al_2O_3-ZrO_2 Eutectic", *Trans.Jap.Inst.Met.*, **27**[2](1986)102-107.

A.G. Evans and A.H. Heuer, "Transformation Toughening in Ceramics: Martensitic Transformations in Crack-Tip Stress Fields", *J.Am.Ceram.Soc.*, **63**[5-6](1980)241-48.

M. Foex, F. Sibieude, A. Rouanet and D. Hernandez, *J.Mater.Sci.*, **10**, 1255 (1975)

B. Frank and J. Liebertz, *Glastechn.Ber.*, **41** (1968) 253.

R.H. French, "Electronic Structure of Al_2O_3: VUV Reflectivity Measurements from Room Temperature to 1100°C", Ph.D. Thesis, Department of Materails Science and Engineering, MIT, February 1985.

R.C. Garvie, *J.Phys.Chem.*, **69**[4](1965)1238-43.

G.H. Geiger and C.R. Poirier, Transport Phenomena in Metallurgy, Addison-Wesley, Reading, Mass., p.292, 1973.

S. Geislinger, "Determination of Microstructural Effects on Dielectric Constant in Rapidly Solidified $KNbO_3$", B.S. Thesis, Department of Materials Science and Engineering, MIT, June 1987.

E.A. Gómez, "Rapid Solidification of Spinel Ferrites", B.S. Thesis, Department of Materials Science and Engineering, MIT, June 1987.

C.F. Grain, "Phase Relations in the ZrO_2-MgO System", *J.Am.Ceram.Soc.*, **50** 288-90 (1967)

K.F.J. Heinrich, "X-Ray Adsorption Uncertainty", in The Electron Microprobe, eds. McKinely, Heinrich, Wittrey, Wiley, New York, 1966, 296-377.

A. Heuer,"Alloy Design in Partially Stabilized Zirconia", Advances in Ceramics, Vol. 3, eds. A. Heuer, and L.W. Hobbs, American Ceramic Society, 1981, 98-115.

S.M. Ho, "On the Structural Chemistry of Zirconium Oxide", *Mater.Sci.Eng.*, **54**[1](1982) 23–29.

J.D. Hunt and K.A. Jackson, "Binary Eutectic Solidification", *Trans. AIME*, **230** 843-52 (1966).

R.P. Ingel and D. Lewis, "Lattice Parameters and Density for Y_2O_3-Stabilized ZrO_2", *J.Am.Ceram.Soc.*, **69**[4](1986)325-332.

C.M. Jantzen, R.P. Krepski and H. Herman, "Ultra-Rapid Quenching of Laser-Melted Binary and Unary Oxides", *Mater.Res.Bull.*, **15**(1980)1313-1326.

A. Krauth and H. Meyer, "Chilling Codifications and Crystal Growth in Zirconia Systems", *Ber.Deut.Keram.Ges.*, **42**(1965)61-72.

R. Krepski, M.S. Thesis (1975) SUNY at Stoney Brook.

W. Kurz and D.J. Fisher, Fundamental of Solidification, Trans Tech Publications LTD, Switzerland, 1986, 97-107.

F. F. Lange and D.J. Green, "Effect of Inclusion Size on the Retention of Tetragonal ZrO_2: Theory and Experiment", in Advances in Ceramics, Vol. 3, eds. A. Heuer and L. Hobbs, Science and Technology of Zirconia, American Ceramic Society (1981) 217-225.

E.M. Levin and H.F. McMurdie, eds., Phase Diagrams for Ceramists, Vol. 3, American Ceramics Society, 1975, pp. 135-136.

R. Linder and A. Akerstroem, "Diffusion von Ni-63 in Nickelspinellen', *Z.Phusik.Chem.N.F.*, **18** 303-307 (1958)

W.C. Mackrodt and P.M. Woodrow, "Theoretical Estimates of Point Defect Energies in Cubic Zirconia", *J.Am.Ceram.Soc.*, **69**, 277-280 (1986).

W.J. Minford, R.C. Bradt, and V.S. Stubican, "Crystallography and Microstructure of Directionally Solidified Oxide Eutectics", *J.Am.Ceram.Soc..*, **62**[2-3](1979)154-157.

T. Mitsuhashi, M. Ichihara and U. Tatsuke, "Characterization and Stabilization of Metastable Tetragonal ZrO_2", *J.Am.Ceram.Soc.*, **57**[2](1974)97-101.

M. Nogami and M. Tomozawa, "ZrO_2-Transformation-Toughened Glass Ceramics Prepared by the Sol-Gel Process from Metal Alkoxides" *J. Am. Cer. Soc.*, **69**, 99-102 (1986).

P.C. Panda and R. Raj, "Kinetics of Precipitation of α-Al_2O_3 in Polycrystalline Supersaturated $MgO{\cdot}2Al_2O_3$ Spinel Solid Solution", *J.Am.Ceram.Soc.*, b69(1986)365-373.

S.C. Peterson, "Gas Atomization of Al_2O_3-ZrO_2 Eutectic Material: A Rapid Soldidification Process", M.S. Thesis, Department of Materials Science and Engineering, MIT, June 1987.

J. Philibert and R. Tixier, *J.Phys.D*, **1**(1968)685.

A.C. Pierre, "Ceramic Composites by Sol-Gel Techniques", Ph.D. Thesis, Department of

Materials Science and Engineering, MIT, Cambridge, Mass., USA, 1985.

M.J. Readey, A.H. Heuer and R.W. Steinbrech, "Annealing of Test Specimens of High-Toughness Magnesia-Partially-Stabilized Zirconia", *Comm.Am.Ceram.Soc.*, **71** [1] C2-C6 (1988).

A. Revcolevski, "Cooling Rates from Growth Rates", *J.Mater.Sci.*, **11**(1976)563.

A. Revcolevschi and J. Livage, "Rapid Solidification of Nonmetals", in Treatise on Materials Science and Technology, Vol. 20, ed. H. Herman, Academic Press, New York, 1981, 73-116.

A. Revcolevski, A. Rouanet, F. Sibieude and T. Suzuki, "Techniques for Ultrafast Quenching (Splat Cooling) of Refractory Oxides", *H.Temp.H.Press.*, **7**(1975)209-214.

H.P. Rooksby, "The Preparation of Crystalline δ-Al_2O_3", *J. Appl. Chem.*, **8** (1958) 35-49.

H.J. Rossell and R.H.J. Hannink, "The Phase $Mg_2Zr_5O_{12}$ in MgO Partially Stabilized Zirconia", p.136-151 in Advances in Ceramics, Vol. 12, Eds. N. Claussen, M. Rühle and A.H. Heuer, The American Ceramic Society, Columbus, OH, 1984.

D.M. Roy, R. Roy and E.F. Osborn, *J.Am.Ceram.Soc.*, **36** 149 (1953).

R.C. Ruhl, "Cooling Rates in Splat Cooling", *Mater.Sci.Eng.*, **1**, 313-320 (1967).

H. Saalfeld and H. Jagodzinski, *Z.Kristallogr.*, **109**(1957)87.

P.T. Sarjeant and R. Roy, "New Glassy and Polymorphic Oxide Phases Using Rapid Quenching Techniques", J.Am.Ceram.Soc., **50** [10], 500-503.

P.T. Sarjeant and R. Roy, R., *J.Appl.Phys.*, **38**, 4540.

P.T. Sarjeant and R. Roy, "Splat-Quenched Melts in the MgO-Al_2O_3 System", *Comm.Am.Ceram.Soc.*, (1967)4540-4542.

J. Selsing, "Internal Stresses in Ceramics", *J.Am.Ceram.Soc.*, **44**[8] 419 (1961)

H.G. Scott, "Phase Relationships in the Zirconia-Yttria System", *J.Mater.Sci.*, **10**(1975)703-704.

F. Schmid and D. Viechnicki, "Oriented Eutectic Microstructures in the System Al_2O_3/ZrO_2", *J.Mater.Sci.*, **5**(1970)470-473.

S.M. Sim and V. Stubican, "Phase Relations and Ordering in the System ZrO_2-MgO", *J.Am.Ceram.Soc.*, **70**, 521-526 (1987)

D.K. Smith and H.W. Newkirk, "Crystal Structure of Baddeleyite (Monoclinic Zirconia) and its Relation to the Polymorphism of ZrO_2", *Acta.Cryst.*, **18**, 983-991 (1965)

W.H. Strehlow and E.L. Cook, "Compilation of Energy Band Gaps in Elemental and Binary Compound Semiconductors and Insulators", *J.Phys.Chem.Ref.Data*, **2** [1] 183-199 (1973)

T. Suzuki and A.-M. Anthony, "Rapid Quenching on the Binary Systems of High Temperature Oxides", *Mater.Res.Bull.*, **9**(1974)745-754.

T. Suzuki, S. Saito and W. Arakawa, *J.Non-Cryst.Sol.*, **24** (1977) 355.

L.E. Topol, D.H. Hengstenberg, M. Blander, R.A. Happe, N.L. Richardson and L.S. Nelson, "Formation of New Oside Glasses by Laser Spin Melting and Free Fall Cooling", *J.Non-Cryst.Sol.*, **12**(1973)337-390.

W.D. Tuohig and T.Y. Tien, "Subsolidus Phase Equilibria in the System ZrO_2-Y_2O_3-Al_2O_3", *J.Am.Ceram.Soc.*, **63**[1](1980)595-596.

V. Wilms and H. Herman, "Plasma Spraying of Al_2O_3 and Al_2O_3-Y_2O_3", *This Solid Films*, **39**(1976)251-262.

G.M. Wolten, "Direct High-Temperature Single-Crystal Observation of Orientation Relationship in Zirconia Phase Transformation", *Acta.Cryst.*, **17**, 763-765 (1964)

N.J. Zaluzec, "Quantitative X-Ray Microanalysis", in Introduction to Analytical Electron Microscopy, Chapter 4, ed. J.J. Hren, J.I. Goldstein and D.C. Joy, Plenum Press, New York, (1979) 121-167.

PART II. RAPID SOLIDIFICATION OF OXIDE SUPERCONDUCTORS

TABLE OF CONTENTS

LIST OF FIGURES

LIST OF TABLES

1.0 INTRODUCTION

1.1 Overview of Oxide Superconductors

1.1.1 Historical Perspective

Superconductivity was first demonstrated by H.K. Onnes in 1911 when zero electrical resistivity was found in mercury at 4.2 K, the superconducting transition temperature, T_c. Subsequently, the discovery of materials with higher T_c values has increased with a rate of about 4 K per decade. The first reports of superconductivity in an oxide were for $SrTiO_3$ in 1964 by Schooley et al. which had a T_c <1 K. Interest was generated by these findings to further examine oxide materials, and superconductivity was found in $LiTiO_3$ [Johnson, et al. (1973)] with a T_c at 13 K and in $Pb_{1-x}Bi_xBaO_3$ at 14 K [Sleight et al. (1975)].

In 1986 Bednorz and Müller suggested and later confirmed (1987) superconductivity at 30 K in a mixed oxide phase Ba-La-Cu-O. The intense search for higher T_c materials that followed lead Wu et.al. (1986) and Chu et al. (1987) in the US to discover superconductivity in the Y-Ba-Cu-O system at 92 K, and their results were confirmed independently at the Institute of Physics in Beijing [Zhao et al. (1987)] and the Indian Institute of Science, Banglalore [Ganguly et al. (1987)]. Within days, the superconducting compound was identified separately by several groups [Gallagher et al. (1987), Grant et al. (1987), Tarascon et al. (1987) and Cava et al. (1987)] to be $YBa_2Cu_3O_{9-x}$. Based on the work on the structure of defective perovskites by Michel and Raveau (1984) and Er-Rakho et al. (1981), a better description of the compound is $YBa_2Cu_3O_{7-x}$ where the stoichiometric superconducting phase is $YBa_2Cu_3O_7$.

Subsequent work by thousands of research groups around the world in the past year has elucidated the crystallography, phase relationships, microstructural features, and magnetic and electric properties. However, the field is far from saturated in that there are still unanswered questions as to optimal processing techniques, understanding the phase relationships, and especially in formulating a basic theory of these superconductors. The possibility of other high T_c oxide superconductors had lead to investigations into other compounds. Recently, superconductivity has been discovered in systems comprised of Bi-Sr-Ca-Cu-O and Tl-Ba-Ca-Cu-O[Chu et al. (1988), Zhao et al. (1988) and Sleight et al. (1988)], both of which display a T_c between 110-120 K, higher than that of $YBa_2Cu_3O_{7-x}$.

The discovery of the new classes of high temperature oxide superconductors offers a tremendous challenge to the materials science community. It is the responsibility of the ceramics community to develop viable processing routes to optimize the engineering properties. Rapid solidification may prove to be a valuable processing route for ceramic superconductors as it can provide great flexibility for microstructural control of ceramics in general, and for these exciting new materials in particular. This enhanced microstructural control can be expected to be beneficial by the factors outlined in Part I. Firstly, there exists the possibility of enhancing engineering properties through chemical homogeneity and greatly extended solid solubilities, through the generation of very fine grained microstructures, and through the ability to quench in a variety of metastable phases. Secondly, the ability to generate novel microstructures, which may be inaccessible by other processing routes, can lead to new scientific insights into fundamental aspects of the superconducting properties of these systems. Examples might include quenching in metastable cation distributions, or high temperature degrees of disorder among of oxygen vacancies, and investigating the effect of these phenomena on properties.

The goals of this research were to melt and rapidly solidify various compositions in the M-Ba-Cu-O (M=Y, Eu, Gd) system in order to achieve the above mentioned properties. The solidification techniques reported in Part I were successfully used to quench high temperature melts into an amorphous form and it seemed reasonable to assume that some of the techniques could be used successfully on the superconductors. It was desired to obtain metastable high temperature phases, both crystalline and amorphous, and examine these for any superconducting behavior via electric and magnetic measurements. It was also of interest to examine the microstructural and phase developmental route the materials took in approaching equilibrium.

1.1.2 Crystallography

The crystal structure (space group Pmmm) of the orthorhombic $YBa_2Cu_3O_7$ (Y-1:2:3) is shown in Figure 1.0. It is an oxygen deficient, triple perovskite consisting of Cu atoms on the corner of the cells, Ba ions in the center of the top and bottom cells and a Y ion in the center of the middle cell. The O ions sit on the edges of the cells. The oxygen deficiency is manifested in two ordered arrays, one planar and one linear, in order to leave 2 vacancies/cell. The Y-plane contains no oxygen, accounting for one of the vacancies at

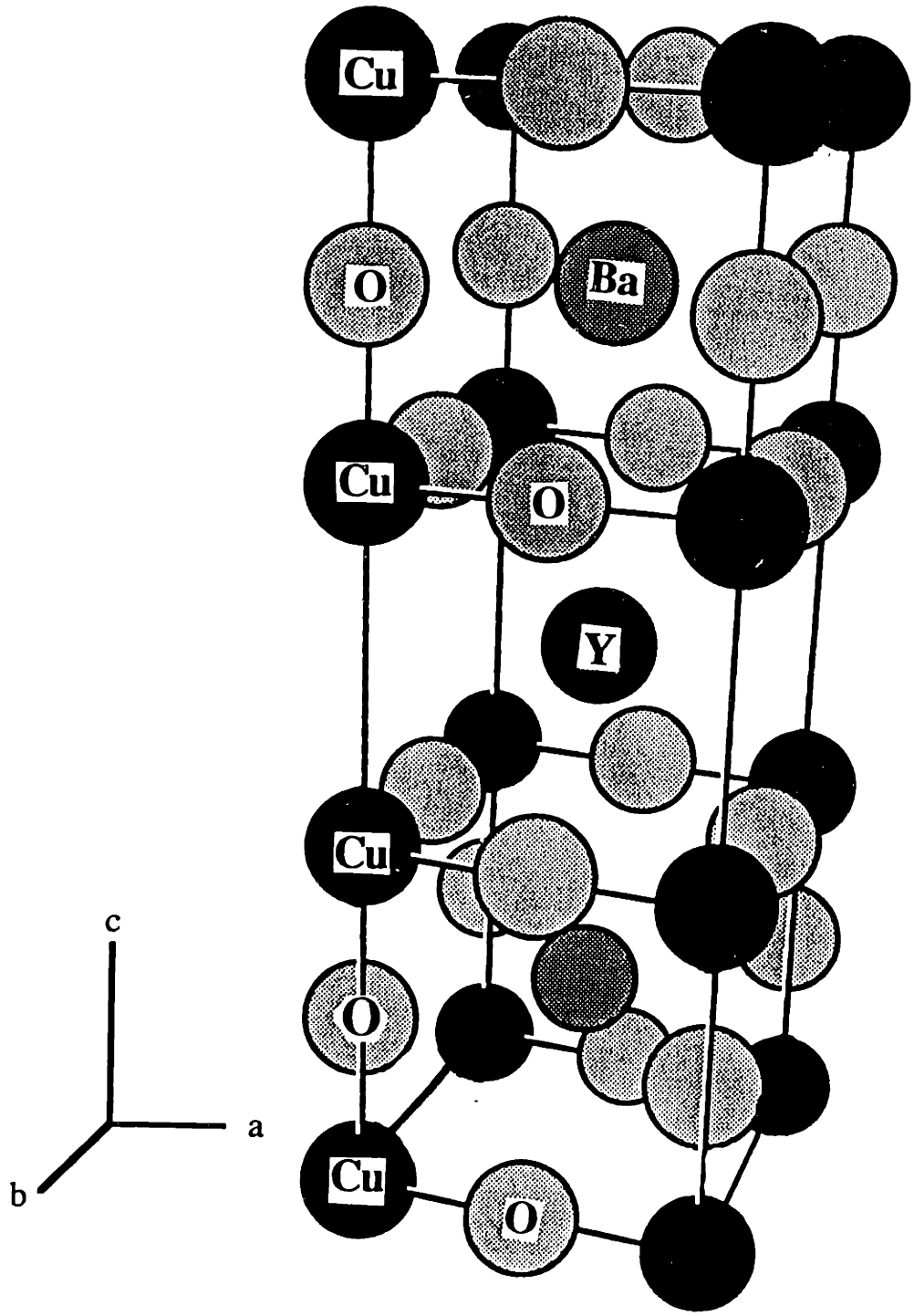

Figure 1.0
Crystal structure of $YBa_2Cu_3O_{7-x}$. From Siegrist et al. (1987).
a=0.3827 nm, b=0.3893 nm and c=1.1699 nm.

(0,0,1/2). The other vacancy is on the z=0 plane. It is ordered along the a-axis at (1/2,0,0) and forms one dimensional chains parallel to the b-axis.

Atom	Wyckoff Symbol	x/a	y/b	z/c
Y	1h	1/2	1/2	1/2
Ba	2t	1/2	1/2	0.1850(2)
Cu(1)	1a	0	0	0
Cu(2)	2q	0	0	0.3565(5)
O(1)	1e	0	1/2	0
O(2)	2q	0	0	0.1566(23)
O(3)	2s	1/2	0	0.3776(21)
O(4)	2r	0	1/2	0.3765(21)
O(5)*	1b	1/2	0	0

Table 1.0. Crystallographic data for $YBa_2Cu_3O_7$ [Calestani and Rizzoli (1987)]. a=0.3827(1), b=0.3893(1), c=1.1699(2) nm. * This position is not occupied by oxygen in the orthorhombic structure.

The Cu(1) ions on the basal planes are coordinated by 4 oxygens in a square planar array on the b-c plane. The Cu(2) ions are 5-fold coordinated in a square pyramidal arrangement. The planar oxygens on the a-b plane [Cu(1)] have bond lengths significantly shorter (0.193-0.196 nm) than the apical one [Cu(2) with 0.234 nm] and the structure can therefore be regarded as puckered sheets of CuO_4 parallel to the a-b plane which weakly interact with the one dimensional O(2) chains along the c-axis.

The $YBa_2Cu_3O_7$ compound can be written as $(YO_{1.5})\cdot(2BaO)\cdot(3.5Cu_{0.857}O)$ corresponding to an average Cu valence state of +2.333, a mixture of Cu^{+2} and Cu^{+3}. Based on bond strength calculations, David et al. (1987) have proposed that since the bond lengths for the Cu(1)-O(2) are unexpectedly short, the Cu^{+3} ions occupy that position.

The oxidation state of $YBa_2Cu_3O_{7-x}$ can vary between x=1 to x=0 during thermal processing of the compound. At temperatures ~1010°C, x=1 and the structure is tetragonal with space group P4/mmm, with a=0.38578 and b=1.18391 nm [Wong-Ng et al. (1987)]. This compound is semiconducting under ambient conditions and is not superconducting, at least at T.30 K.. The oxygen is completely removed from the basal plane so that the O(1) in the 1e position is absent. This phase can be obtained by annealing in Ar or by rapidly

cooling the sample from high temperatures. The compound can be written as $(YO_{1.5})\cdot(2BaO)\cdot(2.5Cu_{1.2}O)$ which corresponds to an average Cu valence state of 1.67, a mixture of Cu^{+2} and Cu^{+1}.

The tetragonal to orthorhombic (t->o) transition is a first order transformation as indicated by the exothermic reaction seen in DSC traces from heating the tetragonal phase in O_2 by Gallagher (1987). From the thermogravimetric analyses performed by several research groups [Behrman et al. (1987), Strobel et al. (1987)] it was found that the o-1:2:3 samples heated from room temperature gradually lose weight from ~500°C up to ~950°C, a process which is reversible upon cooling. The presence of the tetragonal phase will debilitate the optimal superconducting properties of the Y-1:2:3 material by lowering the T_c and widening the transition gap, ΔT_g, the difference in temperature between the onset of superconductivity and the temperature where zero resistance is attained. However, there is a caveat in assuming that the orthorhombic phase will always exhibit desirable superconducting properties. The T_c is dependent not only on the stoichiometry, but on the degree of ordering of the oxygen vacancies in the basal plane.

The tetragonal structure can be maintained for $x<1$ if the oxygen occupancy in the 1e position, n_{1e}, is equal to n_{1b}, the oxygen occupancy in the 1b position. And $n_{1e}=n_{1b}=0$ for the ideal tetragonal structure. As the oxygen content in the sample is raised, the vacancies on the (001) plane begin to order along [010]. Figure 1.1 shows transition temperature, the temperature where the resistivity begins to drop as the temperature is lowered, as a function of oxygen stoichiometry in Y-1:2:3 [Cava et al. (1988)]. As shown, the transition temperature drops slightly for $0<x<0.2$ and then decreases precipitously for $x>0.2$, levels out at a transition temperature of 60K for $0.3<x<0.5$ and then drops to ~20 K for $x=0.5$.

The t->o transition is a function of oxygen partial pressure and temperature. O'Bryan and Gallagher (1987) have reported that the t->o transition is only a function of oxygen stoichiometry and occurs at $x=0.37\pm0.03$ for $YBa_2Cu_3O_{7-x}$. They found that the transition temperature decreases as p_{O_2} decreases. The transition temperature was 686°C in pure O_2 and 520°C in 0.09% O_2. They also report that there is a 0.2% volume change for the o->t transformation. Steinfink et al. (1987) report that the orthorhombic phase is stable between $0\leq x\leq0.4$, the tetragonal phase is stable between $0.88\leq x\leq1$, and a mixture of orthorhombic and tetragonal phases co-exist between $0.4<x<0.88$. Beyers et al. (1988) report that the orthorhombic phase can be maintained for $x\leq0.7$. The discrepancies in the data are thought to be related to the degree of vacancy ordering on the 1e and 1b sites,

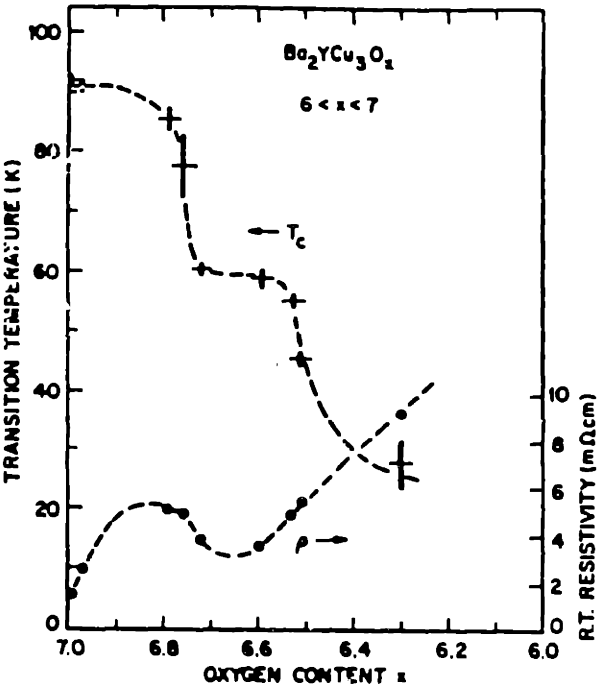

Figure 1.1
Transition temperature as a function of O_2 stoichiometry for $YBa_2Cu_3O_{7-x}$. From Cava et al. (1988).

according to Cava et al. (1988). If oxygen is removed slowly and the sample remains in equilibrium, the orthorhombic structure can be stable for high values of x whereas if the oxygen is removed rapidly, the orthorhombic to tetragonal transformation occurs at lower values of x. Thus, processing dictates the oxygen stoichiometry at which the transformation takes place. To obtain the optimal stoichiometry of x=1, it is necessary to cool the sample from the processing temperature at a slow rate, on the order of a few degrees per minute.

1.1.3 Phase Relationships

Figure 1.2 shows the phase diagram for the BaO-$YO_{1.5}$-CuO_x ternary system combined from data of Roth et al. (1987) and Frase and Clarke (1987). It is recognized that the valence state of the Cu ion can range from +1-+3 in this phase diagram. The diagram shows the compatibility triangles, regions of partial melting in the temperature range of 950-1000°C and the primary phase field of $YBa_2Cu_3O_7$. Hwu et al. (1987) and McCallum et al. (1987) have determined similar phase diagrams. Three ternary compositions have been identified in the system: $YBa_2Cu_3O_7$, Y_2BaCuO_5 and $YBa_3Cu_2O_{6.5}$. $YBa_2Cu_3O_7$ is the only superconducting compound found, the others are semiconducting. Table lists the structures of these interior compounds.

Not much work has been done on determining the phase diagrams of $EuO_{1.5}$-BaO-CuO and $GdO_{1.5}$-BaO-CuO. It has been shown by Hor et al. (1987) that the Eu and Gd compounds have the same structure as the Y compound and similar T_c's. It is reasonable to expect that the melting and solidification behavior and phase compatibility in these systems will be analogs.

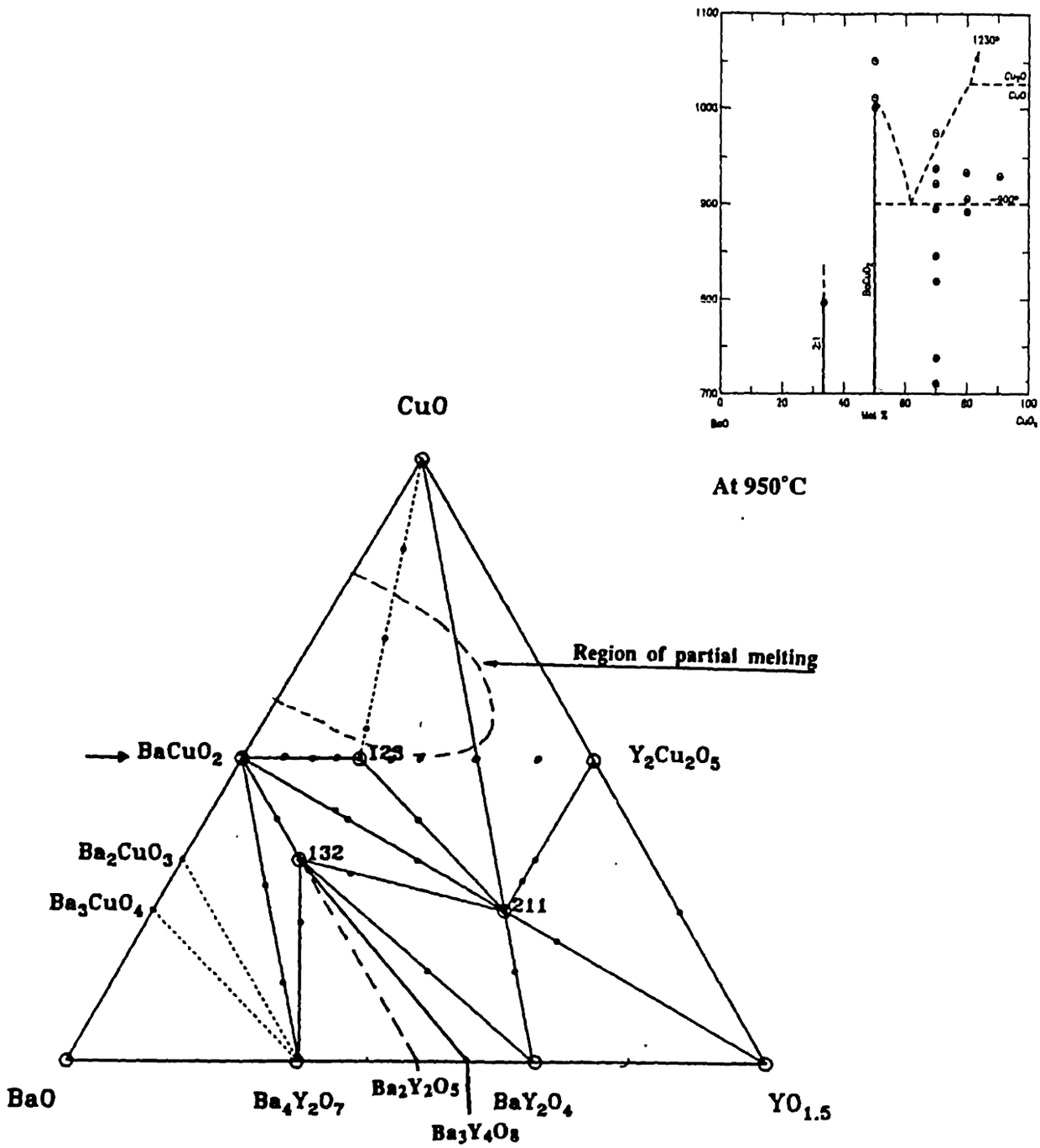

Figure 1.2
Ternary phase diagram for BaO-$YO_{1.5}$-CuO_x. From Roth et al. (1987) and Frase et al. (1987). Binary $BaCuO_2$-CuO_2 system is also included from Roth et al. (1987).

Composition	*Crystal Structure*	*Lattice Parameters (nm)*
$YBa_2Cu_3O_7$	Pmmm (orthorhombic)	a=0.3827, b=0.3893, c=0.11699†
$YBa_3Cu_2O_{6.5}$	P4mm (tetragonal)*	a=0.5866, c=0.8000
Y_2BaCuO_5	Pbnm (orthorhombic)	a=0.71319, b=0.121802, c=0.56593

Table 1.1. Crystallography of the three ternary compounds found in the BaO-$YO_{1.5}$-CuO phase diagram. [Roth et al. (1987)]
† from Calestani and Rizzoli (1987)
* This compound appears to be a high temperature ordered phase.

Frase and Clarke (1987) also identified two binary BaO-CuO compositions, Ba_2CuO_3 and Ba_3CuO_4 which are included in Figure 1.2 along with the compatibility joins found to other compositions. The aforementioned compounds were found to be hygroscopic and decomposed under ambient conditions. The $BaCuO_2$-CuO_x phase equilibria is of interest as the eutectic reaction between the two compounds has been observed upon heating and cooling the $YBa_2Cu_3O_7$ compound [McCallum et al. (1987)]. This binary is shown in Figure 1.1 as determined by Roth et al.(1987). The eutectic temperature is 900°C, the eutectic composition is 24.4 mol% $BaCuO_2$-75.6 mol% CuO_x, the melting point of $BaCuO_2$ is 1020°C, the CuO->Cu_2O transition occurs at 1025°C and the melting point of CuO_x is 1230°C. McCallum et al. (1987) report a slightly different phase diagram. They report that the eutectic temperature is 890°C, the melting point of $BaCuO_2$ is 970°C and the melting point of CuO_x is 1092°C.

Tie-lines are found to extend from $YBa_2Cu_3O_7$ to $BaCuO_{2+x}$, Y_2BaCuO_5, and CuO_x. $YBa_2Cu_3O_7$ is a peritectic composition and melts incongruently. Its primary phase field is on the BaO and CuO rich portion of the phase diagram.

1.2 Magnetic Properties

If a superconductor is cooled below its transition temperature in the presence of a weak magnetic field ($H<H_{c_1}$), the material sets up small eddy currents on the surface opposing the applied magnetic field. The net flux inside the superconductor is zero, thus

$$B=\mu_o(H+4\pi M)=0 \qquad (1.0)$$

B is the magnetic flux, H is the applied magnetic field and M is the magnetic dipole moment per unit volume (magnetization), and $M=\chi_m H$ where χ_m is the magnetic susceptibility. For this condition, $\chi_m=-1/(4\pi)$, which means that a superconductor cooled below its transition temperature in a weak magnetic field is a perfect diamagnet. This flux exclusion is called the Meissner effect. In another path, if a superconductor is cooled below its transition point in zero field and a weak magnetic field is then applied, the flux is also excluded from the interior. This is called the shielding condition. In the Meissner effect, flux is expelled as the temperature is decreased below T_c; in shielding, the flux is prevented from entering when the field is turned on for temperatures greater then T_c.

2.0 EXPERIMENTAL TECHNIQUES

2.1 Rapid Solidification Techniques

Pellets of material were prepared by weighing the desired amount of $BaCO_3$, CuO and M_2O_3 (M=Y, Eu, Gd), grinding first with a mortar and pestle and then in a ball mill overnight with ZrO_2 grinding media. The powder was placed in Al_2O_3 crucibles and calcined at 950°C for 16 hours in air. The powders were re-ground and sieved to 106 μm, cold pressed under $22x10^3$ kg into 1.27 cm diameter, 4 cm long pellets. The pellets were sintered in flowing O_2 at 950°C for 5 hours and cooled at 3°C/min to 300°C and removed from the furnace. Table 2.0 lists the starting powders and their purity levels.

Powder	Purity	Major Contaminants	Supplier
$BaCO_3$	99.999	Sr, Ca, Mg	Cerac
CuO	99.999	Al, Ca, Co, Fe, Mg, Si	Cerac
Y_2O_3	99.99	Yb, Er, Sm, Ca	Cerac
Eu_2O_3	99.999	Yb, Er, Sm, Ca	Cerac
Gd_2O_3	99.999	Yb, Er, Sm, Ca	Cerac

Table 2.0 Starting powders and their purity levels.

The single phase, orthorhombic 1:2:3 was verified to be the composition of the pellets by x-ray diffraction before attempting further work. The first heating experiment was done by trying to couple an RF field directly to the material without the use of a susceptor. Although the Y-1:2:3 composition became warm, it did not melt. The second attempt was to couple the RF field to a graphite susceptor and heat the material through convective heating. The material did melt but was extremely reduced. The flakes obtained were black with streaks of pure copper metal. X-ray diffraction revealed that Cu and $BaCuO_2$ were present along with other unidentified compounds.The experiment was run in air but the oxidation of the graphite susceptor was severe enough to absorb oxygen from the material. With these failures in mind it seemed necessary to provide an oxygen rich environment when melting the material. The obvious choice was to employ an O_2 gas torch with an O_2-rich flame.

The pellets were melted using an H_2-O_2 torch with an O_2 rich flame and solidified with three different techniques which yielded estimated cooling rates from ~300 K/sec to ~10^7 K/sec. For estimated cooling rates of 300 K/sec, the melt-drop technique was used. In this technique, a sintered rod is suspended approximately 8 cm above a copper block. A droplet is melted on the end of the rod with the torch and allowed to fall under its own weight to the copper substrate.

The melt extraction technique was also used to rapidly solidify the material. This technique has been described in Part I. The cooling rate for this technique ranges from 10^4-10^6 K/sec, depending on the thickness of the flakes.

The twin roller device was used to solidify the melt at faster quench rates with dual H_2-O_2 torches, shown in Figure 2.0. As pointed in Part I, twin rolling produces faster quench rates than melt extraction, on the order of 10^5-10^7 K/sec. For all three techniques, 10-15 gms of the material were melted and solidified.

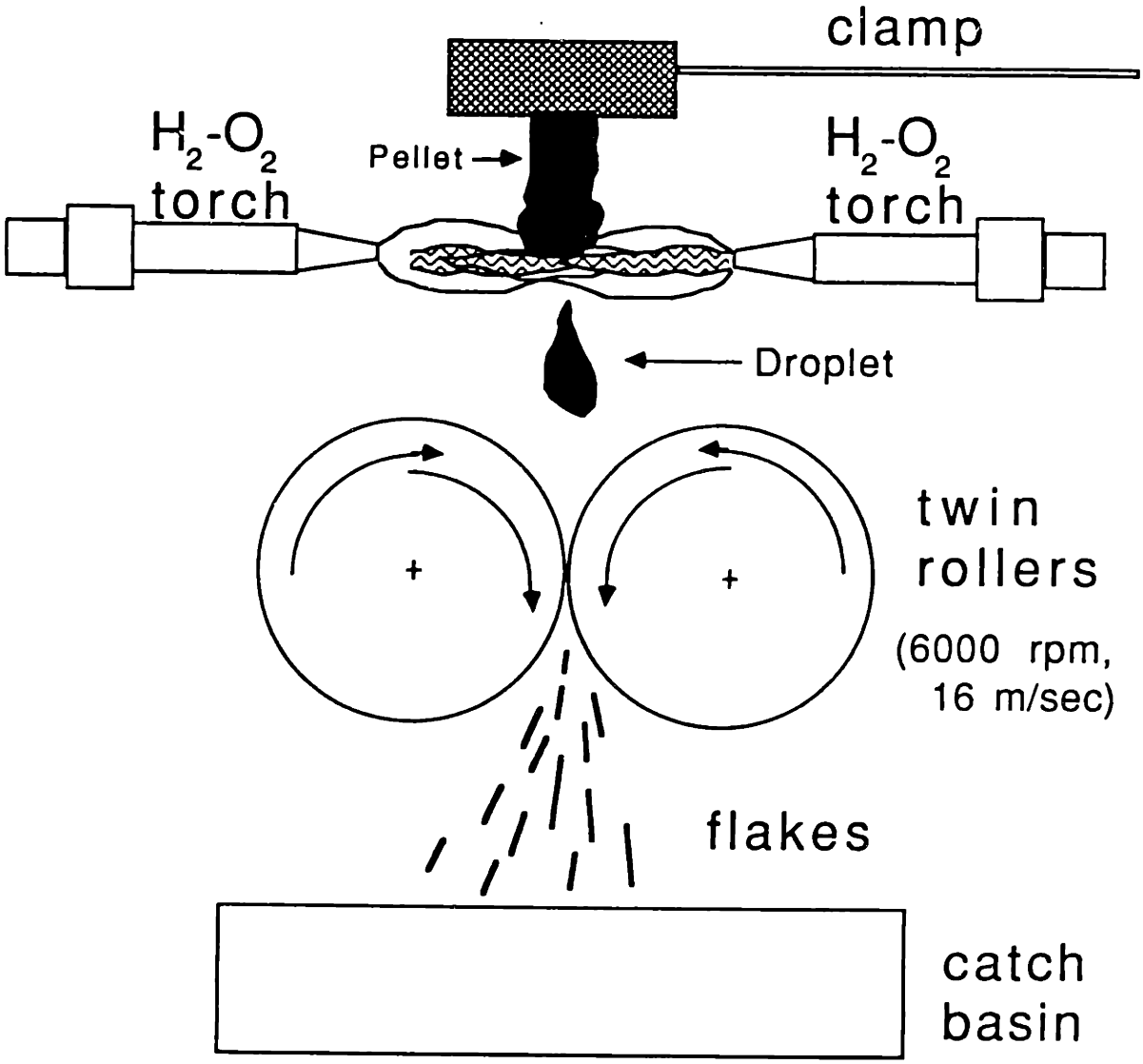

Figure 2.0
Schematic diagram of the rapid solidification technique used with the dual torches and twin roller quenching device.

2.2 Analytical Techniques

The analytical devices used in this part of the work are the same as the ones employed in Part I, and the reader should refer to that section for the manufacturers name and location. The as-quenched and annealed materials were examined with a powder x-ray diffraction unit. Annealing was performed in flowing O_2 at 6 cm^3/min at various temperatures up to 950°C. DTA was performed on the as-quenched flakes in flowing O_2 at a heating and cooling rate of 10°C/min with an Al_2O_3 reference in Pt cups. Fresh samples were annealed for 10 min. at temperatures between the exothermic and endothermic reactions found from the DTA traces and then analyzed by x-ray diffraction.

SEM analysis was performed on a Cambridge[1] equipped with EDS[2] analysis. Both the as-quenched and the heat treated materials of the 1:2:3 composition were polished in oil to 3 μm with diamond paste and etched in a 30% $FeCl_2$-70% CH_3OH solution. Flakes of the twin-rolled material in the as-quenched and annealed condition were thinned on a liquid nitrogen cold stage in an ion mill for periods of 6-12 hours at 6 KeV and 1.5 mA. The thinned materials were examined with a TEM and with a STEM equipped with microdiffraction and chemical analytical capabilities. The as-quenched and annealed materials were crushed and pressed into pellets for electrical and magnetic measurements. DC resistivity vs.temperature (or temperature and magnetic field) measurements were made by a four probe technique with the leads attached by silver paint. Magnetic measurements were performed at the Francis Bitter National Magnet Laboratory in a commercial SQUID magnetometer. Susceptibility data were taken by cooling to 10 K in a zero field and then heating in a field of 100 Oe (ZFC) and then cooling down in that field (FC). Magnetic relaxation data were taken in the zero field cooled state. The magnetic field was applied after stabilizing at the desired temperature and relaxation data were taken after one minute elapsed.

---

[1] Cambridge Instruments Ltd., Rustat Rd., Cambridge, CB13QH, England.

[2] Tracor Northern, 2551 W. Beltline Hwy., Middleton, WI 53562

3.0 EXPERIMENTAL RESULTS AND DISCUSSION

3.1 Materials Systems Examined

Several compositions in the Y-Ba-Cu-O system were examined along with $EuBa_2Cu_3O_{7-x}$ and $GdBa_2Cu_3O_{7-x}$. Compositions along the 1:2:3-$BaCuO_2$ tie-line were prepared which are listed in Table.3.0. Strontium oxide was added to several compositions as it falls directly above Ba in the periodic table and would be a likely candidate for substitution in this system. Hosoya et al. (1987) and Hor et al. (1987) have found that most of the lanthanide series can be substituted for yttrium and the 1:2:3 phase remains superconducting. The oxides Eu_2O_3 and Gd_2O_3 were chosen to examine the influence of high magnetic moments on superconducting properties.

Composition (molar ratios)	Y_2O_3	Eu_2O_3	Gd_2O_3	BaO	CuO
1:2:3	1			2	3
1:2.5:3.5	1			2.5	3.5
1:3:4	1			3	4
1:2:3		1		2	3
1:2:3			1	2	3

Table 3.0 Compositions examined in the Y-Ba-Cu-O, Eu-Ba-Cu-O and Gd-Ba-Cu-O systems.

3.2 Solidified Material Geometry

For the melt dropped samples, the solidified material was glossy black in appearance and disk shaped with a diameter of 0.20-0.75 cm and 0.05-0.30 cm in thickness. The melt extracted flakes were also glossy black and measured a few millimeters in length and width and about 400 μm in thickness. For the twin rolled samples, the materials were in the form of flakes, some as large as 3 cm in length, 2 cm in width and 40-100 μm in thickness. These flakes were also glossy black in appearance, but on prolonged exposure to air turned orange. If placed in liquid N_2, the materials turned turquoise blue-green in color, which indicated the presence of reduced cuprous oxide, Cu_2O.

3.3 X-Ray Diffraction Results

The Debye-Scherrer x-ray diffraction results for 30 μm thick twin rolled Y-1:2:3 composition is shown in Table 3.1. The x-ray pattern exhibits the presence of amorphous material as well as crystalline peaks, as shown in Figure 3.1(a). The crystalline peaks could not be indexed to any known compounds in the BaO-$YO_{1.5}$-CuO system, however, they could be indexed to a cubic cell with lattice parameter 0.701 nm. A few weak lines could not be indexed to this lattice structure. The flakes could not be easily separated or broken into samples which contained completely amorphous regions and ones with microcrystalline regions as they were not visually transparent. The best way is to separate them by thickness and only the thinnest flakes (<30 μm) were used for the x-ray analysis.

The cubic structure was also found in the more slowly cooled samples from the melt extraction and melt drop techniques, as shown in Table 3.2. For these techniques, $BaCuO_2$ (0:1:1) and Y_2BaCuO_5 (2:1:1) were also found with the cubic phase. This phase assemblage was also found for the thicker flakes of the twin rolled material.

d (nm)	*Relative Intensity*	*(hkl)*
0.157	M	420
0.166	W	330
0.170	VW	322
0.188	M	321
0.204	M	222
0.247	S	220
0.251	W	*
0.287	VS	211
0.291	W	*
0.304	W	*
0.312	M	210
0.405	W	111
0.498	W	110

Table 3.1. X-ray diffraction data for the thinnest samples which were melted with an oxygen torch and rapidly solidified with a twin-roller devise. The hkl's are calculated on a cubic cell of lattice constant a=0.701 nm. The * indicates that these d-spacings cannot be indexed to the cubic cell.

d(nm)	*Relative Intensity*	*Phases found*
0.157	M	c
0.159	M	+
0.165	M	-
0.176	M	-
0.180	M	-
0.187	M	+,c
0.192	W	-
0.196	W	-
0.202	S	c
0.214	W	+
0.224	M	+,§
0.227	M	-
0.230	W	-
0.248	VS	c
0.263	M	+,§
0.285	VS	c,§
0.294	S	+,§
0.302	VS	+,c
0.311	M	c

Table 3.2 X-ray diffraction results for the 1:2:3 compound melted by the H_2O_2 torch and solidified by the melt drop and melt extraction techniques. c=cubic phase, + =BaCuO2, § = Y_2BaCuO_5, - =unidentified peak. Note absence of the 0.275 and 0.273 nm peaks, the two strongest peaks for the 1:2:3 orthorhombic phase.

From these results it appears that the solidification behavior of the 1:2:3 compound is quite complex at low to moderate solidification rates and yields a phase assemblage that does not contain any 1:2:3 composition in either the tetragonal or orthorhombic structures. Due to the multiple phases found in these materials, it is possible that the 1:1:2 and 2:1:3 could be present, but could not be identified with x-ray diffraction. Only at the highest quenching rates were amorphous materials identified.

The results in Table 3.2 are for 1:3:4 melt extracted flakes and 1:2.5:3.5 melt-dropped samples. All three compositions are found to contain both the cubic phase and 0:1:1 along with some unidentified, but weak, peaks. The presence of 2:1:1 could not be detected. This suggests that the cubic phase is not a high temperature polymorph of 2:1:1. The 1:2.5:3.5 composition contains the greatest amount of the cubic phase, while the 1:3:4 compound contains the most $BaCuO_2$, which is in agreement with the phase diagram. The cubic phase is present for the spectrum of cooling rates attained through the three solidification techniques and sample compositions, whereas the $BaCuO_2$ is only found for the moderate to slowly cooled samples. It is assumed that barium vaporization is negligible due to the short time the sample is heated, and melted and thus the cubic phase must be yttrium and copper rich to co-exist with $BaCuO_2$, as discussed in further detail in Sec. 3.5.2.

$YO_{1.5}$:BaO:CuO			
1:2.5:3.5		1:3:4	
d (nm)	*Relative Intensity*	*d (nm)*	*Relative Intensity*
0.444	W	0.311	S(c)
0.308	VS(c)	0.297	S(+)
0.303	S(+)	0.292	W
0.266	M(+)	0.220	M(+)
0.247	W(c)	0.198	M(c)
0.213	W(+)	0.187	S(+,c)
0.193	W	0.177	W
0.188	M(+,c)	0.174	W
0.160	W(+)	0.165	W(c)
		0.159	W(+)
		0.156	M(c)

Table 3.3. Debye-Scherrer x-ray diffraction results for the melt extracted, as-quenched materials of composition Y-1:2.5:3.5 and for the melt dropped Y-1:3:4. Patterns index to the cubic phase (c) and $BaCuO_2$ (+). The Y_2BaCuO_5 phase was not detected.

Annealing the samples generated from all three melting techniques in O_2 at 950°C transformed the material into the o-1:2:3 phase. The duration of the anneal was from 1-16 hours, depending on the bulk density of the samples. Annealing for 1 hour was sufficient time to transform the as-quenched material into the single phase o-1:2:3 for the twin rolled and melt extracted flakes. Table 3.4 summarizes the various techniques, estimated quench rates and products obtained in the as-quenched and annealed conditions.

Technique	dT/dt (K/sec)	Materials Produced	Phases Present	Heat Treatment	Phases Present
Melt drop	300	1-5 gms 0.20-0.75 cm dia. 0.05-0.30 cm thick	$BaCuO_2$, Y_2BaCuO_5 and cubic phase	950°C 4-16 hours	1:2:3
Melt extraction	10^4-10^6	Flakes, 1-3mm long 400 μm thick	$BaCuO_2$ Y_2BaCuO_5 and cubic phase	950°C 1-16 hours	1:2:3
Twin Rolling	10^5-10^7	Flakes, 2-3 cm length 10-100 μm thick	Cubic phase and amorphous materials	950°C 1-6 hours	1:2:3

Table 3.4. Materials produced and phase identification for as-quenched and heat treated samples made from melting the 1:2:3 compound with an H_2-O_2 torch.

Annealing has two effects in all of the melted and solidified samples. First it crystallizes any amorphous material present and then transforms the multiphase system into the single orthorhombic 1:2:3 phase.

3.4 DTA Results

DTA results on the twin rolled samples are shown in Figure 3.0 for as-quenched samples of compositions $YBa_2Cu_3O_{7-x}$, $EuBa_2Cu_3O_{7-x}$ and $GdBa_2Cu_3O_{7-x}$. Table 3.5 lists the exo- and endothermic reaction temperatures. The flakes were selected at random and no special care was taken to select only flakes of uniform thickness. Upon heating the as-quenched materials, an exotherm occurs for all the three compositions in the range of 730-750°C which does not occur during cooling. This corresponds to a crystallization event of the amorphous materials quenched-in from the melt. Endothermic reactions occur in the range of 900-1085°C for all three compositions. The endotherm between 900-910°C is attributed to melting of the eutectic between $BaCuO_2$-CuO [McCallum et al. (1987), Roth et al. (1987)], which occurs at roughly the same temperature for the three compositions (See Figure 3.0). .The endotherms occurring between 935-945°C for the three samples can be attributed to decomposition of CuO into Cu_2O [Liang et al. (1987)], although Roth et al.(1987) report a decomposition temperature of 1025°C. It is likely that the p_{O_2} in these two experiments was not the same. For the data presented here, the low decomposition temperature indicates that a higher over pressure of O_2 is needed to prevent the formation of Cu_2O. The endotherms which occur in the range 970-1035°C are due to melting of an oxygen deficient $BaCuO_x$. The melting point of $BaCuO_2$ is reported to be between 970-1020°C. The endotherms in the range of 1035-1085°C are due to the peritectic decomposition of $MBa_2Cu_3O_{7-x}$ into a Ba and Cu rich liquid and a solid of composition M_2BaCuO_5 [McCallum et al. (1987)]. The peritectic decomposition temperature is 50°C higher for the Eu and Gd samples than for the Y samples.

	Y-Ba-Cu	Eu-Ba-Cu	Gd-Ba-Cu		Y-Ba-Cu	Eu-Ba-Cu	Gd-Ba-Cu
Heating (°C)				*Cooling (°C)*			
Exotherms	745	730	750	Exotherms	1060	1045	1035
Endotherms	900	905	910		915	920	915
	935	945	945			905	
	970	1030	1035				
	1035	1085	1085				

Table 3.5. DTA results on the as-quenched $YBa_2Cu_3O_{7-x}$, $EuBa_2Cu_3O_{7-x}$, and $GdBa_2Cu_3O_{7-x}$ compositions.

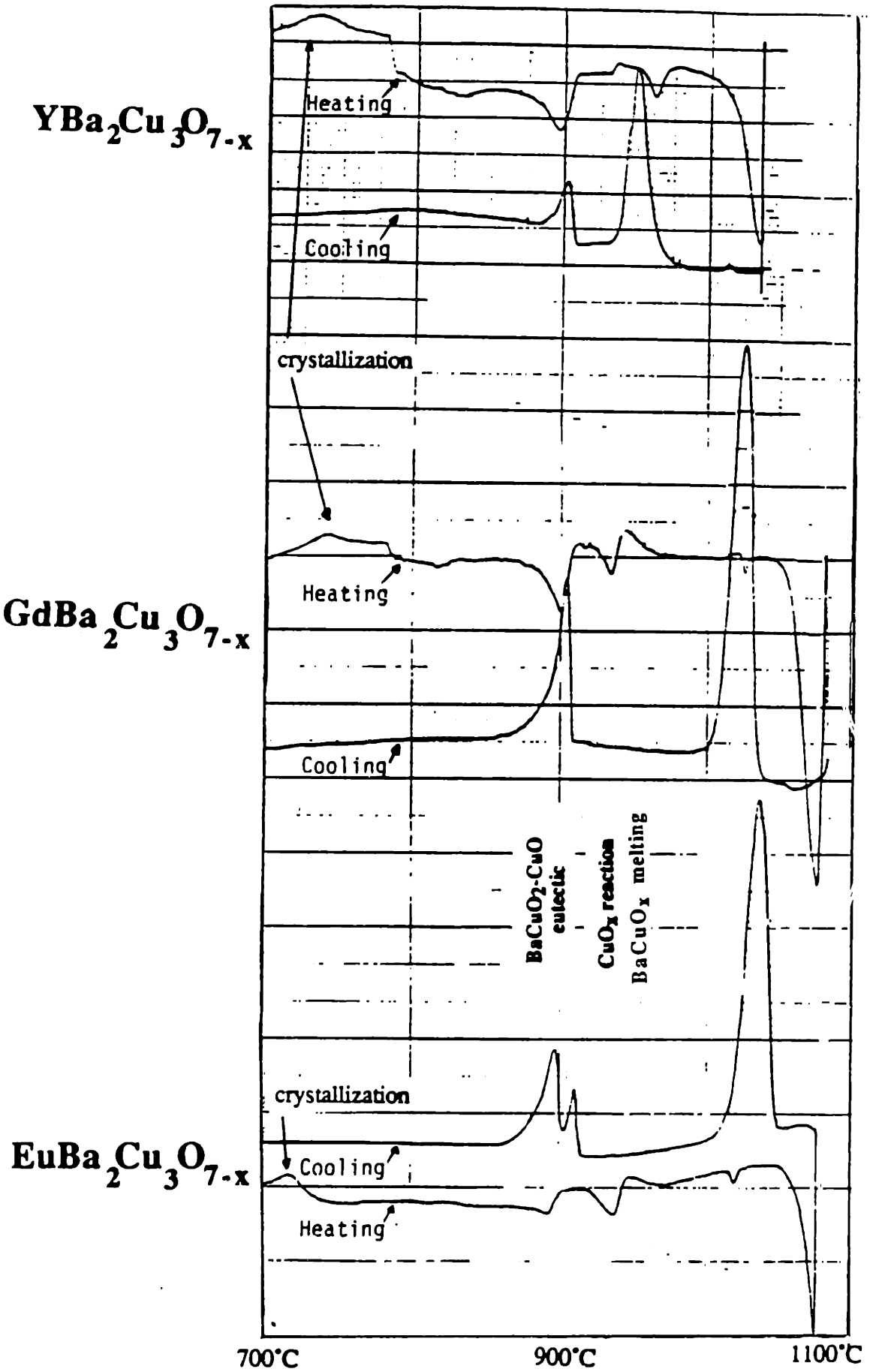

Figure 3.0
DTA traces for the as-quenched material upon heating and cooling for (a) $YBa_2Cu_3O_{7-x}$, (b) $GdBa_2Cu_3O_{7-x}$ and (c) $EuBa_2Cu_3O_{7-x}$.

X-ray diffraction results showed that the samples had transformed into the o-1:2:3 phase after the first DTA run. These samples were re-heated in the DTA. Table 3.6 lists the thermal reaction temperatures for the three compositions. The results for the $YBa_2Cu_3O_{7-x}$ are similar to what has been reported by Cook et al. (1987). Three endotherms occur upon heating which correspond to melting of the $BaCuO_2$-CuO eutectic, the copper reduction reaction, and the peritectic decomposition of $MBa_2Cu_3O_{7-x}$. It appears that the only significant difference between the rapidly quenched materials and the reheated samples is the presence of the exothermic crystallization peak in the as-quenched samples and the presumed melting of $BaCuO_x$. The as-quenched materials have a greater amount of $BaCuO_2$ than the annealed materials and thus is easier to detect in the DTA experiment. The absence of the $BaCuO_x$ reaction in the annealed materials are likely due to a lack of sensitivity in the measurements.

	Y-Ba-Cu	Eu-Ba-Cu	Gd-Ba-Cu		Y-Ba-Cu	Eu-Ba-Cu	Gd-Ba-Cu
Heating (°C)				*Cooling (°C)*			
Endotherms	935 980 1040	930 1030 1085	935 1035 1085	Exotherms	975 910	1045 900	1030 905

Table 3.6. DTA results on the re-heated as-quenched $YBa_2Cu_3O_{7-x}$, $EuBa_2Cu_3O_{7-x}$, and $GdBa_2Cu_3O_{7-x}$.

Figure 3.1(a) shows the x-ray diffraction results for the as-quenched and annealed $YBa_2Cu_3O_{7-x}$ samples. The as-quenched material has an amorphous phase as shown by the characteristic broad peak around $2\theta=25°$. The crystalline peaks index to a mixture of the cubic phase, $BaCuO_2$ and some Y_2BaCuO_7. Annealing the sample at 859°C, above the exothermic reaction temperature, causes complete crystallization of the glassy material. After annealing the sample at 924°C, the peaks for the tetragonal phase are well developed, although there is some $BaCuO_2$ present as well. Annealing at 954°C develops the orthorhombic phase and the peaks for $BaCuO_2$ have shrunk comparatively. After an anneal

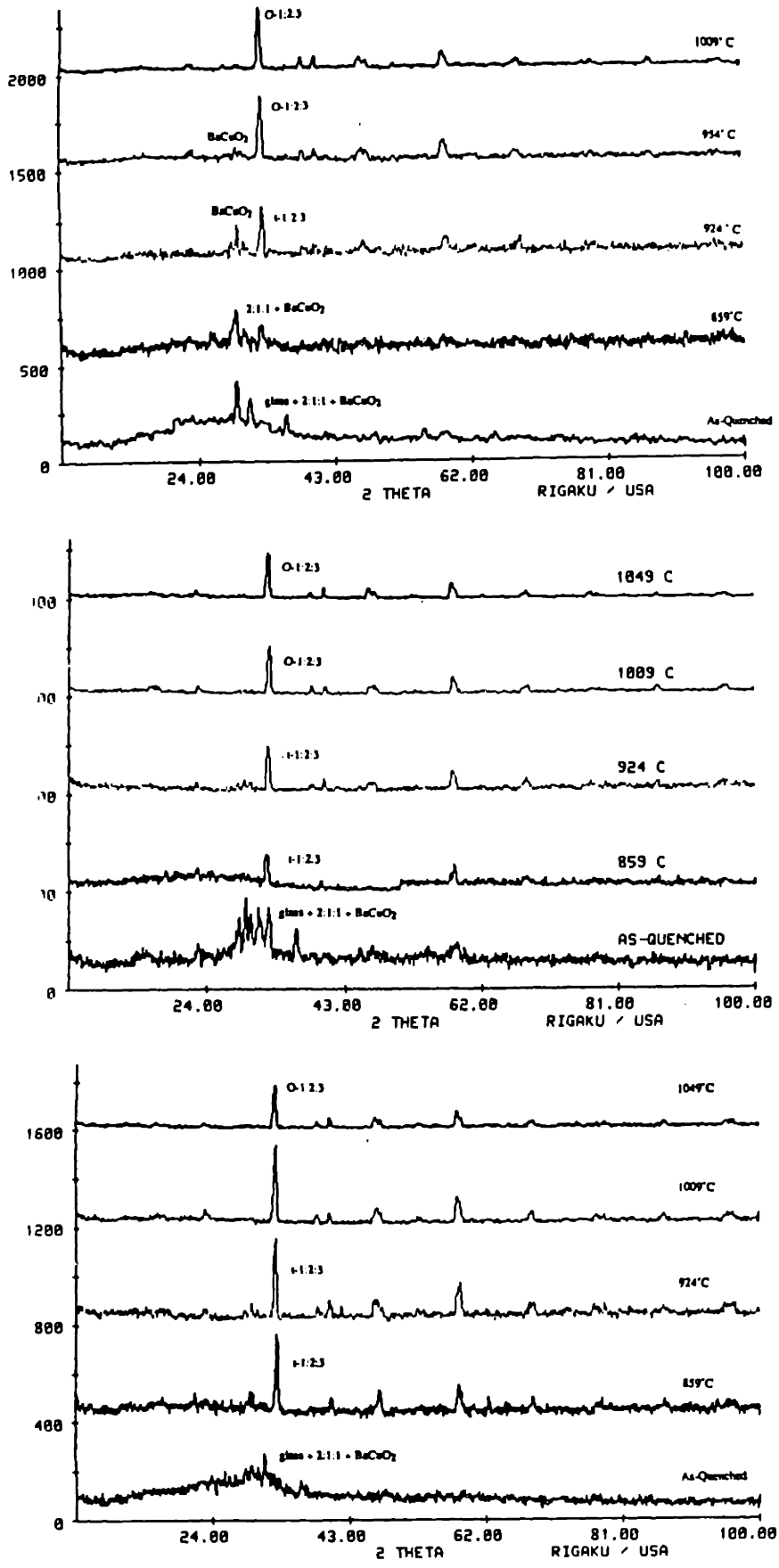

Figure 3.1

X-ray diffraction results for the as-quenched and annealed (a) $YBa_2Cu_3O_{7-x}$, (b) $EuBa_2Cu_3O_{7-x}$ and (c) $GdBa_2Cu_3O_{7-x}$ samples.

at 1009°C, only the orthorhombic phase is detectable. In these samples, the retention of the tetragonal phase is seen through the merging of the (013) and (103), the (020) and (200), and the (123) and (213) peaks in the x-ray diffraction spectra and by the shape of the (103) peak. For the orthorhombic phase, the (103) peak is skewed towards the higher d-spacings and for the tetragonal phase, it is skewed towards the lower d-spacings.

Figure 3.1(b) shows the x-ray diffraction results for the as-quenched and annealed $EuBa_2Cu_3O_{7-x}$. The as-quenched material shows the presence of a glassy phase and the tetragonal 1:2:3 phase. Annealing at 859°C has crystallized the glass and further developed the tetragonal phase. At 924°C, peaks for $BaCuO_2$ are seen along with the tetragonal phase. At 1009°C, the orthorhombic phase has developed and $BaCuO_2$ is still present, but it disappeared after annealing at 1049°C.

Figure 3.1(c) shows the x-ray diffraction results for the as-quenched and annealed $GdBa_2Cu_3O_{7-x}$ samples. The as-quenched material shows glassy phase with no peaks of the orthorhombic phase. Annealing at 859°C, above the exothermic reaction temperature, results in the formation of the tetragonal phase. At 924°C and 1009°C, the structure has not changed significantly, indicating the reactions between CuO and $BaCuO_2$ have contributed to the endotherms on the DTA traces. After annealing at 1049°C, the only phase present is the orthorhombic phase.

The first 1:2:3 phase to appear after annealing the rapidly solidified materials is the tetragonal phase. There are two reasons that explain why the stable high temperature phase is observed after heating above then cooling below the t->o transformation temperature: (1) surface energy constraints in the developing crystallites favor the formation of the higher symmetry phase and/or (2) the oxygen content in the as-quenched materials is not sufficient to cause the t->o transformation at these temperatures. Preliminary RBS data on the as-quenched materials show an oxygen content of x~1.5, which is a highly oxygen deficient system. Recall that the lowest value found in the orthorhombic phase is $x \approx 0.7$ and that the t->o transformation is typically between 520-686°C. In this case, the samples would have to be annealed at higher temperatures in O_2 Alternatively, the samples could be annealed under higher p_{O_2}'s and lower temperatures in order to drive the transformation.

3.5 Microstructural Evaluation

3.5.1 SEM and EDS Analysis

Figure 3.2(a) shows SEM micrographs for the annealed molten droplet. The density of the solidified molten droplets was 5.01 gm/cm^3, compared to a density calculated from the lattice parameters [Siegrist et al. (1987).] of 6.357 g/cm^3, implying ~20% porosity. The porosity arises from solidification voids present in this material, as shown in a lower magnification SEM micrograph in Figure 3.2(b). The microstructure consists largely of elongated, rectangular grains of average length 10 μm and 2-3 μm in average diameter . On the basis of the EDS analysis, these grains have a composition of Y:Ba:Cu in a 1:2:3 ratio. The composition in these grains is uniform within the limits of the x-ray detector. Grant et.al. (1987) reported that electron microprobe results on the orthorhombic 1:2:3 compound showed significant compositional variations for materials prepared by the conventional powder processing route.

EDS analysis on some of the transverse sections of the thicker as-quenched, twin rolled 1:2:3 flakes show a non-uniform compositional profile. A depletion of barium occurs along the edges of the flake and an excess is found in the center of the flake. Recall that the x-ray measurements have shown that these materials consist of the cubic phase, 2:1:1 and 0:1:1. Semi-quantitative analysis on several areas within one sample reveals the quantity of Y:Ba:Cu found along the edges of the transverse sections to be in the compositional range of [5.5±2.4]:[34.4±11.8]:[60.1±12.5] in atomic percent. This corresponds approximately to an average composition of 1:4.3:7.6. In the middle of the flake the compositional range was [43.7±15.8]:[14.0±4.1]:[42.2±11.9] in atomic percent. This corresponds to an approximate composition of 1:0.24:0.71. This indicates that the 2:1:1 phase forms on the surface next to the rollers, and the barium rich phases form in the center of the flakes. In light of this data, it seems likely that barium vaporization occurred during the melting process. Vaporization would transpire on the surface of the droplet which is the surface that comes in contact with the rollers. The overall composition remains 1:2:3, but other as yet unknown phases may be present because of the non-uniformity of the chemical composition across the transverse section. There are several unidentified peaks in the x-ray data which could be from some undocumented phases.

The phase diagram for this system is quite complex and is not fully mapped. There are various high temperature metastable phases which have been identified, plus numerous

(a)

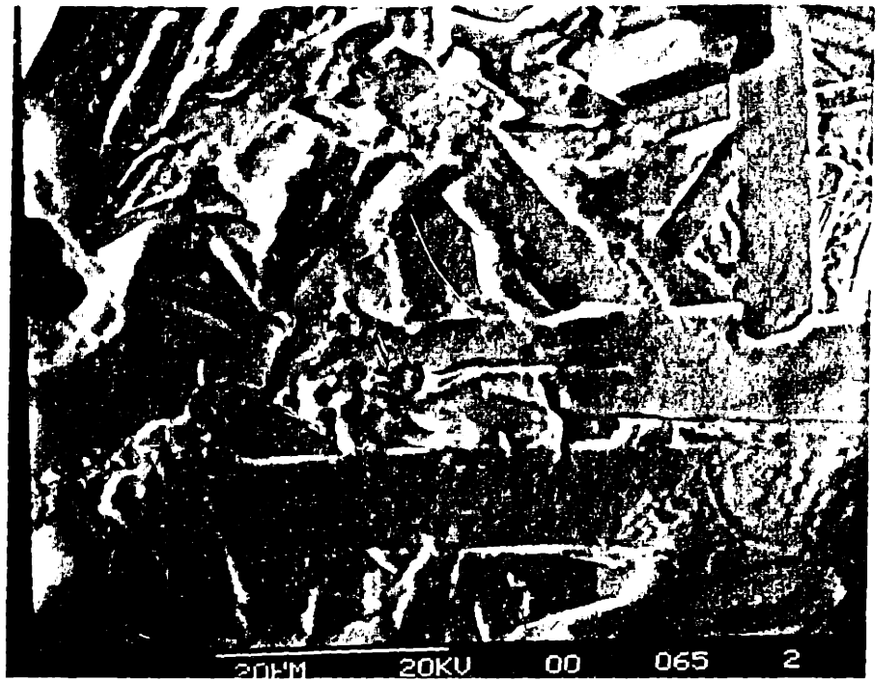

(b)

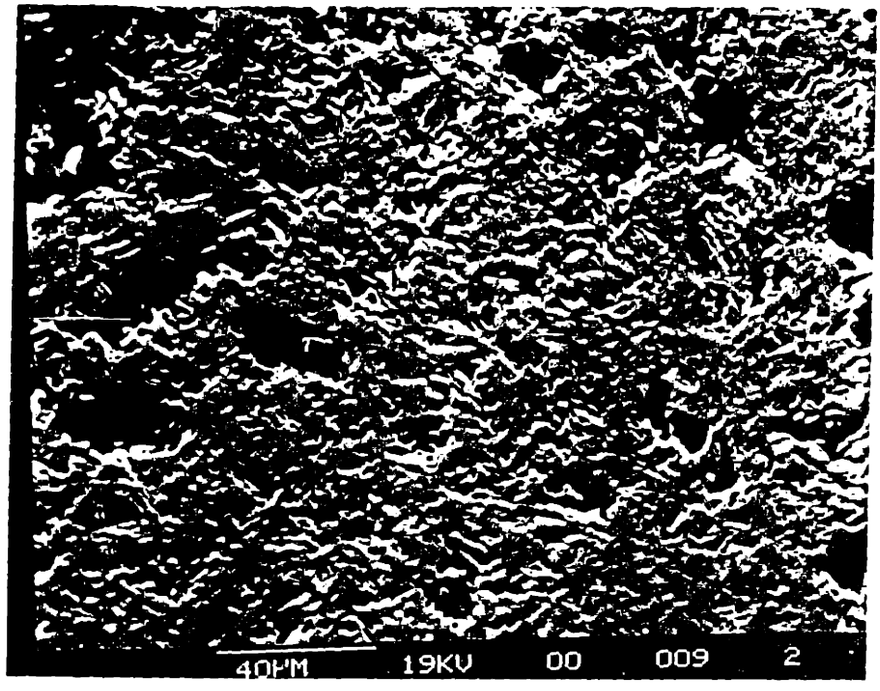

Figure 3.2
(a) SEM photomicrograph of the annealed melt dropped sample of $YBa_2Cu_3O_{7-x}$. (b) Lower magnification SEM micrograph of the sample showing the solidification voids.

stable room temperature phases. For example, a 1:1:2 compound [Clarke (1987)] has been reported to be a cubic compound which appears as a minor phase in the 1:2:3 compound sintered at 1050°C. This is a higher sintering temperature than is typically used, and this could be a metastable, high temperature phase.

3.5.2 TEM

TEM work was performed on the O_2 as-quenched and annealed flakes obtained from the twin roller technique. Figure 3.3 shows an amorphous bright-field micrograph and diffraction pattern for an as-quenched flake. No evidence of crystallinity is observed in this region. In other areas, there are amorphous regions in which small cubic crystallites were embedded are shown in Figure 3.4. The figure shows a bright field image and a dark field image taken from one of the spots, which can be indexed to the cubic phase. The microstructure is not uniform for these as-quenched materials in that large areas of completely amorphous materials are found along with microcrystalline and amorphous materials in different regions. There are three possible explanations for this observations: (1) ion milling of the samples irradiated the material sufficiently to create amorphous material, (2) the solidification rate was not uniform through the thickness of the flake. and/or (3) the droplet of material had not completely melted as it fell from the pellet to the rollers. Explanation (1) is not likely because the samples showed the presence of amorphous regions in the x-ray data and care was taken to ion mill on the cold stage. For explanation (2), the cooling rates for the twin roller system are on the order of 10^7 K/sec (see Part II, Sec. 3.1.7) for flakes ~50 μm in thickness. Materials produced by this technique are compositionally uniform for the ZrO_2 containing samples, and it is reasonable to assume that this quenching technique applied on the superconductors would not yield results which are substantially different. Which leaves explanation (3) as the most likely possibility. The Y-1:2:3 compound is a peritectic and upon melting forms a copper-rich liquid. If the droplet was not completely liquid before it was rapidly solidified, small crystallites could be present in the liquid. Rapid solidification of this material would result in samples which contain amorphous and microcrystalline regions.

TEM results on the 10 hour, 950°C annealed material is shown in Figure 3.5. This material contains only the o-1:2:3 phase according to the x-ray data. Twinning with an average spacing of 50 nm is clearly observed in the bright field micrograph taken along the

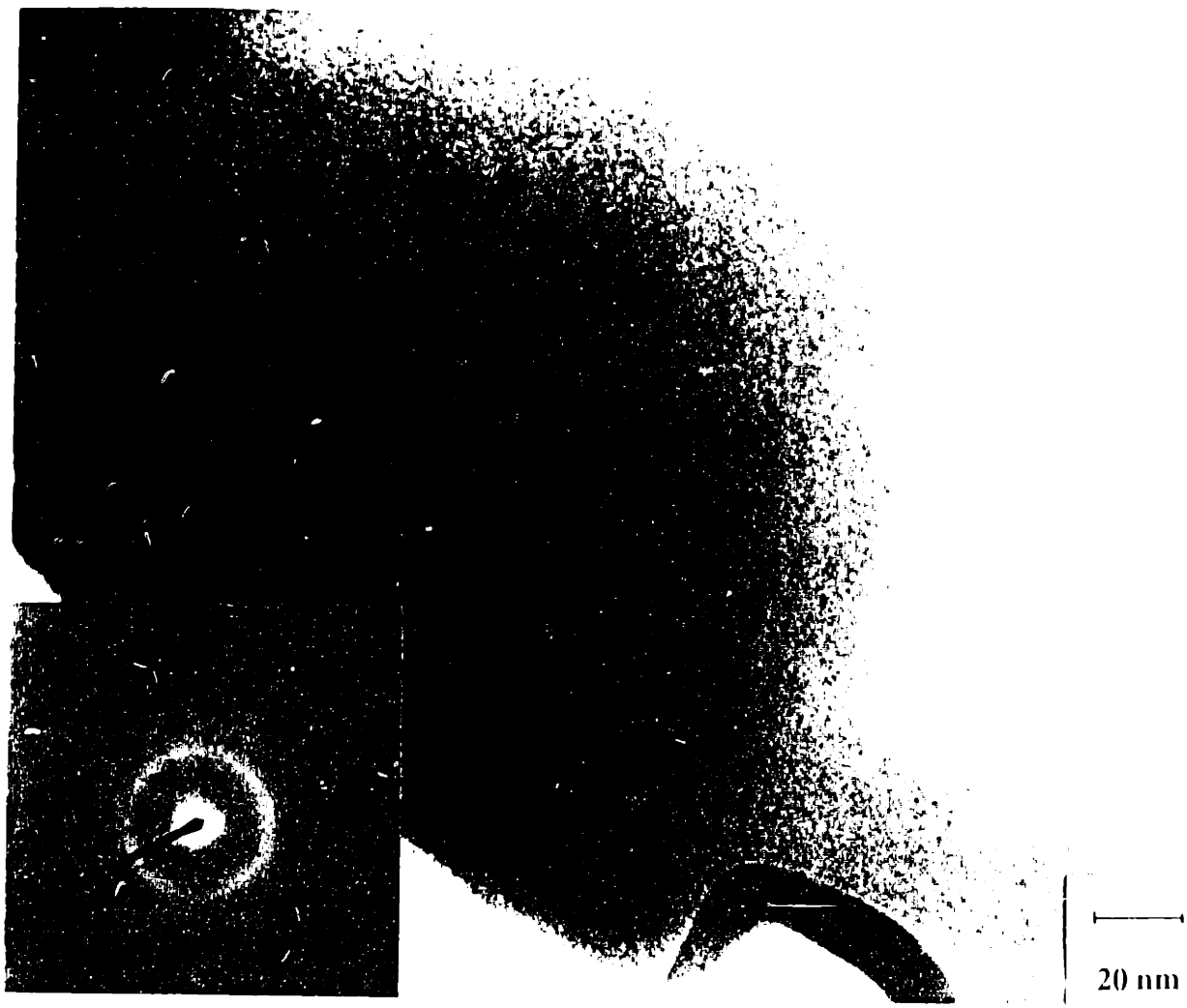

Figure 3.3
Bright field TEM micrograph and diffraction pattern of the as-quenched, amorphous $YBa_2Cu_3O_{7-x}$.

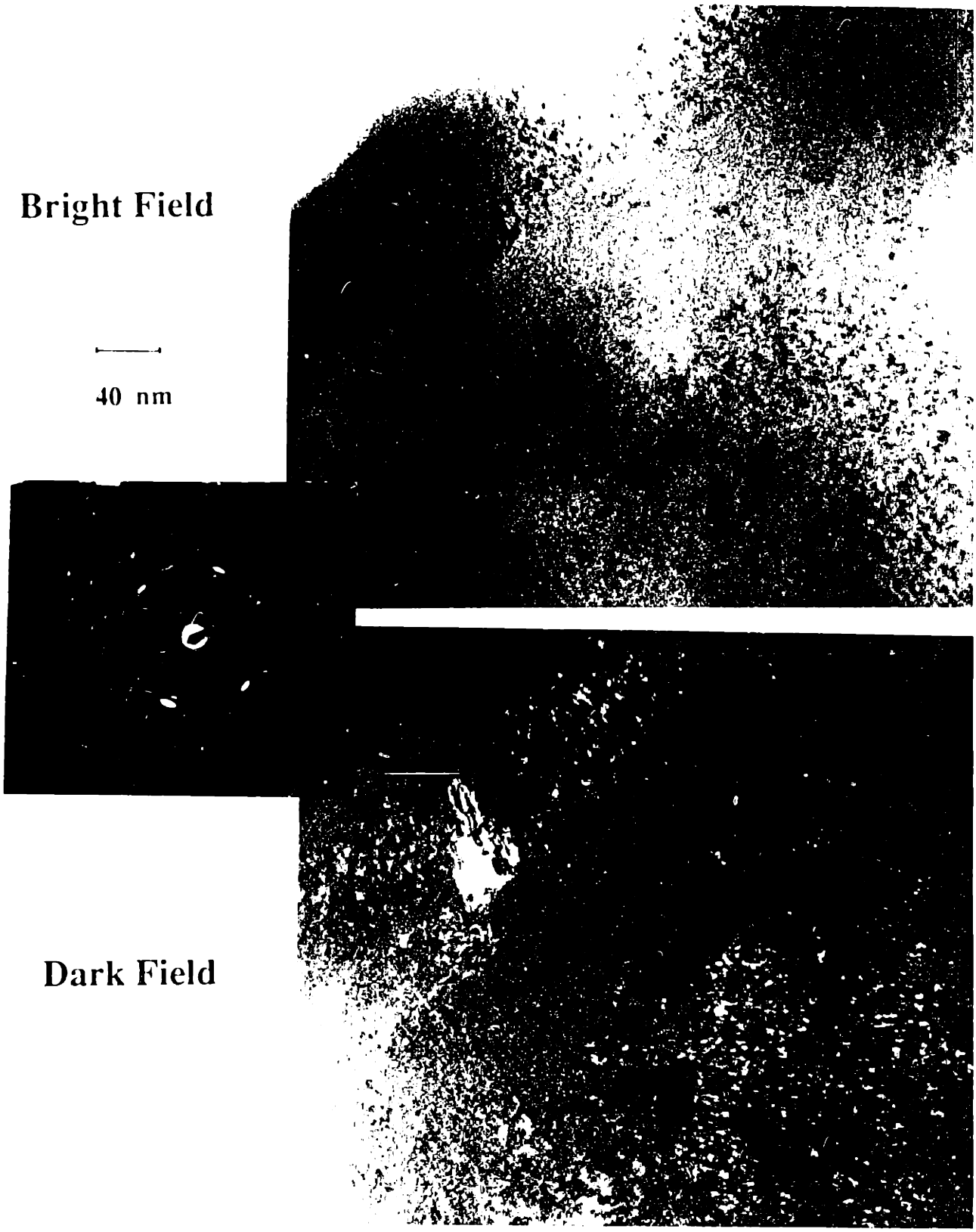

Figure 3.4
Bright field and dark field TEM micrographs with diffraction pattern of the as-quenched, twin rolled $YBa_2Cu_3O_{7-x}$ showing cubic crystallites embedded in the glass. Dark field taken from the 1:00 spot.

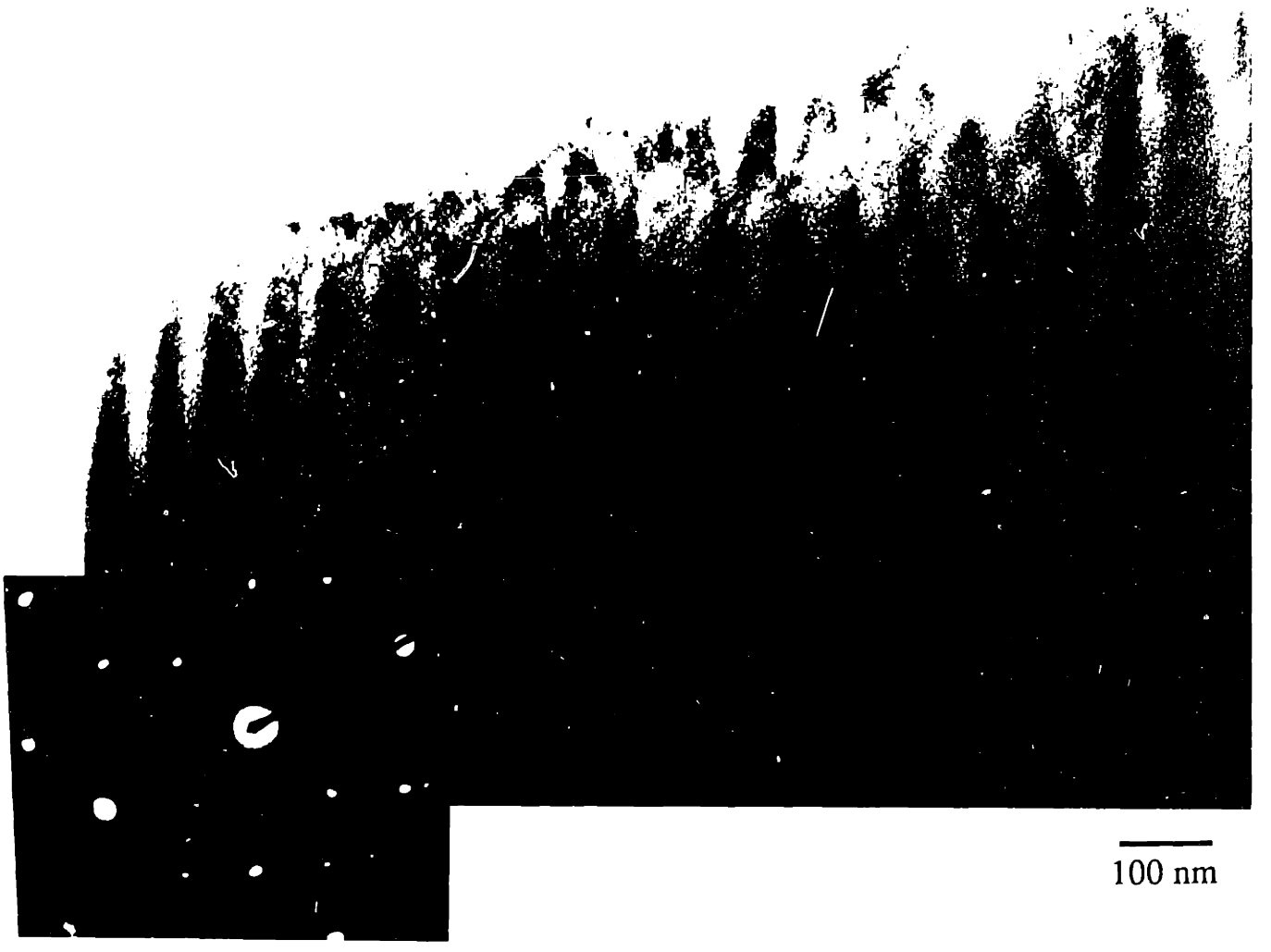

Figure 3.5
Bright field TEM micrograph and diffraction pattern of rapidly solidified $YBa_2Cu_3O_{7-x}$ after an anneal at 950°C in O_2 for 5 hours. Micrograph is taken along the [001] direction.

[001], and spot-splitting can be seen in the diffraction pattern. The twin spacing is much finer in these materials than for samples prepared through conventional powder processing techniques, which typically show spacings of ~500 nm

3.5.3 STEM

Figure 3.6 shows STEM results for the Y-1:2:3 material annealed at 780°C for 2 hours. The microstructure consists of small equiaxed crystallites and some rectangular shaped grains embedded in a glass . The small crystallites have the cubic structure. The microdiffraction pattern taken from one of the elongated, rectangular grains shows a tetragonal pattern. The x-ray data on samples annealed under these conditions show the presence of t-1:2:3 and thus it seems likely that the rectangular grains are the t-1:2:3. The rectangular grains have compositions of elemental ratios Y/Ba ≈ 1/2 and Y/Cu ≈ 1/3. The cubic phase has Y/Ba ≈ 1/2 and Y/Cu ≈ 1/5 indicating that the cubic phase is enriched in copper. The glass surrounding the cubic phase has a concentration ratio of Y/Cu ≈ 1/2, indicating that the cubic->tetragonal transformation requires at least some copper diffusion. According to these compositions, the cubic phase lies along the CuO-$YBa_2Cu_3O_{7-x}$ tie line at 0.67 CuO-0.33 $YBa_2Cu_3O_{7-x}$. The phase diagram for this binary system has not been studied to date and the only known compositions are CuO_x and $YBa_2Cu_3O_{7-x}$. The cubic phase is metastable, which indicates that this binary system is not a simple eutectic.

Figure 3.7 shows a STEM photomicrograph and x-ray microanalysis results on the annealed Y-1:2:3 material. The diameter of the STEM probe is 2-3 nm. The compositions were collected at several points across two boundaries and within three grains. The grain boundaries are sharp and no presence of a second phase is detected. As shown, the Ba, Y and Cu concentrations do not vary significantly, indicating that the annealed, rapidly solidified materials have very clean grain boundaries within the limits of the STEM windowless x-ray detector. Chiang et al. (1988) have pointed out that grain boundary segregation of Sr in $La_{1.85}Sr_{0.15}CuO_{4-y}$ could be detected with a scanning Auger microprobe but was not with the STEM x-ray measurements. It is possible that segregation of certain elemental species occurs in the Y-1:2:3 materials, but it was not observed in the STEM.

Figure 3.8 shows STEM results on the annealed Y-1:2:3 rapidly solidified material. The twin spacing is ~50 nm which is quite small compared to conventionally powder

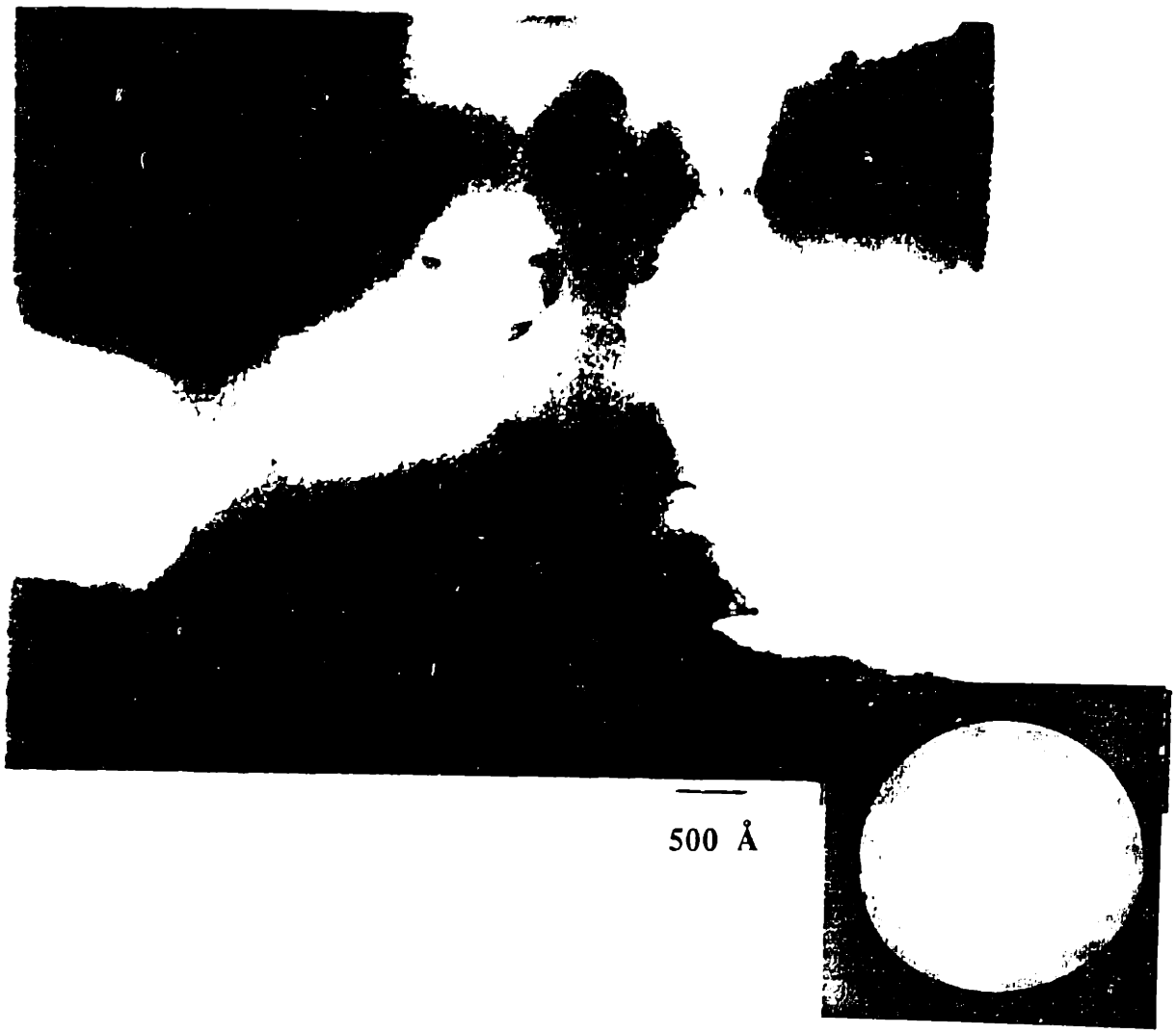

Figure 3.6
STEM micrograph of the $YBa_2Cu_3O_{7-x}$ composition annealed at 780°C for 2 hours showing the cubic crystallites and the tetragonal $YBa_2Cu_3O_{7-x}$ phase.

[001], and spot-splitting can be seen in the diffraction pattern. The twin spacing is much finer in these materials than for samples prepared through conventional powder processing techniques, which typically show spacings of ~500 nm

3.5.3 STEM

Figure 3.6 shows STEM results for the Y-1:2:3 material annealed at 780°C for 2 hours. The microstructure consists of small equiaxed crystallites and some rectangular shaped grains embedded in a glass . The small crystallites have the cubic structure. The microdiffraction pattern taken from one of the elongated, rectangular grains shows a tetragonal pattern. The x-ray data on samples annealed under these conditions show the presence of t-1:2:3 and thus it seems likely that the rectangular grains are the t-1:2:3. The rectangular grains have compositions of elemental ratios Y/Ba ≈ 1/2 and Y/Cu ≈ 1/3. The cubic phase has Y/Ba ≈ 1/2 and Y/Cu ≈ 1/5 indicating that the cubic phase is enriched in copper. The glass surrounding the cubic phase has a concentration ratio of Y/Cu ≈ 1/2, indicating that the cubic->tetragonal transformation requires at least some copper diffusion. According to these compositions, the cubic phase lies along the CuO-$YBa_2Cu_3O_{7-x}$ tie line at 0.67 CuO-0.33 $YBa_2Cu_3O_{7-x}$. The phase diagram for this binary system has not been studied to date and the only known compositions are CuO_x and $YBa_2Cu_3O_{7-x}$. The cubic phase is metastable, which indicates that this binary system is not a simple eutectic.

Figure 3.7 shows a STEM photomicrograph and x-ray microanalysis results on the annealed Y-1:2:3 material. The diameter of the STEM probe is 2-3 nm. The compositions were collected at several points across two boundaries and within three grains. The grain boundaries are sharp and no presence of a second phase is detected. As shown, the Ba, Y and Cu concentrations do not vary significantly, indicating that the annealed, rapidly solidified materials have very clean grain boundaries within the limits of the STEM windowless x-ray detector. Chiang et al. (1988) have pointed out that grain boundary segregation of Sr in $La_{1.85}Sr_{0.15}CuO_{4-y}$ could be detected with a scanning Auger microprobe but was not with the STEM x-ray measurements. It is possible that segregation of certain elemental species occurs in the Y-1:2:3 materials, but it was not observed in the STEM.

Figure 3.8 shows STEM results on the annealed Y-1:2:3 rapidly solidified material. The twin spacing is ~50 nm which is quite small compared to conventionally powder

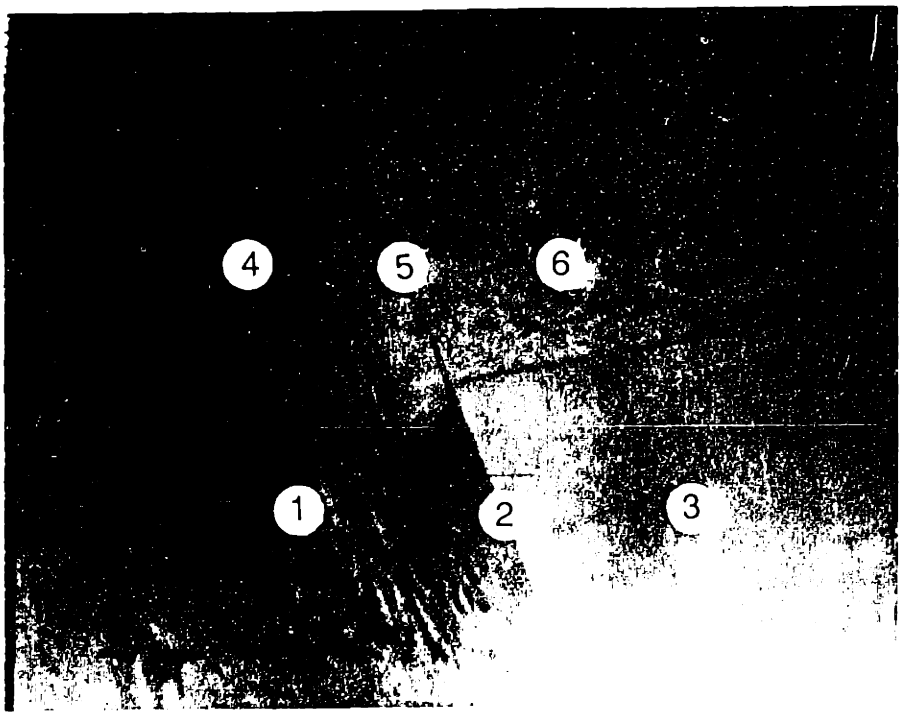

100 nm

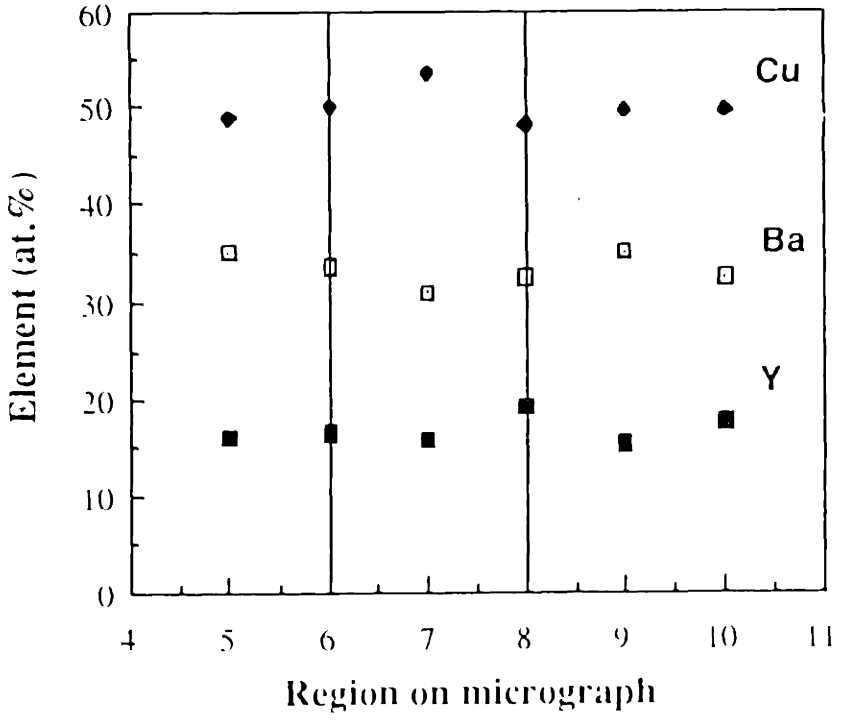

Figure 3.7

STEM results and x-ray microanalysis across grainboundaries in the annealed, rapidly solidified Y-1:2:3 material.

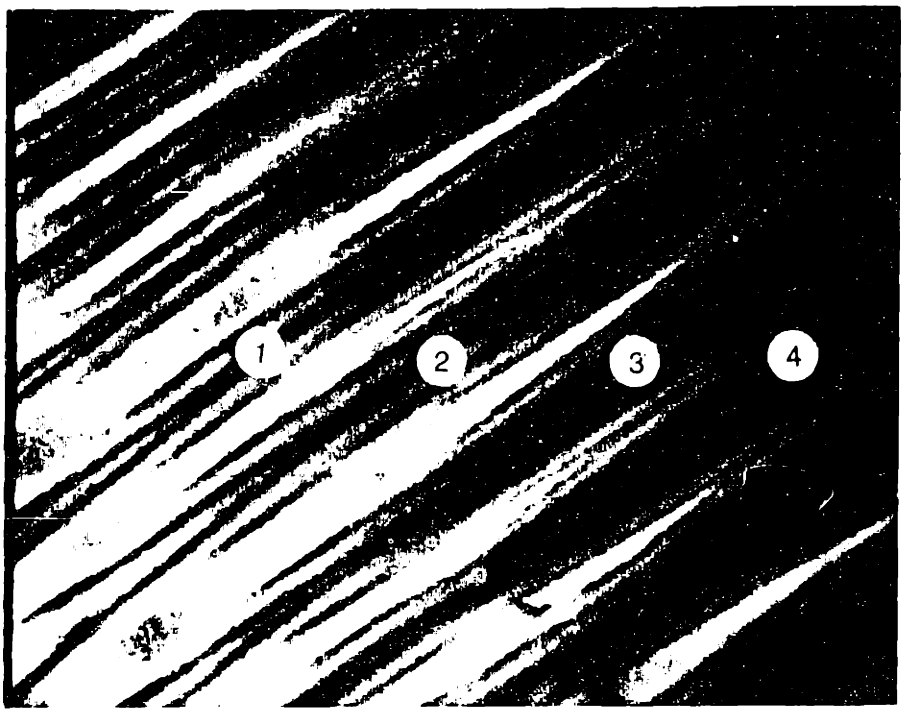

50 nm

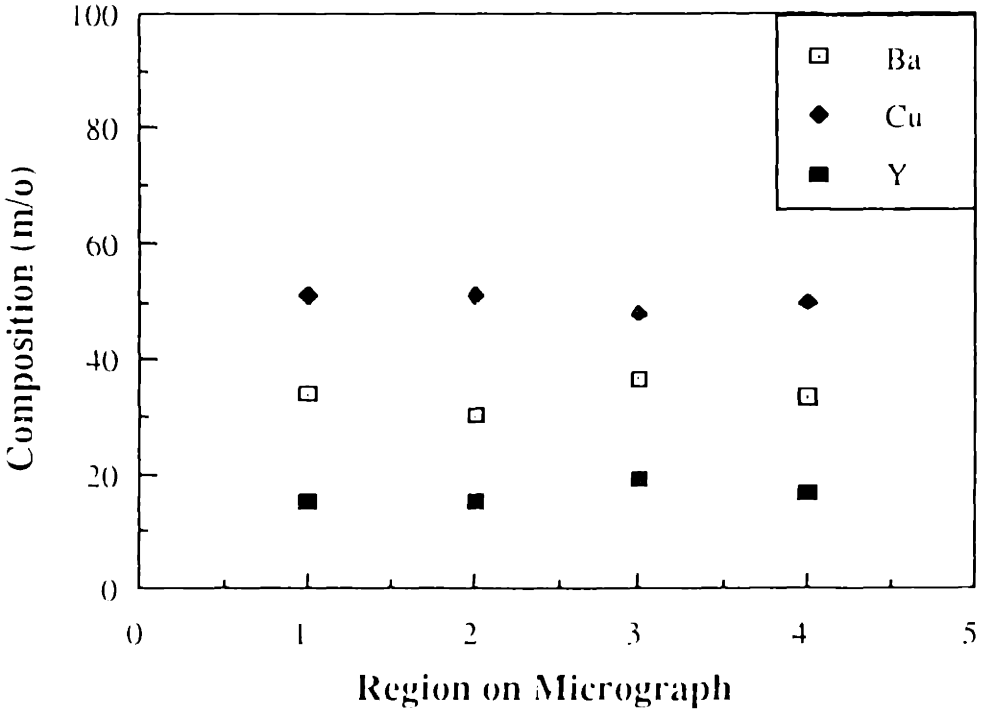

Figure 3.8

Composition of the metallic elements across several twin boundaries in the annealed rapidly solidified Y-1:2:3

processed materials. The composition between the twins does not vary as indicated by the STEM x-ray microanalysis results.

3.6 Electrical Property Measurements

None of the as-quenched samples of any composition were superconducting at liquid N_2 temperatures. Bulk samples have to be annealed for longer times than the rapidly solidified flakes which indicates that oxygen diffusion through the entire sample is crucial for desirable superconducting properties. For the melt processed samples, whether slowly or rapidly cooled, the resistivity vs. temperature measurements can be deceptive. In one case, a melt dropped sample (5.32 gms) was annealed for 1 hour at 950°C in the oxygen furnace. Data were taken with the four-probe technique using silver paint contacts and a current of ~30mA. The sample displayed good superconducting behavior. The transition width, the temperature differential between the drop in resistivity and attainment of zero resistivity, was 1.4 K. Zero resistivity was attained at 91.6 K. This sample was put into another device to measure the current vs. magnetic field as a function of temperature. These results did not show the sample to be superconducting. It is assumed that this is because our annealing conditions were not sufficient for complete diffusion of O_2 through the bulk. The resistivity vs. temperature apparatus measures a surface effect, while the current vs. temperature apparatus measures a bulk effect. Oxygen diffusion throughout the material is critical for the presence of the superconducting orthorhombic phase.

The flakes produced from the twin-roller quenching of compositions Y-1:2:3, Y-1:2.5:3.5 and Y-1:3.5:4.5 were ground into a powder to make a pellet of the material. The powder was pressed under 69 MPa pressure in a cold-press and sintered it at 950°C for 1 hour under flowing O_2. The samples were measured for resistivity changes as a function of temperature, shown in Figure 3.9. This Y-1:2:3 specimen was found to be superconducting with a narrow transition width of ΔT=1.4 K and T_c=91.6 K. The Y-1:2.5:3.5 sample has an excess of $BaCuO_2$ and the resistivity vs temperature plot reflects the presence of a non-superconducting second phase. The transition width is larger and the T_c is smaller (83 K). This sample has ~25 mol% $BaCuO_2$.. The Y-1:3:4 sample has the poorest superconducting behavior. The transition width is greater than 20 K and T_c at zero resistivity is only 41 K. The sample shows semiconductor-like behavior on cooling as the slope of the resistivity vs temperature curve is negative. This sample contains ~50 mol%

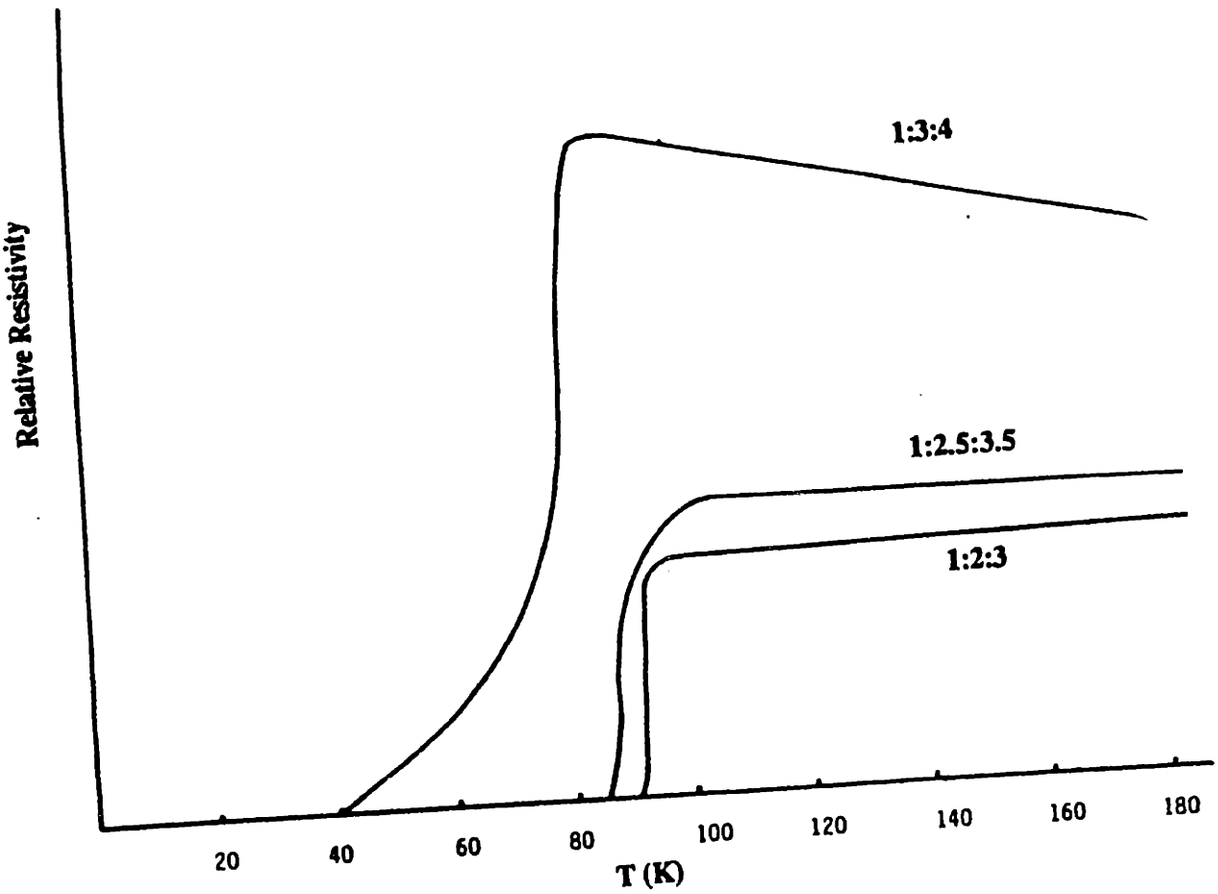

Figure 3.9
Resistivity vs temperature plots for samples prepared through rapid solidification with the twin roller devics. Samples of $YO_{1.5}$:BaO:CuO compositions 1:2:3, 1:2.5:3.5 and 1:3:4 were annealed in flowing O_2 for 1 hour at 950°C.

$BaCuO_2$. It is apparent that any non-superconducting phase destroys the desirable properties of a small transition width and high T_c.

3.7 Magnetic Property Measurements

Figure 3.10 shows field cooled (FC) and zero field cooled (ZFC) magnetic moments as a function of temperature of the melt-extracted 1:2:3 material which had been annealed in oxygen. A 0.76 gm sample was cut from a pellet of annealed, rapidly solidified material The sample was cooled in a zero field and then heated in a field of 100 Oe. This data is shown by the points labeled ZFC in Figure 3.10. After heating to 240 K the sample was subsequently cooled in the same 100 Oe field. The magnetization vs temperature curve for this process is labeled FC. The field cooled sample is indicative of the Meissner effect while the ZFC represents the shielding effect. Based on the mass and ideal density of 6.36 gm/cm^3, a diamagnetic susceptibility of $2.09x10^{-2}$ $emu/Oe{\cdot}cm^3$ is calculated, which represents 26% of ideal diamagnetism. The superconducting transition temperature as derived from the change from paramagnetic to diamagnetic response was measured to be ~88 K in good quantitative agreement with the resistivity data as measured at midpoint. The transformation from paramagnetism to diamagnetism is sharp and well defined, indicating that the material is "clean" and has zero or small deviation from stoichiometry.

The time dependence of the diamagnetic response is:

$$M(t) = M_0 + A(T,H) \ln (t) \qquad (3.0)$$

where M is the induced magnetization, A is the relaxation rate parameter [=dM/dln(t)], T is the temperature and t is the time. The driving force for relaxation is a non-equilibrium flux concentration. The relaxation rate parameter can be expressed by [Hara and O'Handley (1988)]:

$$A=-kTf_m\{M_0-M_e\} \qquad (3.1)$$

where k is Boltzmann's constant, f_m is the average value of the activation energy distribution function, and M_e is the equilibrium magnetization. Figure 3.12(a) shows the

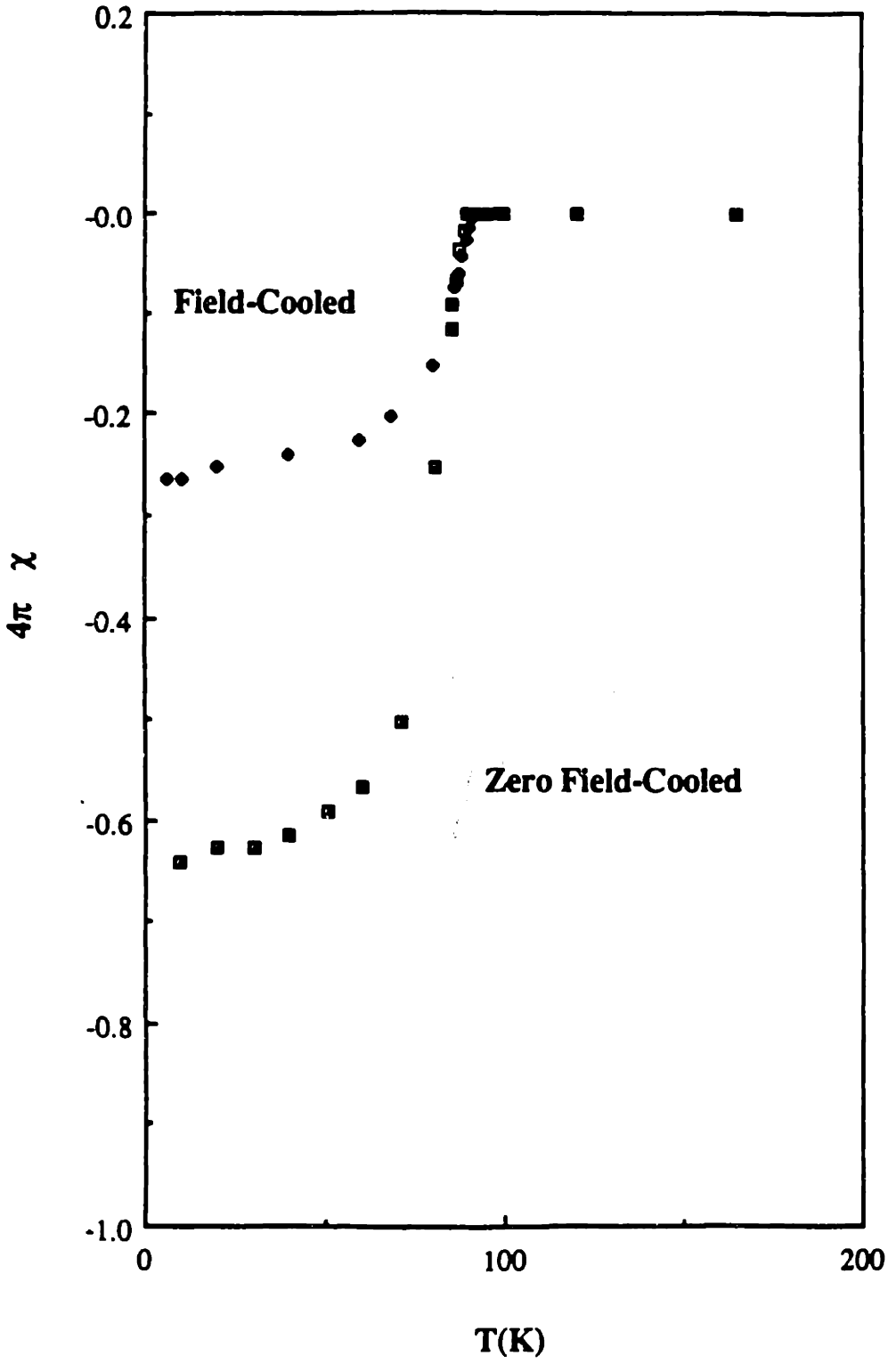

Figure 3.10
Field cooled (Meissner effect) and zero field cooled (shielding) diamagnetic susceptibility as a function of temperature for the annealed, melt-extracted $YBa_2Cu_3O_{7-x}$.

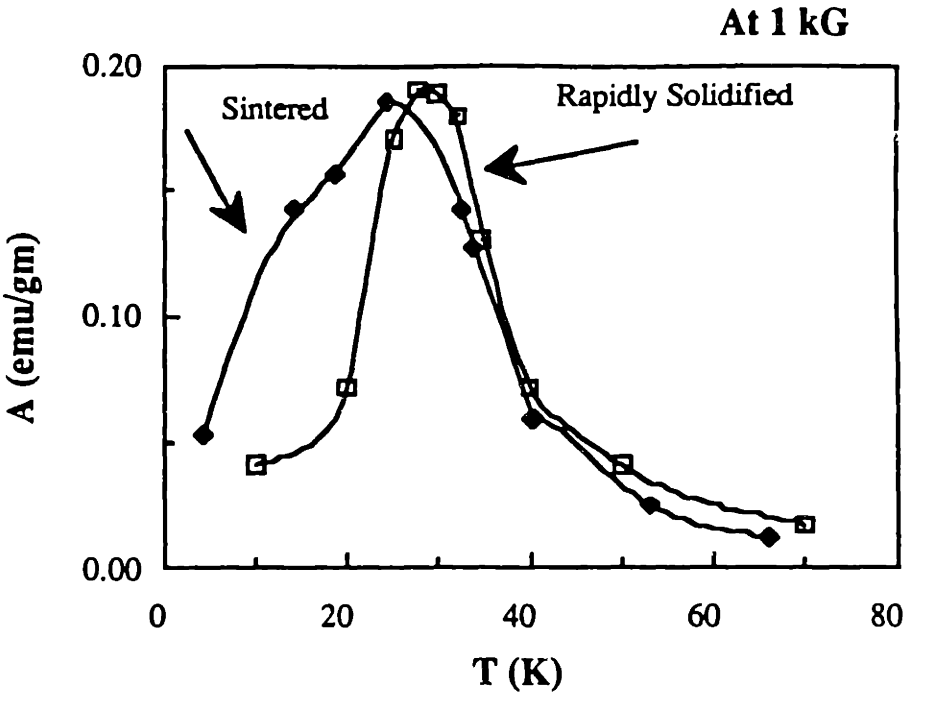

(a)

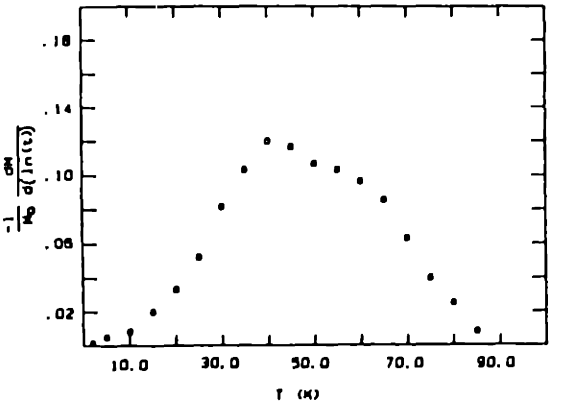

(b)

Figure 3.11

(a) Magnetic relaxation data comparing the annealed, rapidly solidified material with the conventionally prepared sintered material of composition Y-1:2:3. (b) Magnetic relaxation data on a single crystal of Y-1:2:3. From Tuominen et al. (1988).

magnetic relaxation data for the O_2 annealed rapidly solidified Y-1:2:3 material along with data from conventionally prepared powder samples. The relaxation rate parameter, A, was derived for the zero field cooled samples with a subsequent application of a 1 kG applied field, is shown as a function of temperature for both materials in Figure 3.11(a). These spectra are reflective of the distribution of flux pinning barriers in the materials. As shown, the spectrum for the material produced by the rapid solidification processing route, clearly narrower, is indicative of a more well defined distribution of energy barriers for flux motion than that of the conventionally prepared material. Tuominen et al. (1988) have measured A as a function of T for single crystals of Y-1:2:3, shown in Figure 3.11(b). They found a broader distribution than for either the conventionally prepared sintered material or the rapidly solidified material. For A=0.05, the temperature range was between 20-72 K. In the sintered material the range is 5-40 K and for the rapidly solidified material it is 20-40 K. The maximum in the curves for all three materials occurs between 30-40 K, which suggests that the temperature at which the energy distribution is centered may be an intrinsic materials property. The broader distribution found for the single crystals could suggest that the grain boundaries pin the flux more effectively than the twin boundaries, which are presumed to pin the flux in the single crystals.

4.0 CONCLUSIONS

Melting and solidification of compositions in the M-Ba-Cu-O (M=Y, Eu, Gd) has been successfully performed with the use of an H_2-O_2 torch with an O_2-rich flame and three different solidification techniques. Cooling rates attained were between 300-10^7 K/sec. Y-1:2:3 materials produced from the twin roller technique had the fastest solidification rate and were composed of amorphous or amorphous and microcrystalline materials. None of the as-quenched materials produced via the different solidification techniques were superconducting, at least at liquid N_2 temperature. The crystallinity is from a previously unreported cubic phase with a lattice parameter of 0.701 nm. This phase is not a high temperature polymorph of Y-1:2:3 as it is copper rich. The crystallization of the amorphous materials in the Y-1:2:3, Eu-1:2:3 and Gd-1:2:3 systems occurred in the same temperature range of 730-750°C. The peritectic decomposition temperature for Y-

1:2:3 is 1035°C and the Eu and Gd-1:2:3 compositions have a decomposition temperature 50°C higher.

Slower quench rates produce materials with $BaCuO_2$ and Y_2BaCuO_5 along with the cubic phase. The compositional inhomogeneity present across the thickness of a melt extracted flake indicates that the solidification path is complex and further understanding of the phase diagram is needed to elucidate the solidification behavior.

Annealing the as-quenched materials in O_2 leads to the development of the tetragonal phase at low temperatures and the orthorhombic phase does not appear until after heating and cooling from 924°C. The development of first the stable, high temperature phase followed by the stable, low temperature phase is presumed to be due to the high oxygen deficiency present in the as-quenched materials. The t->o transformation is very sensitive to oxygen stoichiometry and will not occur until a minimum of x=0.7. Annealing the as-quenched flakes for 1 hour in flowing O_2 transforms the multiphase material into the single phase, orthorhombic superconducting compound. The materials have very small twin spacings, on the order of 50 nm. The annealed materials show excellent superconducting properties, with a transition width of 1.4 K and a T_c at zero resistivity of 94 K. Magnetic relaxation data has shown that the as-quenched, annealed materials have a narrower distribution of flux pinning site energies compared to those of single crystals and materials prepared via conventional powder processing This may suggest that grain boundaries pin the flux more effectively than the twin boundaries.

PART IV. CONCLUSIONS

Rapid solidification has been used successfully to produce materials with a metastable phase assemblages in two classes of oxides: ZrO_2 containing ceramics and $MBa_2Cu_3O_{7-x}$ (M=Y, Eu, Gd) superconductors. The benefits from employing this processing technique are: (1) increased chemical homogeneity in the as-quenched crystalline phases, (2) the generation of fine grained, uniform microstructures, (3) the production of amorphous materials with unusual properties and finally (4) further clarification of the phase relationships and phase stability in the systems examined. Producing materials far from equilibrium and documenting their approach towards equilibrium gives basic insights into the crystallography and phase compatibility of the equilibrated materials.

The crucibleless melting technique developed for the ZrO_2 ceramics is ideal for melting eutectic compositions. Although it was used on a hypoeutectic, a hypereutectic and a peritectic composition, the possibility of incomplete melting was present as in some cases completely amorphous materials were not generated. The dual H_2-O_2 torch heating technique used on the superconductors proved to be an ideal method for melting, as an overpressure of O_2 can be maintained to inhibit significant reduction of the material. Even so, an oxygen deficiency was present, which suggests that melting under ambient conditions would lead to further reduction and possible liquid-liquid phase separation.

The twin roller quenching device proved to be the best technique for obtaining amorphous materials. The cooling rate is estimated to be between 10^5-10^7 K/sec, depending on the speed of the rollers. The dual substrate solidification technique is best suited for oxides as wetting problems between the liquid and metal substrate are avoided and the heat is extracted more efficiently by the presence of two surfaces.

The uniform, fine grained structures generated during annealing of the ZrO_2 containing glasses and microcrystalline materials indicate that compaction of these materials would lead to high strength and fracture toughness. The microstructures can be tailored as to their grain size and chemical constituents by the application of different solidification rates or by annealing the as-quenched samples under different conditions. The fine grain size and twin spacing found in the annealed, rapidly solidified superconductors give rise to desirable magnetic properties. The small grain size appears to be advantageous in generating a narrow distribution of flux pinning site energies.

Solidification theory has proved to be useful in predicting the types of microstructures obtained through rapid solidification of oxides. If rapidly solidified ceramics are to be exploited commercially, understanding the microstructural development is crucial in order to generate materials with optimal properties.

Rapid solidification has yielded materials with unusual optical properties in the ZrO_2 containing glasses and desirable electrical and magnetic properties in the $YBa_2Cu_3O_{7-x}$ superconductors. The ability to produce quenched materials exhibiting unique physical properties, which are not attained by other processing routes, may lead to valuable and interesting applications for the materials systems examined in this work.

REFERENCES

J.G. Bednorz and K.A. Müller, "Possible High T_c Superconductivity in the Ba-La-Cu-O System", *Zeitschrift fur Physik B*, **64**, 189-193 (1986).

E.G. Behrman et al., "Synthesis, Characterization and Fabrication of High Temperature Superconducting Oxides", *Adv.Ceram.Mat.*, **2**(1987)539-555.

R. Beyers, E. Engler, P. Grant, S. Parkin, G. Lim, M. Ramirez, K. Roche, J. Vazquez, V. Lee and R. Jacowitz, "The Effects of Oxygen Stoichiometry and Oxygen Ordering on Superconductivity in $YBa_2Cu_3O_{9-x}$", in High Temperature Superconductors, eds. M.B. Brodsky, R.C. Dynes, K. Kitazawa and H.L. Tuller, Materials Research Society Symposium Proceedings, Vol 99, 1988, 77-82.

R. Beyers, G. Lim, E.M. Engler, R.J. Savoy, T.M. Shaw, T.R. Dinger, W.J. Gallagher and R.L. Sandstrom, "Crystallography and Microstructure of $Ba_2YCu_3O_{9-x}$, a Perovskite-Based Superconducting Oxide", submitted to *Appl.Phys.Let.*.

G. Calestrani and C. Rizzoli, "Crystal Structure of the $YBa_2Cu_3O_7$ Superconductor by Single Crystal X-ray Diffraction", *Nature*, **328**(1987).

R.J. Cava, B. Batlogg, A.P. Rameriz, D. Werder, C.H. Chen, E.A. Rietman and S.M. Zahurak, "$Ba_2YCu_3O_{7-\delta}$: Effect of Oxygen Stoichiometry", in High Temperature Superconductors, eds. M.B. Brodsky, R.C. Dynes, K. Kitazawa and H.L. Tuller, Materials Research Society Symposium Proceedings, Vol 99, 1988, 19-30.

R.J. Cava, B. Batlogg, R.B. van Dover, D.W. Murphy, S. Sunshine, T. Siegrist, J.P. Remeika, E.A. Rietman, S.Zahurak, and G.P. Espinosa, "Bulk Superconductivity at 91°K in Single-Phase Oxygen-Deficient Perovskite $Ba_2YCu_3O_{9-x}$", *Phys.Rev.Let.*, **58** [16] (1987) 1676-1679.

Y-M. Chiang, A. Roshko, B. Fabes, D. Leung, J. Ikeda, D. Rudman, M. Parker and J. Martin, "Grain Boundary Segregation and Thermal History Effects on Properties of $La_{1.85}Sr_{0.15}CuO_{4-y}$ Superconductors", in High Temperature Superconductors, eds. M.B.

Brodsky, R.C. Dynes, K. Kitazawa and H.L. Tuller, Materials Research Society Symposium Proceedings, Vol 99, 1988, 821-824

C.W. Chu, P.H. Hor, R.L. Meng, L. Gas, Z.J. Huang, Y.Q. Wang, J. Bechtald and D. Campbell, Preprint

D. Clarke, personal communication, 1987.

L.P. Cook, C.K. Chiang, W. Wong-Ng and J. Blendell, Adv.Ceram.Mat., 2, 656, (1987).

M.R. DeGuire, R.C. O'Handley, M.D. Dyer and G. Kalonji, "Magnetic Ordering in Splat Quenched Spinel Ferrite-Silicates", *J.of Magnetism and Magnetic Materials*, **54-57** (1986) 1337.

M.R. DeGuire, R.C. O'Handley, M.D. Dyer and G. Kalonji, "Spinel Ferrite-Silica Glasses Obtained by Splat Quenching", *J.Non-Cryst.Sol.*, **81** (1986) 351-364.

L. Er-Rakho, C. Michel, J. Provost and B. Raveau, "A Series of Oxygen-Defect Perovskites Containing Cu^{II} and Cu^{III}: The Oxides $La_{3-x}Ln_xBa_3[Cu_{5-2y}(II)-Cu_{1+2y}(III)]O_{14+y}$", *J.Sol.State Chem.*, **37**, 151-156 (1981).

K.G. Frase, E.G. Liniger and D.R. Clarke, "Phase Compatibilities in the System Y_2O_3-BaO-CuO at 950°C", *Comm.Am.Ceram.Soc.*, **70** [9] C-204-C-205 (1987).

P. Gallagher, "Characterization of $Ba_2YCu_3O_x$ as a Function of Oxygen Partial Pressure, Part I: Thermoanalytical Measurements", *Adv.Ceram.Mater.*, **2** [3B] 632-639 (1987).

W.J. Gallagher, R.L. Sandstrom, T.R. Dinger, T.M. Shaw and D.A. Chance, "Identification and Preparation of Single Phase 90°K Oxide Superconductor and Structural Determination by Lattice Imaging", *Sol.State.Comm.*, in press.

P. Ganguly, A..K. Raychaudhuri, K. Sreedhar and C.N.R. Rao, "High Temperature Superconductivity in the 100°K Region in Perovskite-related Oxides of the Ln-Ba-Cu-O (Ln=Y or La) System", *Pramana-J.Phys.*, **27**(1987)L229.

S.G. Geislinger, "Determination of Microstructural Effects on Dielectric Constant in Rapidly Solidified $KNbO_3$", B.S. Thesis, Department of Materials Science and Engineering, Massachusetts Institute of Technology, June 1987.

P.M. Grant, R.B.Beyers, E.M. Engler, G. Lim, S.S.P. Parkin, M.L. Ramirez, V.Y. Lee, A. Nazzal, J.E. Vazquez and R.J. Savoy, "Superconductivity above 90°K in the Compound $YBa_2Cu_3O_{9-x}$: Structural, Transport and Magnetic Properties", *Phys.Rev.B1*, **35**(1987)7242.

Y. Hara and R.C. O'Handley, manuscript in progress, 1988.

P.H. Hor, R.L. Meng, Y.Q. Wang, L. Gao, Z.J. Huang, J. Bechtold, K. Forster and C.W. Chu, "Superconductivity above 90 K in the Square-Planar Compound System $ABa_2Cu_3O_{6+x}$ with A=Y, La, Nd, Sm, Eu, Gd, Ho, Er, and Lu", *Phys.Rev.Lett.*, **58** [18] 1891-1893 (1987).

S. Hosoya, S. Shamoto, M. Onoda and M. Sato, "High T_c Superconductivity in New Oxide Systems II", *Jpn.J.Appl.Phys.*, **26** [4] L-456-L-457 (1987).

S.-J. Hwu, S.N. Song, J.B. Ketterson, T.O. Mason and K.R. Poeppelmeier, "Subsolidus Compatibilities in the Y_2O_3-BaO-CuO System via Diamagnetic Susceptibility", submitted to *Comm.Am.Ceram.Soc.*

D.C. Johnson, H. Prakash, W.H. Zachariasen and R. Viswanathan, *Mater.Res.Bull.*, 8(1973)777.

J.K. Liang, X.T. Xu, G.H. Rao, S.S. Xie, X.Y. Shao and Z.G. Duan, J.Phys.D: Appl.Phys. 20, 1324-1326, (1987).

R.W. McCallum, R.N. Shelton, M.A. Noack, J.D. Verhoeven, C.A. Swenson, M.A. Damento, K.A. Gschneidner, E.D. Gibson and A.R. Moodenbaugh, in Novel Superconductivity, proceedings from the International Workshop on Novel Mechanisms of Superconductivity, June 22-26, 1987, Berkeley, Calif., 633-645.

C. Michel and B. Raveau, "Oxygen Intercalation in Mixed Valence Copper Oxides Related to the Perovskites", *Rev.Chim.Min.* , **21**, 407-425 (1984).

H.M. O'Bryan and P.K. Gallagher, "Characterization of $Ba_2YCu_3O_x$ as a Function of Oxygen Partial Pressure; Part II Dependence of the O-T Transition on Oxygen Content", *Adv.Ceram.Mat.*, **2**(1987)640-648.

R.S. Roth, K.L. Davis and J.R. Dennis, "Phase Equilibria and Crystal Chemistry in the System Ba-Y-Cu-O", *Adv.Ceram.Mat.*, **2** [3B] 303-312 (1987)

J.F. Schooley, W.R. Hoster, E. Ambler, J.H. Becker, M.L. Cohen and C.S. Koonce, *Phys.Rev.Lett.*, **14**(1965)305.

T. Siegrist, S.Sunshine, D.W. Murphy, R.J. Cava and S.M. Zahurak, "Crystal Structure of the High T_c Superconductor $Ba_2YCu_3O_{9-\delta}$", submitted to *Phys.Rev.Letters*, June,1987.

A.W. Sleight, J.L. Gillson and P.E. Bierstaedt, *Sol.State.Comm.*, **17**(1975)27.

H. Steinfink, J.S. Swinnes, A. Manthiram, Z.T. Sui and J.B. Goodenough, "Oxygen Stoichiometry of $YBa_2Cu_3O_{7-x}$", in Novel Superconductivity, eds. S. Wolf and V. Kresin, Plenum Press, New York, 1987, 1067-1072.

P. Strobel, J.J. Capponi, C. Chaillout, M. Marezio and J.L. Tholence, "Variations of Stoichiometry and cell symmetry in $YBa_2Cu_3O_{7-x}$ with Temperature and Oxygen Pressure", *Nature*, **327**(1987)

E. Takayama-Muromachi, Y. Uchida, Y. Matsui and K. Kato, "Identification of the High T_c Superconductor in the System Y-Ba-Cu-O", *Jpn.J.Appl.Phys.*, **26** [4] 1987, L476-478.

J.M. Tarascon, L.H. Green, W.R. McKinnon, and G.W. Hull, "Superconductivity at 90°K in a Multi-Phase Oxide of Y-Ba-Cu", *Phys. Rev. B* , **35**(1987)7115.

M. Tuominen, A.M. Goldman and M.L. Mecartney, "Magnetization of a Superconducting Glass", in High Temperature Superconductors, eds. M.B. Brodsky, R.C. Dynes, K. Kitazawa and H.L. Tuller, Materials Research Society Symposium Proceedings, Vol 99, 1988, 371-374.

M.K. Wu, J.R. Ashbun, C.J. Torng, P.H. Hor, R.L. Meng, L. Gao, Z.J. Huang, Y.Q. Wang and C.W. Chu, *Phys.Rev.Lett.*, **58**(1987)908.

W. Wong-Ng, R.S. Roth, L.J. Swartzendruber, L.H. Bennet, C.K. Chiang, F. Beech and C.R. Hubbard, "X-Ray Powder Characterization of $Ba_2YCu_3O_{7-x}$", *Adv.Ceram.Mat.*, **2**(1987)565-576.

Z. Zhao, C. Liquan, Y. Qiansheng, H. Yuzhen, C. Genghua, T. Ruming, L. Guirong, C. Changgeng, C. Lie, W. Lianzhong, G. Shuquan, L. Shanlin and B. Jianqing, "Superconductivity Above Liquid Nitrogen Temperature in Ba-Y-Cu Oxides", *Kexue Tongbao*, No. 6, 1987.

BIBLIOGRAPHY

The research described in this Ph.D. work has resulted in the following publications:

"Applications of Rapid Solidification Theory and Practice to Al_2O_3-ZrO_2 Ceramics", with G. Kalonji and L. Hobbs, Advances in Ceramics, Vol. 12, eds. N. Claussen, M. Ruhle and A. Heuer, American Ceramic Society, pp. 816-825, 1984.

"Crystallization of a Rapidly Solidified Al2O3-ZrO2 Eutectic Glass", with G. Kalonji and T. Ando, J.Non-Cryst.Sol.., **94**, 163-174 (1987).

"Microstructural Control of Al_2O_3-ZrO_2 Ceramics Through Rapid Solidification", with G. Kalonji and T. Ando, to be published in Advances in Ceramics, Vol. 24, American Ceramic Society, 1988.

"Rapid Solidification of Oxide Superconductors in the Y-Ba-Cu-O System", with L.-Q. Chen, S. Sasayama, M.E. McHenry, G. Kalonji and R.C. O'Handley, in *Adv.Ceram.Mats.*, **2**[3B], 353-363, (1987).

"Magnetic Susceptibility of Rapidly Solidified $YBa_2Cu_3O_{7-x}$ Superconductors", with M.E. McHenry, S.Sasayama, V. Kwapong, R.C. O'Handley and G. Kalonji, to be published in the Proceedings of the 32nd Annual Conference of Magnetism and Magnetic Materials, held Nov. 9-12, 1987, Chicago, Ill.

"Magnetism and Microstructure of $YBa_2Cu_3O_{7-\delta}$ Superconductors Produced by Rapid Solidification", with M.E. McHenry, S. Sasayama, V. Kwapong, R.C. O'Handley and G. Kalonji, *Phys.Rev. B*, **58**, 71-79, 1988.

"Rapid Solidification of $YBa_2Cu_3O_{7-x}$, $EuBa_2Cu_3O_{7-x}$ and $GdBa_2Cu_3O_{7-x}$" with M.E. McHenry, P. Standley, C. Heremans, T.R.S. Prasanna, G. Kalonji and R.C. O'Handley, in *Mat.Res.Soc.Symp.Proc.*, **99**, 567-570 (1988).

"Microstructural Studies of Rapidly Solidified Oxide Superconductors", with M.E. McHenry, C. Heremans, P. Standley, T.R.S. Prasanna, G. Kalonji and R.C. O'Handley, to be published in *Jpn.Inst.Met.*, Sept. 1988.

"Temperature and Field Dependent Magnetic Relaxation in $REBa_2Cu_3O_{7-x}$ Superconductors", with M. Foldeaki, M.E. McHenry, R.C. O'Handley and G. Kalonji, to be published in *Jpn.Inst.Met.*, Sept. 1988.

"Rapid Solidification Processing of High T_c Superconductors: Microstructural Features and Phase Relationships", with M.E. McHenry, C. Heremans, P. Standley, T.R.S. Prasanna, G. Kalonji and R.C. O'Handley, to be published in *Physica B*, 1988.

"Time Dependent Magnetic Response in a $GdBa_2Cu_3O_{7-x}$ Superconductor: Flux Creep or Superconducting Glass State?", with M.E. McHenry, M. Foldeaki, R.C. O'Handley and G. Kalonji, to be published in *Physica B*, 1988.